TURUN YLIOPISTON JULKAISUJA
ANNALES UNIVERSITATIS TURKUENSIS

SARJA - SER. A I OSA - TOM. 389

ASTRONOMICA - CHEMICA - PHYSICA - MATHEMATICA

Efficient Channel Modeling Methods for Mobile Communication Systems

by

Jussi Poikonen

TURUN YLIOPISTO
Turku 2008

Supervisors

Adjunct professor Valery Ipatov
Department of Information Technology
University of Turku
FIN-20014 University of Turku
Finland

Professor Jouni Isoaho
Department of Information Technology
University of Turku
FIN-20014 University of Turku
Finland

Dr. Tech. Jarkko Paavola
Department of Information Technology
University of Turku
FIN-20014 University of Turku
Finland

Reviewers

Professor Victor N. Malyshev
Faculty of Radio Engineering and Telecommunications
Saint Petersburg Electrotechnical University
Professor Popov str. 5, 197376, St. Petersburg
Russia

Dr. Tech. Jussi Vesma
Senior Research Engineer
Nokia
FIN-20520 Turku
Finland

Opponent

Professor Emeritus Ernst Bonek
Institut Für Nachrichtentechnik und Hochfrequenztechnik
Technische Universität Wien
Gusshausstrasse 25/389, A-1040, Vienna
Austria

ISBN 978-951-29-3792-9 (PRINT)
ISBN 978-951-29-3793-6 (PDF)
ISSN 0082-7002
Painosalama Oy – Turku, Finland 2008

Abstract

For purposes of simulating contemporary communication systems, it is in many cases useful to apply error models for specific levels of abstraction. Such models should approximate the error behavior of a given system at a specific protocol layer, thus incorporating the possible detrimental effects of lower protocol layers. In this Thesis, it is studied how and to which extent it is feasible to derive, based on physical channel models, finite-state models for simulating mobile wireless communication systems, and how to model specific wireless communication systems at various protocol levels, or levels of abstraction, in a computationally efficient manner.

Finite-state models are considered for physical and modulation symbol level error processes, and for packet error processes at transport stream and internet packet protocol layers of a digital video broadcast system for handheld devices. All models are derived based on underlying physical channel and system characteristics using direct theoretical analysis, or approximations based on simulations and measurements. It is found that significant performance gains are achievable with tolerable decrease in accuracy of the results compared to more detailed models. Although model abstraction reduces to some extent the possibility of modifying specific system and channel characteristics, which is an important property of simulation models, in many cases the possibility for efficient implementation and application of simplified models outweighs the disadvantages.

A specific finite-state model is proposed for efficient simulation of transmission of orthogonal frequency division multiplexing over frequency-selective fast fading channels, which is a common scenario for contemporary wireless mobile communication systems. The proposed model is derived from basic system and physical channel characteristics, and is found to be a promising tool for fast simulation of the considered scenario. Furthermore, a specific class of finite-state stochastic processes is defined and applied in simulating packet error processes of a digital video broadcasting system. An approach for determining the parameters of these models based on physical reception conditions is suggested and applied in constructing a dynamic system simulator corresponding to an existing digital video broadcasting network. The proposed simulation structure enables efficient simulation of very large groups of mobile receivers operating simultaneously within a broadcast network.

Acknowledgements

The research leading to this Thesis was funded by University of Turku and the graduate school in electronics, telecommunications and automation (GETA). Further financial support was provided by the Nokia foundation, and the Finnish foundation for technology promotion (Tekniikan edistämissäätiö, TES). I also want to thank Nokia for providing measurement equipment and DVB-H laboratory measurement data, Digita for providing signal strength prediction data for the DVB-H test network in Turku, and Jukka-Pekka Nuutinen at Elektrobit for fruitful conversations related to the research topic, and for introducing me to my opponent, professor Ernst Bonek.

Several persons contributed significantly to the timely completion of this Thesis. I am grateful for the guidance and teaching of professor Valery Ipatov, whose example in scientific thinking I hold in high regard. Furthermore, the patient support and assistance from doctor Jarkko Paavola have been invaluable for finishing this Thesis. I wish to thank professor Jouni Isoaho, who has facilitated my research and helped to obtain funding for the work. I am grateful to Mikko Jalonen for his role in building a framework within which it has been a pleasure to perform research, and for supporting my work during the years. Also, I thank the pre-reviewers of the Thesis, doctor Jussi Vesma and professor Victor Malyshev, for their comments and prompt reviews.

Throughout my Thesis research I have had the privilege of working with my colleagues and friends Heidi Himmanen and Tero Jokela, who have not only been a valuable support during my research, but also contributed to a pleasant working environment. I am grateful to Alexey Dudkov for his support, assistance and company. Furthermore, I wish to express my gratitude to all of the numerous colleagues at University of Turku, Åbo Akademi, and Turku University of Applied Sciences that I have worked and spent time with during the past three years. I have also had the pleasure of collaborating with David Gómez-Barquero from the Polytechnic University of Valencia, who has both helped me improve my work based on his questions and comments, and contributed to the research presented in this Thesis through our ongoing co-operation.

Finally, I thank my dear family – my parents Laila and Jorma, Seija Poikonen, and my brother Jonne, whose example and guidance are ever valuable to me. Also, I wish to thank Päivi Viksten and Tauno Tuomola, and especially their daughter – my beloved fiancée – Laura Tuomola, who has patiently encouraged me throughout the years.

Contents

List Of Acronyms

AFSMC	Amplitude-based Finite-State Markov Chain
AL-FEC	Application Layer Forward Error Correction
AMP	Aggregated Markov Process
ARMP	Aggregated Renewal Markov Process
ARQ	Automatic Repeat reQuest
AWGN	Additive White Gaussian Noise
BER	Bit Error Rate
BPSK	Binary Phase Shift Keying
CDF	Cumulative Distribution Function
CIR	Carrier-to-Interference Ratio
CNR	Carrier-to-Noise Ratio
DAB	Digital Audio Broadcasting
DVB-T	Digital Video Broadcasting - Terrestrial
DVB-H	Digital Video Broadcasting - Handheld
ESR	Erroneous Seconds Ratio
FFT	Fast Fourier Transform
FIR	Finite Impulse Response
FSMC	Finite-State Markov Channel
GPS	Global Positioning System
HMM	Hidden Markov Model
HMP	Hidden Markov Process
ICI	InterCarrier Interference
IFFT	Inverse Fast Fourier Transform
IP	Internet Protocol
ISI	InterSymbol Interference
LSE	Least Squared Error
LOS	Line-Of-Sight
MFER	MPE-FEC Frame Error Rate
MPE-FEC	MultiProtocol Encapsulation-Forward Error Correction
MTA	Markov-based Trace Analysis
NLOS	Non-Line-Of-Sight
OFDM	Orthogonal Frequency Division Multiplexing
PD	Probability Distribution

PDF	Probability Density Function
PDP	Power-Delay Profile
PER	Packet Error Rate
PGF	Probability Generating Function
QAM	Quadrature Amplitude Modulation
QoS	Quality of Service
QPSK	Quaternary Phase Shift Keying
RSSI	Received Signal Strength Indicator
SD	Sample Distribution
SFN	Single-Frequency Network
SINR	Signal-to-Interference plus Noise Ratio
SNR	Signal-to-Noise Ratio
TS	Transport Stream
WiMAX	Worldwide Interoperability for Microwave Access
WLAN	Wireless Local Area Network
WSS	Wide-Sense Stationary
WSSUS	Wide-Sense Stationary Uncorrelated Scattering

List of Symbols

$\mathbf{A}$	Transition probability matrix
B_C	Coherence bandwidth
$b(y\|s)$	Conditional observation probability
c	Speed of light
d	Minimum distance between modulation symbols
f_c	Carrier frequency
$f_C(n)$ $(f_E(n))$	Probability of n consecutive correct (erroneous) symbols
f_D	Maximum Doppler frequency shift
$G_C(z)$ $(G_E(z))$	Probability generating function for $f_C(n)$ $(f_E(n))$
$I_0(.)$	Modified Bessel function of the first kind and zeroth order
$J_0(.)$	Bessel function of the first kind and zeroth order
K	Number of states in a finite-state Markov channel
L_C (L_E)	Length of correctly (erroneously) received sequence
l_B	Data block length
l_{cp}	Relative cyclic prefix length
l_Q	Measurement length
Λ_R	Received SNR over Rayleigh fading
λ	SNR
$\mu_C,\ \mu_E$	Mean value for n from $f_C(n)$ $(f_E(n))$
N_{coh}	Maximum integer number of subcarriers within B_C
N_{sc}	Number of subcarriers in an OFDM symbol
N_{symb}	Number of transmitted OFDM symbols
N_t	Number of discrete WSSUS channel taps
n_e	Correction capability of an error-correcting code
P_B	Block error probability
P_i	Average power of i:th WSSUS channel tap
P_N	Noise power
P_S	Signal power
P_T	Total power of WSSUS channel taps
$\vec{\pi}$	Limiting probability vector
Q_n	Quantized quality of n:th received data block
q_C (q_E)	Correctly (erroneously) received data block
R	Rayleigh-distributed random variable

R_t	Symbol rate
$r_{XX}(\tau)$	Autocorrelation function
ρ	Average received SNR over a fading channel
$\rho_I(k)$	CIR for OFDM subcarrier k
$\mathbb{S}$	State space
S_D	Delay spread
$S^2_{L_C}$ ($S^2_{L_E}$)	Sample variance of L_C (L_E)
S_t	State of a stochastic process at time index t
σ	Standard deviation
$\mathbb{T}$	Index set
T_C	Coherence time
T_s	Symbol duration
τ_i	Delay of i:th WSSUS channel tap
$\vec{v}$	Receiver velocity
$\mathbb{Y}$	Observation space
Y_t	State of observation process at time index t

Chapter 1

Introduction

1.1 The Role of Channel Models in Communication System Development

Ideally, design, development and deployment of communication systems aims at maximally efficient utilization of available resources for transferring information reliably between a sender and a recipient. In real systems, typically some amount of unreliability is tolerated in this transfer to achieve a predefined level of consumption of limited resources. In modern communication systems, primary resources are time, space, and power and frequency bandwidth of the electromagnetic radiation used to convey information. Given such resources, systems must be designed to overcome distortions to transmitted information caused mainly by elements within the system itself, possible external communications, and the environment through which the information propagates. To achieve efficient utilization of available resources, knowledge of the mechanisms that cause interference in a given transmission scenario must be available in designing and analyzing a communication system.

Three separate methods for performance evaluation of a specific communication system can be readily identified [1]. The most resource-consuming approach is to construct a functioning system and measure its performance in a specific environment, while theoretical analysis and system simulation demand less resources. There are distinct advantages and disadvantages to each approach. For example, properly performed measurements provide unarguably realistic results for the exact scenario considered, where it may not be feasible to represent all details of the real environment and system components in analytical form or using simulation models. On the other hand, modifying specific components of a measurement scenario can be costly or even unrealizable, while analytical and simulation tools provide flexibility in changing both system and environment characteristics. Com-

monly, different performance evaluation methods are also mixed for example by constructing simulation models that include empirical and analytical components.

In performance evaluation of wireless communication systems, significance of the communication channel is emphasized, since the degradation of a signal propagating from a transmitter to a receiver is strongly dependent on their locations relative to the external environment. Wireless mobile communication, where either the transmitter or the receiver is in motion, presents additional challenges to channel modeling, as it is necessary to account for variation in the signal distortion as a function of time for each transmitter-receiver pair. Furthermore, mobile broadcasting is an increasingly popular example of unidirectional wireless communication, where thousands of mobile receivers may attempt to receive information simultaneously from a single transmitter. In developing and analyzing such systems, comprehensively modeling the transmitter-receiver link is a complicated task.

It is relevant to note that even the term *channel model* is not entirely unambiguous. Perhaps the most apparent definition is to consider the channel as the environment in which information-bearing electromagnetic radiation propagates from a transmitter to a receiver. From a system simulation point of view, a channel model is then a representation or estimation of the effects imposed on the transmitted signal by the propagation environment. Such a representation can justifiably be called a physical channel model. When considering digital communication systems, it is often convenient to include in the physical channel model also non-digital hardware components of the system, namely analog amplifiers, modulators, demodulators, and antenna elements. Equivalently, a channel model can be defined to encompass also digital components of a considered system, which effectively shifts the bounds of the channel towards higher system protocol layers. Such - possibly highly abstracted - representations are in the following called logical channel models.

For simulation purposes, the inherent abstraction of logical channel models can be realized to an advantage as decrease in computational burden. Also, because in system design it is often necessary to analyze specific system components, simplifying a simulation structure by including relevant low-level system components in an abstract black-box representation is a useful option. Again, mobile broadcast systems offer a relevant example. Designing metrics for analysis of service quality for typical content - streaming video, for example - in such systems is a nontrivial task in itself. Combining this with the challenges for channel modeling outlined above results in a scenario for which the design of simplified models is well motivated.

1.2 Finite-State Channel Models

Finite-state models are applicable as tools for simulating logical channels. For such applications, the term *finite-state channel model*, or simply *finite-state channel* may be used. A finite-state channel is in effect a quantization of the transfer channel conditions between two points in a communication system into a finite set of identifiable channel conditions, or states. The transition between channel states is determined by a probabilistic rule specific to the finite-state model. The model description also includes an error generation mechanism that determines the effect that each model state has on the signal transmitted through the channel.

Typical advantages of finite-state models for logical channels are computational efficiency, ease of application, and tractability in theoretical system analysis. In digital system simulations, finite-state channels are in many cases a natural solution, as they can easily be specified to operate with finite input and output symbol sets, which are a defining characteristic of digital systems.

There is of course a tradeoff in using highly abstracted finite-state models for logical channels. Typically, simplified channel representations both induce inaccuracy due to approximation of low-level system and channel properties, and hide the distinction between physical channel effects and signal processing in the considered system. Thus upper-level logical models are specific to a given system and channel, and the assumptions and approximations made in determining any finite-state channel should be carefully considered before applying such a model.

1.3 Problem Description and Scope

The main research problem behind the work presented in this Thesis can be formulated as follows: how and to which extent is it feasible to derive, based on physical channel models, finite-state models for simulating mobile wireless communication systems? A closely related, but more system-specific issue considered in the work is how to model specific wireless communication systems at various protocol levels, or levels of abstraction, in a computationally efficient manner. It is acknowledged that simplification of simulation structures may lead to inaccurate results compared to more detailed models. To some extent this is accepted as a tradeoff, but it is considered important to determine the level of and causes for inaccuracy introduced in model simplification. As performance metrics for comparing various models, typically statistical properties of output sequences produced by the models and subsequent upper system protocol layers are used. Although selection of suitable performance metrics for simulation models is a nontrivial issue

in itself, the objective in this work is mainly to find measures that reveal significant performance differences in relevant simulation scenarios.

Regarding the scope of the Thesis, the principle is to consider only theoretical results and system properties that are directly relevant to subsequently considered models. It is chosen not to present many related subjects such as the basic principles of digital communication systems, for which references [2–4] are suggested, system simulation [1], error correction coding [5], data interleaving for channels with memory [6], multiple-input multiple-output channel models [7], or satellite communication channel models, of which reference [8] provides a classic example. Although the primary focus of this work is on simulation models, analytical and measurement results are presented and applied where beneficial, as considered in the beginning of this Chapter.

1.4 Structure and Contributions of the Thesis

This Thesis is organized into six main Chapters and two Appendices. The main Chapters are reserved exclusively for considering simulation models for wireless mobile channels. By definition, every communication channel is linked to a system that conveys information between a source and a receiver. It is thus impossible to completely separate consideration of communication channel models from specific transmission systems to be simulated using such models. However, for sake of consistency, properties of example transmission systems relevant to the considered channel models are presented in separate Appendices.

Appendix A contains a description of the principles of orthogonal frequency division multiplexing (OFDM), which is a wireless communications transmission technique used in many contemporary communication systems such as digital video broadcasting for terrestrial and handheld devices (DVB-T and DVB-H, respectively), digital audio broadcasting (DAB), wireless local area networks (WLAN), and worldwide interoperability for microwave access (WiMAX). In this Thesis, OFDM is most relevant for simulation studies presented in Chapter 2, and for Chapter 3, where a finite-state model for simulating the performance of an OFDM system operating over a frequency-selective fading channel is considered.

As the focus of this Thesis moves in later Chapters towards efficient simulation of channels defined within specific protocol layers of communication systems, it is necessary to consider an example system for implementing such channel models. In this work, the digital video broadcasting system for handheld devices (DVB-H) is used as an example, as it is representative of contemporary wireless communication systems, and its performance is affected by all the typical characteristics of the mobile wireless communi-

cation channels that are the primary topic for this work. An overview of the DVB-H system and its most relevant properties regarding this Thesis is presented in Appendix B.

Of the primary content of the Thesis, Chapters 2 and 3 are designed mainly to provide the reader with background information and definitions related to the original contributions of this work. Thus the treatment of these Chapters is mainly of referential nature, although some original work is also presented. Chapter 2 contains information about the basic principles of low-level, or physical, channel models, which are primarily derived based on physical properties of a specific propagation environment. The basic modeling principles introduced in this Chapter are the most generic simulation tools considered in this Thesis, as they are relatively system-independent and thus applicable for a wide range of simulation scenarios. The only part of Chapter 2 where a specific transmission system is considered is Subsection 2.4.3, where selection of discrete components for a frequency-selective fading channel model is considered using a simulated OFDM system. This Subsection also contains the main original contribution of Chapter 2.

In Chapter 3, principles of simulating wireless channels using finite-state stochastic models are considered. Initially, derivation of stochastic models analytically from the physical models presented in Chapter 2 is studied. In Section 3.3, a finite-state model for frequency-selective fading channels is proposed, which is an original contribution of this work. Finite-state channel models that incorporate low-level components of specific communication systems are also considered in Chapter 3. Analytical derivation of such models from low-level channel descriptions is often challenging, and high-level finite-state models are thus typically constructed by fitting given statistical properties of such models to those of target error processes. An overview of relevant statistical inference and several examples of previously applied error models end Chapter 3.

A specific class of finite-state models is considered in Chapter 4 for simulating packet error processes. This topic continues directly from Chapter 3 by extending a classic, widely applied class of finite-state models. The considered models are also applicable for parameterization, where the parameters of the packet error models are derived based on physical reception conditions. In Chapter 4, statistical properties of a generic class of finite-state models are first derived, after which specific model realizations are considered for simulating the packet error behavior of a DVB-H system. Using error rates of upper protocol layer forward error correction coded frames as a performance metric, the effect of approximating different measured error statistics on the accuracy of the considered models is studied. Finally, determining model parameters based on the instantaneous signal-to-noise ratio and maximum Doppler frequency of the received signal is considered. Chapter 4 consists primarily of original work based on the studies presented

in references [9–16], all having the author of this Thesis as the main contributor. The considered models are also applied in reference [17], where the author is a minor contributor.

Parameterization of the error models considered in Chapter 4 offers a possibility for efficient simulation of large numbers of users moving simultaneously within a broadcast network. This kind of dynamic analysis of global service quality is relevant for mobile broadcast networks, where the majority of receivers operate in rapidly varying reception conditions. Chapter 5 consists of a case study on the principles and application of a dynamic DVB-H system simulator, which enables such analysis. In the Chapter, necessary components in a dynamic system simulator are first considered on a general level, after which a specific implementation is applied. The accuracy of the considered simulator is studied by comparing simulation results with field measurements performed in operational DVB-H test networks. Finally, application examples of dynamic DVB-H system simulations are given. Main references related to the work presented in Chapter 5 are [18, 19], in which the author of this Thesis is the main contributor, and [20], in which the author is a minor contributor.

1.5 Author's contributions

This monograph is partially based on and extended from the author's contributions in the publications listed below. In addition to these topics, this Thesis contains previously unpublished research results. In the following, the author's contribution to each of the listed publications is specified. Note that the publications below are also contained in the list of references for this work as indicated by the attached reference numbers.

- [9] J. Poikonen, "Finite-state Models for Simulating the Performance of DVB-H," *Master's thesis*, University of Turku, May 2005.

  Author's contributions: The possibility of applying various finite-state models in simulating the link and physical layers of a DVB-H system is investigated. The topic was originally specified as part of a DVB-H simulation task within the European Celtic project *Wing TV*. The work consists mostly of applying existing error models, and served as a basis for continued research on the topic. The author performed the simulation studies, simulation analyses, and literary review in this work. Professor Jouni Isoaho, professor Valery Ipatov, and doctor Jarkko Paavola acted as supervisors and instructors for the work.

- [10] J. Poikonen, J. Paavola, "Comparison of Finite-State Models for Simulating the DVB-H Link Layer Performance," *Proc. ISWCS '05*, Siena, Italy, 2005.

- [11] J. Poikonen, J. Paavola, "Error Models for the Transport Stream Packet Channel in the DVB-H Link Layer," *Proc. ICC 2006*, Istanbul, Turkey, 2006.

  Author's contributions: Publication [10] contains a summary of the results obtained in [9]; Paavola supervised the writing of the document. In [11], the author further studies the applicability of a model found promising in the previous studies, and considers a reference error model for renewal processes. Again, Paavola supervised and instructed in the writing.

- [12] J. Poikonen, "Half-normal Run Length Packet Channel Models Applied in DVB-H Simulations," *Proc. ISWCS '06*, Valencia, Spain, 2006.

  Author's contributions: This paper is an independent contribution of the author, where an approach to modeling renewal error processes using mixtures of Gaussian distributions with parameters derived from measured error statistics is proposed.

- [13] J. Poikonen, "Geometric Run Length Packet Channel Models Applied in DVB-H Simulations," *Proc. PIMRC 06*, Helsinki, Finland, 2006.

  Author's contributions: The comments given for [12] apply, but instead of Gaussian distributions, mixtures of geometric distributions are applied. In this work, an error model found promising in [9–11] is generalized, and an analytical approach to finding the error model parameters is proposed.

- [14] J. Poikonen, "Parameterization of Aggregated Renewal Markov Processes for DVB-H Simulations," *Proc. PIMRC '07*, Athens, Greece, 2007.

  Author's contributions: The comments given for [13] apply. In this paper, a more precise theoretical description of the models considered in [13] is given, along with a derivation of relevant statistical properties of the generic class of models considered and their parameter estimation.

- [15] J. Poikonen, J. Paavola, V. Ipatov, "Finite-State Models for Simulating the Packet Error Behavior of a Mobile Broadcasting System Operating in a Multi-Path Channel Environment," *Handbook of Mobile Broadcasting*, CRC Press, 2008.

- [16] J. Poikonen, J. Paavola, V. Ipatov, "Aggregated Renewal Markov Processes with Applications in Simulating Mobile Broadcast Systems," to appear in *IEEE Trans. Veh. Technol.*, January 2009.

Author's contributions: These publications are extended descriptions of the work presented in [13,14]. The considered subject is the same in [15] and [16], but [16] contains more background information and more detailed descriptions for applying the considered models. Paavola and Ipatov supervised and instructed in the writing of these publications.

- [17] J. Paavola, H. Himmanen, T. Jokela, J. Poikonen, V. Ipatov, "The Performance Analysis of MPE-FEC Decoding Methods at the DVB-H Link Layer for Efficient IP Packet Retrieval," *IEEE Transactions on Broadcasting - Special Issue on Mobile Multimedia Broadcasting*, 2007.

  Author's contributions: the author has a minor contribution in this work, where the packet error models considered in [13] are applied in simulations for analyzing DVB-H MPE-FEC decoding methods. The author implemented models used for simulations considered in the publication, and participated in editing the document.

- [18] J. Poikonen, "Applications of Parameterized Packet Error Models for Simulating Mobile DVB-H Reception in an Urban Environment," *Proc. ISWCS '07*, Trondheim, Norway, 2007.

  Author's contributions: This paper presents independent work by the author on applying the parameterized error models considered in [14–16] for simulating DVB-H networks.

- [19] J. Poikonen, D. Gómez-Barquero, "Validation of a DVB-H Dynamic System Simulator using Field Measurements," *Proc. IEEE International Symposium on Broadband Multimedia Systems and Broadcasting*, Las Vegas, Nevada, 2008.

  Author's contributions: This publication presents results based on joint research with David Gómez-Barquero from the polytechnic university of Valencia. Models proposed previously by the author are applied as a physical layer performance model in a dynamic system simulator. The publication was jointly written by the author and Gómez-Barquero.

- [20] D. Gómez-Barquero, J. Poikonen, "Filecasting for Streaming Content Delivery in IP Datacast over DVB-H Systems," *Proc. IEEE International Symposium on Broadband Multimedia Systems and Broadcasting*, Las Vegas, Nevada, 2008.

  Author's contributions: the author has a minor contribution in this paper. He provided measurement data used in the work, and reviewed the text during the writing.

Chapter 2

Principles of Terrestrial Mobile Wireless Channel Modeling

In the following, principles of modeling wireless communication channels are presented with a focus on single-link terrestrial mobile communication, where a stationary ground-based single-antenna transmitter communicates with a single-antenna receiver, which is assumed to be in outdoor pedestrian use or mounted on a moving ground vehicle. This rather detailed specification serves to rule out of the discussion specific considerations required in modeling other wireless channel scenarios such as satellite and aeroplane communication, multiple-input multiple-output channels, and indoor communication. However, many of the basic principles considered in the following apply also to other wireless channels.

The aim of the following Sections is mainly to provide the reader with preliminary information that will be referred to in Chapters 3–5. Therefore, the scope of the presentation for each topic in the following is selected according to their relevance in subsequent considerations. In Section 2.1, a typical classification of fading, or multiplicative noise, processes in wireless channel modeling is outlined with brief descriptions of the causes for and effects of the different fading types. More detailed descriptions of models for small-scale fading are then given in Sections 2.2–2.4. Finally, relevant topics related to modeling additive noise are considered in Section 2.5.

2.1 Classification of Fading Processes in Wireless Communication Channels

The distortion, or noise, caused by a communication channel to the transmitted signal can be divided into multiplicative and additive components. Multiplicative noise, or fading, can be defined as the relative difference between the power contained in a given section of the transmitted and received signals. Factors that typically contribute to the fading in wireless communication systems are the transmitter and receiver antenna and analog front-end characteristics, absorption of the signal power by the propagation media, and reflection, refraction, scattering and diffraction caused by obstacles in the propagation path [21]. The receiver experiences the combined effect of all these physical factors, which vary according to the positions of the receiver and transmitter within the propagation environment.

Fading in wireless channels is in literature typically characterized as a concatenation or superposition of several types of fading processes. These processes are often classified using the qualitative terms *path loss*, *shadowing*, and *multipath fading*, also referred to as *fast fading* [21, 22]. However, these fading processes can not in general be considered independent of each other, and indeed in many references (for example in [1, 23]) path loss and shadowing are not considered as separate processes. Justification for this will be considered in more detail in Subsection 2.1.1. In the following, fading is classified according to the typical variation from the mean attenuation over a spatial region of given magnitude. The terms large-scale, medium-scale, and small-scale fading are thus used.

Small-scale fading corresponds directly to multipath fading, and involves signal power variations of magnitude up to 40 dB on spatial scale of a half-wavelength (for example 50 cm at 300 MHz). Averaging the total fading in the receiver over a spatial interval significantly larger than a half-wavelength provides information on the medium-scale fading, or shadowing. Over spatial intervals of magnitude hundreds of meters, medium-scale fading involves signal power variations up to magnitude 20 dB. Again, averaging the total fading over a spatial interval of several hundred meters provides an estimate for the large-scale fading, which may vary up to 150 dB over the considered coverage area. [21] These denominations do not suggest a different origin or effect for the fading types, but rather signify that typically different variation around the mean attenuation is observed at different spatial scales, or observation window lengths.

2.1.1 Large-Scale Fading

Large-scale fading, or path loss, is commonly modeled for signals at a given carrier frequency as a deterministic function of the distance between the

transmitter and receiver, and is affected by several parameters such as antenna gains and properties of the propagation environment between the transmitter and receiver. Main physical factors that contribute to large-scale fading are free-space loss, or the dispersion of the transmitted signal power into surrounding space, plane earth loss, and absorption of the signal power by the propagation medium [21]. In addition to these factors, large-scale fading is defined to include the average of the shadowing and multipath fading effects. Thus the type of propagation environment must be taken into account in the total power loss. This has been done for example in the widely used Okumura-Hata [24,25] and COST 231 [26] models by approximating the parameters for the propagation loss for specific environments and transmission setups from sets of field measurements [1].

Similar results can be obtained using analytic methods by assuming a statistical terrain description, where obstacles of suitable geometry are distributed randomly in the propagation environment, and calculating the average propagation loss based on this approximation. Reference [22] contains a detailed description of deriving functions for path loss in various land environments using such methods. The physical mechanisms that cause the environment-specific propagation loss are the same for large-scale fading as for medium-scale fading, and are considered in more detail in Subsection 2.1.2.

Deterministic large-scale fading models are useful in applications where it is sufficient to have rough estimates on the average attenuation of signal power over a large transmission area. In the work presented in this Thesis, deterministic approximations for large-scale fading will not be applied as such, since it will in subsequent Chapters be found necessary to obtain more detailed approximations for the propagation loss. It should be noted that expressions for large-scale fading can be obtained for generic environments using statistical methods as outlined above, or for specific transmission sites by averaging over a site-specific approximation of medium-scale fading. However, this is typically a computationally involved task, as described in the following.

2.1.2 Medium-Scale Fading

As with large-scale fading, methods for modeling medium-scale fading can typically be categorized as statistical or site-specific. In the statistical approach, the fading is typically assumed - based on empirical data - to follow a lognormal distribution [1, 22]. The mean for this distribution can be obtained for a given carrier frequency and distance from the transmitter using expressions for large-scale fading as outlined in the previous Subsection. The standard deviation and autocorrelation of the lognormal distribution are model parameters, which must be selected according to the propagation

environment. Typically, the standard deviation is of the order 8 dB [1].

If site-specific data on the terrain profile and obstructions along the propagation path from the transmitter to the receiver are available, an approximation for the medium-scale fading can be calculated as summarized in reference [21]:

I Locate the positions and heights of the antennas.

II Construct the great circle - or geodesic - path between the antennas. This represents the shortest distance between the two terminals measured across the Earth's surface.

III Derive the terrain path profile. These are readily obtained from digital terrain maps, but it is of course also possible to use traditional contour profile maps.

IV Uplift the terrain profile by representative heights for any known buildings along the path.

V Select a value for the effective Earth radius factor appropriate to the percentage of time being designed for; modify the path profile by this value. The effective Earth radius factor is a constant used to increase the effective radius of the Earth as seen by the propagating signal. This is due to tropospheric refraction, which makes the propagation paths curve slightly towards the ground. Since the atmospheric refractivity varies with pressure, temperature and water vapor pressure of the atmosphere, the correct effective Earth radius factor will vary according to location and time.

VI Calculate the free-space loss for the path.

VII If any obstructions exist within 0.6 times the first Fresnel zone of the propagation path, calculate diffraction over these obstructions and account for the excess loss in the fading. The Fresnel zones can be though of as containing the main propagating energy in the wave; obstructions occupying less than 0.6 times the first Fresnel zone lead to an approximately 0 dB loss of signal power.

VIII Compute the path length which passes through trees and add the corresponding extra loss.

Detailed descriptions for each of the steps above are given in [21]. It should be noted that the approach outlined above accounts only for obstructions along the direct propagation path between the transmitter and receiver. Considering propagation paths corresponding to reflections from objects not along the direct path leads to small-scale fading models, considered in the following Sections.

2.1.3 Small-Scale Fading

Small-scale fading is caused by the interference between several reflected, diffracted or scattered signals arriving at the receiver. Since the reflected propagation paths may be of different length, corresponding to different arrival times for variously faded copies of the transmitted signal at the receiver, the effect of small-scale fading is in the digital domain similar to a finite impulse response (FIR) filter between the transmitter and receiver. Thus, depending on the path delay profile of the channel, small-scale fading may vary rapidly not only in the temporal and spatial domains, but also in the frequency domain.

Again, small-scale fading models can be divided into statistical and site-specific approaches. Site-specific models typically apply ray-tracing methods, where detailed three-dimensional models of the propagation environment are used to calculate propagation paths between the transmitter and receiver. Such techniques were originally developed for indoor environments, but have also been extended to dense urban outdoor areas [1]. Especially for modeling unconfined outdoor environments, ray-tracing models require large amounts of data and are computationally demanding.

Statistical models for small-scale fading are of primary relevance for this Thesis. Thus they are presented in more detail in the following Sections 2.2–2.4. Preliminary information related to statistical modeling of small-scale fading is first presented in Section 2.2. Consequently, typical approaches for modeling frequency-nonselective small-scale fading are presented in Section 2.3, and finally models for frequency-selective fading are considered in Section 2.4.

2.2 Definitions and Assumptions for Statistical Small-Scale Fading Models

2.2.1 Rayleigh and Rice Distributions

Let μ_1, μ_2 be two normally distributed random variables with zero mean and variance σ_0^2: $\mu_1, \mu_2 \sim N(0, \sigma_0^2)$. A random variable R_1, defined as $R_1 = \sqrt{\mu_1^2 + \mu_2^2}$ has the probability density function

$$p_{R_1}(r) = \begin{cases} \frac{r}{\sigma_0^2} \exp\left(-\frac{r^2}{2\sigma_0^2}\right), & r \geq 0 \\ 0, & r < 0 \end{cases} \tag{2.1}$$

and is said to be *Rayleigh distributed*. [21]

Defining a random variable R_2 as $R_2 = \sqrt{(\mu_1 + a)^2 + \mu_2^2}$, $a \in \mathbb{R}$ results

in the probability density function

$$p_{R_2}(r) = \begin{cases} \frac{r}{\sigma_0^2} \exp\left(-\frac{r^2+a^2}{2\sigma_0^2}\right) I_0\left(\frac{ra}{\sigma_0^2}\right), & r \geq 0 \\ 0, & r < 0 \end{cases} \tag{2.2}$$

where I_0 is the modified Bessel function of the first kind and zeroth order. R_2 is said to be *Rice distributed*. [21]

2.2.2 Maximum Doppler Frequency Shift

In the following, the maximum frequency shift of the received signal experienced by a moving receiver due to the Doppler effect is denoted as f_D, and can be obtained from

$$f_D = \frac{|\vec{v}|}{c} f_C, \tag{2.3}$$

where $\vec{v}$ is the receiver velocity (a stationary transmitter is assumed), c is the speed of light, and f_C is the carrier frequency of the signal. Of course, different frequency components in wideband signals experience different Doppler shifts, but this difference is considered small enough to be neglected, as the ratio between the signal bandwidth and carrier frequency is typically small.

The maximum Doppler shift given by equation (2.3) is an absolute value that corresponds to situations where the receiver is moving radially towards (corresponding to a Doppler shift of $+f_D$) or away from the transmitter (corresponding to $-f_D$). The Doppler shift corresponding to other directions of movement can be obtained as

$$f_{D,\alpha} = f_D \cos\alpha,$$

where α is the angle between directions of the receiver velocity and the arriving signal.

2.2.3 Wide-Sense Stationary Stochastic Processes

A stochastic process is a family of random variables $\{X_t\}_{t\in T}$, where T can be any set. If $T = \mathbb{N}$, the stochastic process is simply a sequence of random variables X_n. Such a sequence is called *strict-sense stationary* if and only if for any $n = 0, 1, ...$ and any $k = 1, 2, ...$, $(X_0, ..., X_n)$ and $(X_k, ..., X_{k+n})$ have the same distribution. [27]

A stochastic process is said to be *wide-sense stationary (WSS)* if the mean and autocorrelation of the random variables X_n are invariant to a shift of the origin. More specifically, for any $n = 0, 1, ...$, $k = 0, 1, ...$, $E[X_n]$ has a constant value and

$$E[X_n^* X_k] = r_{XX}(|n-k|),$$

where the asterisk denotes complex conjugation and $r_{XX}(\tau)$ is an autocorrelation function whose value depends only on the time shift τ. [28] It is clear that wide-sense stationarity is a weaker condition than strict-sense stationarity, that is, every strict-sense stationary process is wide-sense stationary, but not vice versa.

2.2.4 Assumptions

For the small-scale fading models described in the following, it is assumed that signals propagate to the receiver antenna along a horizontal plane. Furthermore, it is assumed that the angles of arrival of electromagnetic waves at the receiver antenna are uniformly distributed and that the receiver antenna has a circular-symmetric radiation pattern. As mentioned before, the transmitter antenna is assumed to be stationary, while the receiver moves with velocity $\vec{v}$.

2.3 Rayleigh and Rice Models for Frequency-Nonselective Fading

If the propagation delay differences of the reflected and scattered signal components at the receiver are negligible compared to the symbol interval of the transmission, the channel impulse response can in practice be approximated by a single delta function multiplied by a random variable that describes the amplitude fading. Thus there will be no significant interference caused by overlapping successive transmitted symbols at the receiver (*intersymbol interference*, ISI). Also, the channel affects all frequency components of the signal similarly, and the term *frequency-nonselective fading* can be used. In this case, the small-scale fading is wholly characterized by the distribution and time-variant behavior of the channel coefficient random variable.

In non-line-of-sight (NLOS) conditions, where there is no direct, unobstructed propagation path from the transmitter to the receiver, both the in-phase and quadrature parts of the received signal are assumed to consist of sums of large numbers of independently faded scattered components. Thus, by the central limit theorem, the fading of the in-phase and quadrature - or real and imaginary - components of the signal can be approximated as independent normally distributed random variables. [21] As described in Subsection 2.2.1, this leads to a Rayleigh distribution for the amplitude of the complex fading coefficient. The phase for the complex fading is uniformly distributed between 0 and 2π.

In line-of-sight (LOS) conditions, the received signal can be characterized as a sum of Rayleigh faded NLOS components as described above, and a coherent LOS component with relatively constant power determined by the

medium-scale fading. This can be approximated by adding a constant representing the amplitude of the line-of-sight signal contribution to the real part of the complex fading coefficient, which, as presented in Subsection 2.2.1, leads to a Rice distribution for the fading amplitude.

As small-scale fading is a function of the receiver location, it is clear that the rate of variation of the fading in time is dependent on the speed of the receiver. Analytically, the receiver velocity determines the Doppler frequency shift of the received signal as given in Subsection 2.2.2. Based on the maximum Doppler frequency and the angular probability distribution of the received signal components, the probability density function of the Doppler frequencies can be calculated. This probability density function is directly proportional to the Doppler power spectral density of the received in-phase and quadrature signal components, the inverse Fourier transform of which gives the autocorrelation function of the channel fading coefficient [28].

Given the assumptions of Subsection 2.2.4, for the NLOS case the Doppler power spectral distribution is completely determined by the maximum Doppler frequency shift given by equation (2.3), and follows the so called *Jakes power spectral density*, or *Clarke power spectral density*. The LOS case differs from the above in that the Doppler power spectrum also contains a component corresponding to the power and Doppler shift of the line-of-sight signal component. Figure 2.1 illustrates the probability density function of the Doppler shifts and the corresponding autocorrelation function for the Rayleigh fading process. The autocorrelation function can be written as given in reference [28],

$$r_{XX}(\tau) = 2\sigma_0^2 J_0\left(2\pi f_D \tau\right),$$

where $J_0(.)$ is the zeroth-order Bessel function of the first kind. The *coherence time* T_C of the fading process is in this work defined as the time interval that fulfils $|r_{XX}(T_C)| = 0.5 r_{XX}(0)$. For the above, $J_0\left(2\pi f_D \tau\right) \approx 0.5 \Leftrightarrow 2\pi f_D \tau \approx 1.52$ [29]. Thus $T_C \approx 1.52/(2\pi f_D)$. It should be noted that the coefficient 0.5 assumed above is in no way unique, and also other values could be assigned. However, regardless of the numerical definition, it is clear that the coherence time is reciprocally proportional to the maximum Doppler frequency f_D.

In practice, the time-variant channel coefficient for small-scale frequency-nonselective fading can be generated by drawing two sequences of normally distributed random numbers - or white Gaussian noise - corresponding to the components of the desired Rayleigh or Rice fading. One way to obtain the correct autocorrelation for the fading is then to low pass filter both of these sequences of random numbers according to the Jakes Doppler spectrum, producing colored Gaussian noise. Using the filtered sequences as the real and imaginary components of the complex fading coefficient results in

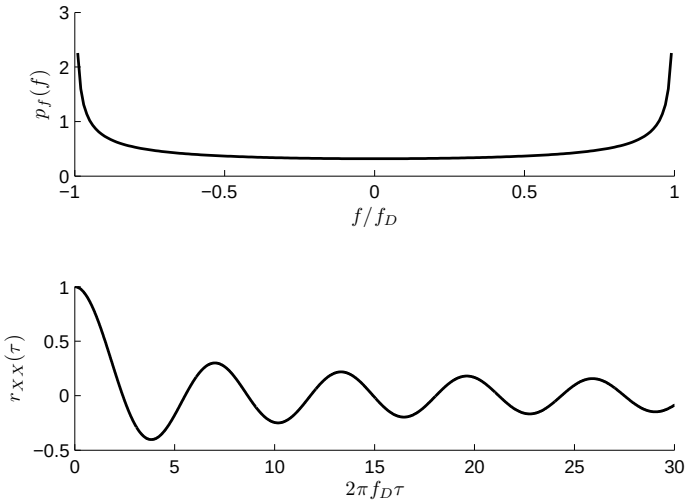

Figure 2.1: Probability density function for Doppler frequency shifts corresponding to the Jakes power spectral density (upper plot), and the corresponding autocorrelation function (lower plot).

approximately the desired probability distribution and autocorrelation described above. Non-ideality arises with this approach mainly from the fact that neither white Gaussian noise nor ideal filters can be realized exactly. [28]

In modeling small-scale fading as described above, the mean and autocorrelation function are typically kept constant, which means that the fading process is wide-sense stationary as defined in Subsection 2.2.3. It is clear that the mean value of the small-scale fading is dependent on medium-scale fading, and thus the assumption of wide-sense stationarity is not generally valid. However, as stated in reference [28], it has been empirically found that small-scale fading can be approximated as a WSS process for short distances (of order tens of wavelengths).

2.4 WSSUS Models for Frequency-Selective Fading

2.4.1 Basic Principles

If the range of propagation delay times from the transmitter to the receiver is not negligible compared to the symbol duration of the transmitted signal, additional distortions of the received signal, such as intersymbol interference and frequency-selective fading, are introduced. In such cases, the

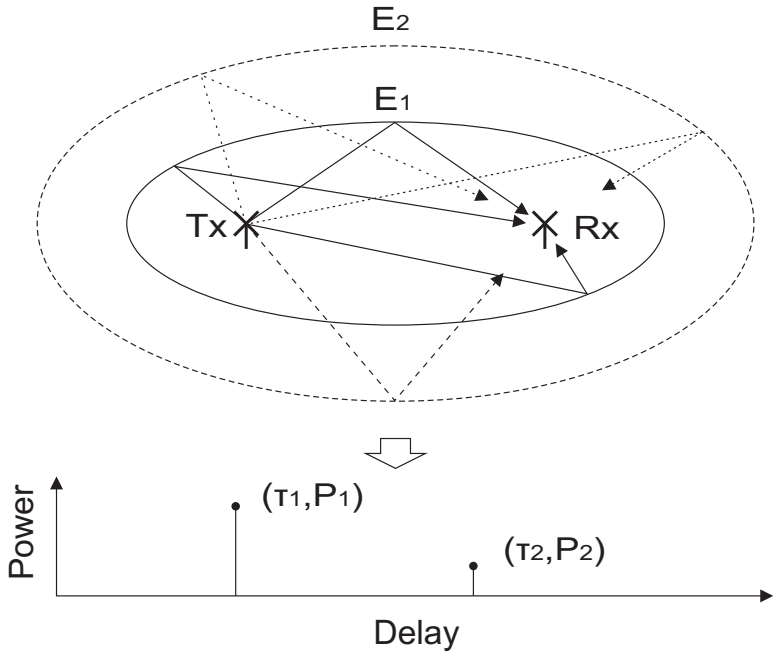

Figure 2.2: Elliptical scattering zones and a corresponding power delay profile.

frequency-nonselective fading models described in the previous Subsection are not generally sufficient to describe the channel.

Adhering to the assumptions given in Subsection 2.2.4, a physical basis for modeling a frequency-selective channel can be found in the ellipses model illustrated for example in references [21,28]. In this simplified representation of the scattering environment the transmitter and receiver are thought to be at the focal points of elliptical scattering zones, where each ellipse - or set of points with a fixed value for the sum of distances to the transmitter and receiver - defines the geometries of all propagation paths corresponding to a given propagation delay value. This principle is illustrated in Figure 2.2. Thus it is possible to consider the signal components corresponding to each discrete delay value as sums of large numbers of scattered signals with uniform distributions for the angle of arrival at the receiver. This in turn makes it possible to determine the time-variant fading coefficient for each discrete delay value as specified in the previous Subsection for frequency-nonselective fading.

Frequency-selective channel models are typically implemented as FIR filters with time-variant complex coefficients by selecting N_t fixed discrete delay values corresponding to the nonzero filter coefficients. The average power for each of the N_t delayed signal components is selected according to a specific *power-delay profile (PDP)*. Given the average powers of each of

the nonzero components of the FIR filter, the time-variant complex values for the filter coefficients are generated as WSS fading processes, as described in the previous Subsection. The N_t discrete scattering components of the channel are typically defined to be statistically uncorrelated, which leads to the denomination *wide-sense stationary uncorrelated scattering (WSSUS)* models.

The parameters that characterize a WSSUS channel model according to a given transmission scenario are the PDP, the number and delays of the discrete filter coefficients, or taps, and the types of fading processes and Doppler spectra applied for the individual taps. Typically the continuous-time power delay profile is selected according to an exponential decrease of received signal power as a function of the propagation delay, although sometimes also mixtures of exponential distributions are used. Furthermore, the tap amplitudes are most commonly modeled as Rayleigh fading processes, with possibly a short-delay component defined as line-of-sight, and thus Rice distributed. The Doppler spectra for the independent tap fading processes are typically assumed to have the Jakes distribution, although for long-delay components, or far echoes, Gaussian power spectral densities have been found more accurate in some cases [28].

2.4.2 Definitions

For a channel with a continuous exponential power delay profile of the form $S(\tau) = \frac{1}{\alpha}\exp\left(-\frac{\tau}{\alpha}\right),\ \tau > 0, \alpha > 0$, the mean delay is obtained as $\overline{\tau} = \alpha$, and the *delay spread* S_D as the square root of the second moment $S_D^2 = \alpha^2$. The Fourier transform of $S(\tau)$ is

$$\psi(f) = \frac{\frac{1}{\alpha}}{\frac{1}{\alpha} + j2\pi f},$$

which gives a measure of the correlation of the fading for a frequency separation of f Hz. The *coherence bandwidth* B_C is in this work defined - similarly to the coherence time T_C considered in the previous Section - as the frequency interval that fulfils $|\psi(B_C)| = 0.5\psi(0)$, which is obtained by writing $\sqrt{\left(\frac{1}{\alpha}\right)^2 + (2\pi B_C)^2} = \frac{2}{\alpha}$, and results in

$$B_C = \frac{\sqrt{3}}{2\pi S_D}. \tag{2.4}$$

Again, regardless of the numerical definition it is clear that the coherence bandwidth is reciprocally proportional to the delay spread of an exponential-PDP WSSUS channel. It is also evident that a continuous exponential distribution is characterized by the single free parameter α, which can be selected according to a given delay spread S_D or coherence bandwidth B_C. After

defining the continuous distribution, it still remains to determine a discrete power-delay profile that sufficiently describes the selected distribution.

A discrete power-delay profile consists of sets of propagation delay values τ_i, and average scattered signal powers $P_i,\ i = 1, ..., N_t$. In the discrete case, the delay spread can be written as

$$S_D = \sqrt{\frac{1}{P_T}\sum_{i=1}^{N_t} P_i \tau_i^2 - \left(\frac{1}{P_T}\sum_{i=1}^{N_t} P_i \tau_i\right)^2}, \tag{2.5}$$

where P_T is the total power in the channel, given by $P_T = \sum_{i=1}^{N_t} P_i$.

It is not self-evident how the selection of the number of discrete channel taps N_t and the component delays $\tau_i,\ i = 1, ..., N_t$ affects the simulation performance of a WSSUS channel model. In the following Section, this topic is addressed for simulating orthogonal frequency division multiplexing (OFDM) signals over channels with single exponential power delay profiles. OFDM modulation is used as an example, because it is a relevant transmission technique in contemporary communication systems, and the error performance of OFDM is sensitive to the characteristic properties of mobile wireless communication systems described above. Description of basic properties of OFDM systems, along with a summary of the effects of specific channel characteristics in such systems, are given in Appendix A, and are assumed to be known in the following. Also, noise-related issues relevant for the simulations performed in the following Subsection are considered in Section 2.5.

2.4.3 Simulation Study on Selecting Discrete Channel Components

Ideally the behavior of a WSSUS channel model would be estimated independently of the parameters of the communication system operating over the channel. To approach this goal, constant values are assigned for the ratio of the channel delay spread to the time duration of an OFDM symbol (S_D/T_s). Thus a rather theoretical OFDM implementation is applied, where the OFDM symbol duration T_s is determined as a function of the delay spread of the channel under study. This provides a simple way of normalizing the effect of the delay spread on the simulated error performance in comparing channels with the discrete channel components selected in different ways.

Furthermore, for non-static channels, the product of the maximum Doppler bandwidth and the time duration of an OFDM symbol, $f_D T_s$, is larger than zero, which results in a nonzero limit for the bit error rate (BER) at high carrier-to-noise ratios (CNR) due to *intercarrier interference* (ICI). Therefore, if the ratio of S_D and T_s is fixed as specified above, the value

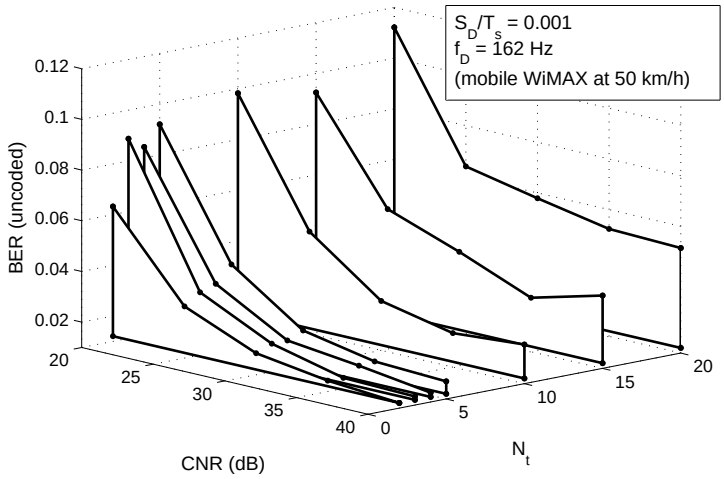

Figure 2.3: Results of a simulations performed using the WINNER C2 channel model with a fixed ratio of S_D to T_s, and a fixed maximum Doppler frequency of 162.1505 Hz.

for $f_D T_s$ should also be fixed, making the maximum Doppler bandwidth for the considered purpose a function of T_s, and thus also dependent on the delay spread of the channel for a given number of taps. As an example, the necessity for such tuning of the maximum Doppler bandwidth is illustrated in Figure 2.3, where the number of discrete propagation delay components N_t is increased from 2 to 20 according to the PDP used in the WINNER C2 channel model (selecting always the first N_t taps) specified in reference [31]. The shown BER behavior can be explained as follows: as the number of taps is increased, the delay spread increases along with the value of T_s, assuming a fixed value for S_D/T_s. Thus, if f_D is fixed, $f_D T_s$ increases along with the delay spread, which raises the BER floor.

The basic idea in the following analysis is to estimate for a generalized channel configuration the behavior of the simulated bit error rates as the number of channel taps increases. More specifically, N_t discrete delay taps are uniformly distributed between 0 and 1000 ns, with the power of each tap selected to correspond to the probability density of an exponential distribution with mean 250 ns. For the Doppler power spectrum of each channel tap, the Jakes Doppler distribution is applied. Figure 2.4 shows the power delay profile of one realization of such a randomized channel.

Initially, a static case is considered ($f_D = 0$) with $S_D/T_s = 0.001$, OFDM cyclic prefix length $l_{cp} = 1/4$, and 16-point quaternary amplitude modulation (16-QAM) subcarrier modulation with 512 subcarriers and every tenth subcarrier used as a pilot. It should be noted that with the specified ran-

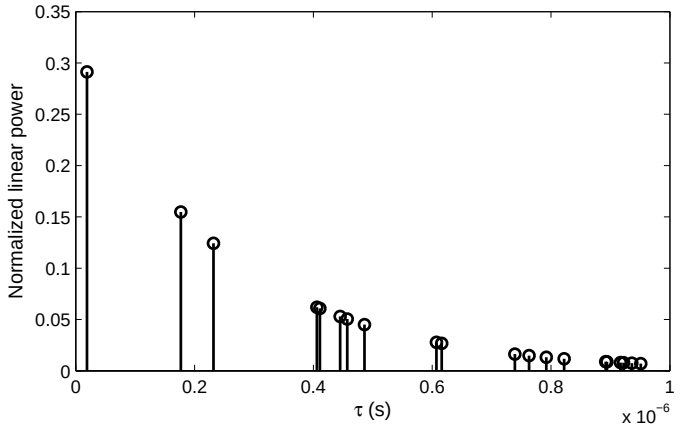

Figure 2.4: Power delay profile of one realization of a random exponential-PDP WSSUS channel.

domized channel, this value for S_D/T_s produces OFDM symbol durations comparable with the symbol duration 91.4 μs defined for a mobile WiMAX system [32]; the resulting mean value for T_s is 179 μs. The simulations are performed with 100 realizations of the randomized channel for a fixed average CNR value and for a range of numbers of channel taps. The distribution of bit error rates obtained from each set of simulations is then investigated.

For numbers of taps from 4 to 24, it is found that the distributions of bit error rates from the simulations correspond quite well to normal distributions. This is illustrated in Figure 2.5, where normal probability plots are given for $N_t = 4$ and $N_t = 24$. In a normal probability plot, data can be considered to follow a normal distribution if the data points follow a line corresponding to a fitted normal distribution. Similar results were obtained for intermediate values of N_t. The mean BER values for different numbers of taps were found to be effectively constant.

Assuming that the BER follows a normal distribution with fixed mean, the conditional probability of the BER given N_t can be estimated for the considered transmission parameters by approximating the standard deviation of the bit error rate as a function of N_t. Figure 2.6 shows estimated conditional probability distributions for the BER with 16-QAM, carrier-to-noise ratios 20 and 30 dB. This example illustrates the reduction in uncertainty of the simulated error rate as the number of taps is increased. Using this kind of analysis, the probability of a model with N_t randomly selected taps producing a given bit error rate for a specific system configuration can be determined.

Figure 2.7 shows bit error rate intervals within which the simulated BER falls with a 95 % probability assuming a random exponential PDP channel

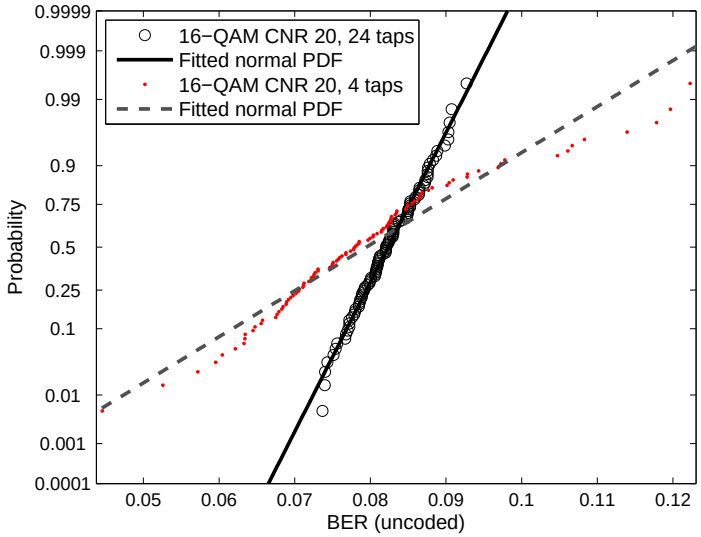

Figure 2.5: Normal probability plots for the BER of uncoded 16-QAM, $f_D = 0$, CNR = 20 dB.

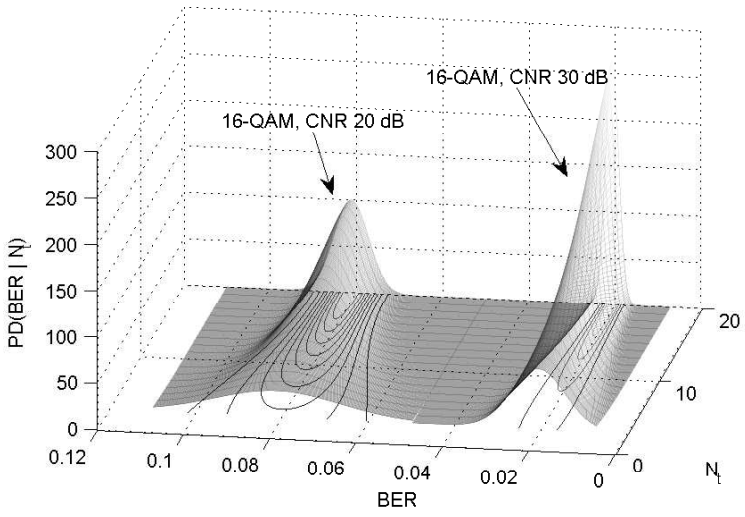

Figure 2.6: Approximated probability distributions for the BER conditioned on N_t for uncoded 16-QAM, $f_D = 0$, CNR = {20, 30} dB.

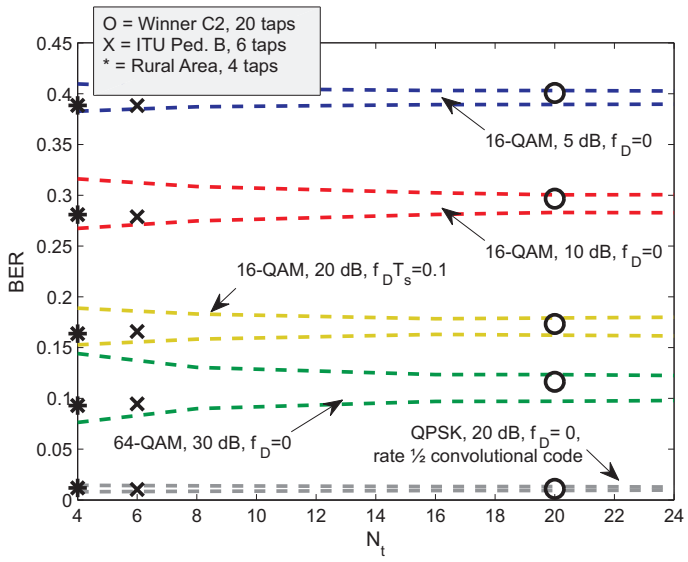

Figure 2.7: 95 % confidence intervals for the BER of a random channel compared to predefined channels, estimated for various signal constellations, average carrier-to-noise ratios and relative maximum Doppler shifts.

model with N_t taps as described above. Several examples with different average bit error rates and system parameters are shown. Bit error rates obtained using predefined channel models with different numbers of taps are also plotted in the Figure. These are implemented by taking the tap delays and average powers from the WINNER C2 model, the ITU Pedestrian B six-tap channel model [33], and the COST 207 four-tap rural area model [34], and assuming the Jakes distribution for the Doppler power spectrum of each channel tap. The obtained results suggest that selection of the tap delay values τ_i is not crucial in determining the BER performance of the considered OFDM transmission, since for all of the transmission parameters considered, each of the predefined channel models produces error rates that fall within the range of BER values produced with a 95 % probability using a PDP with randomly selected tap delays. It should be noted that in this study, non-site-specific models are assumed, where there is no specific assumption of clustering for the channel tap delays. In scenarios, where site-specific or measurement-based models are applied, it may be necessary to account for clustering, as considered for example in reference [35] for measurement-based indoor multiple-input multiple-output channel models.

In general, increasing the number of taps reduces the variation of error rates produced by a set of channels with randomly selected tap delays. If the objective is to ensure relatively consistent results by increasing the number of taps, it is relevant to investigate the gain of increasing N_t. It should be

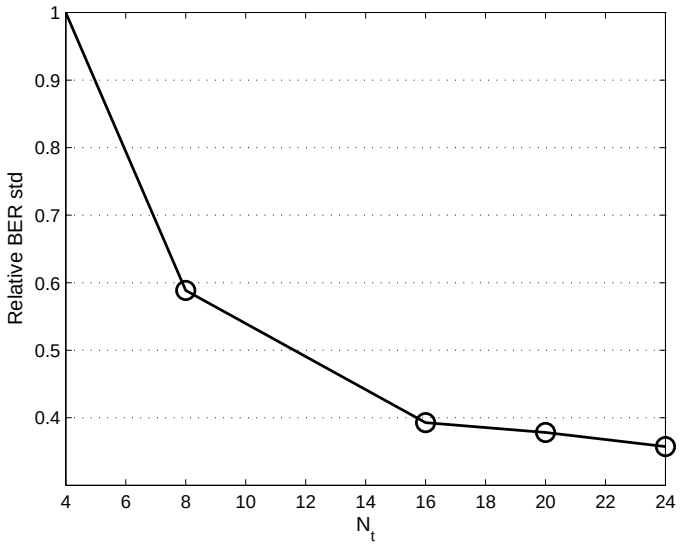

Figure 2.8: Standard deviation of the bit error rate as a function of N_t, relative to the BER std at $N_t = 4$, averaged over a large set of system parameters.

noted that for increasing simulation efficiency, the number of taps should be kept as small as possible, because the number of computations required to generate the channel coefficients increases linearly with N_t. Figure 2.8 illustrates the decrease of the standard deviation of the bit error rate as the number of channel taps is increased for the random exponential channel profile. The shown values are relative to the standard deviation at $N_t = 4$, and are averaged over a set of system parameter combinations, where quaternary phase-shift keying (QPSK), 16-QAM, and 64-QAM modulations were used, both uncoded and using a convolutional code with code rate 1/2. Carrier-to-noise ratios ranged from 5 dB to 30 dB; the values 0.001, 0.01 and 0.1 were used for $f_D T_s$, and the values 0.001 and 0.01 for S_D/T_S. From this example it can be seen that on average, increasing N_t from 4 to 8 decreases the relative standard deviation of the simulation results by approximately 40 %, while increasing N_t from 8 to 16 results in an approximately 20 % additional decrease compared to the reference value. Furthermore, increasing the number of taps from 16 to 24 decreases the relative BER standard deviation by less than 5 % of the value at $N_t = 5$.

2.5 Additive Noise

As mentioned in the beginning of this Chapter, distortions in typical wireless channels can be divided into multiplicative and additive components. In the previous Sections, multiplicative distortion - or fading - has been considered. In the following, some remarks and relevant results concerning additive distortion - also referred to simply as noise - are presented.

Additive noise is introduced to a wireless communication system both from outside sources - such as atmospheric effects, cosmic radiation and electrical devices - and from internal components of the receiver hardware, which produce thermal and shot noise [21]. Typically, additive distortion in a received signal consists of a sum of a large number of independent components, and is modeled as additive white Gaussian noise (AWGN). In some cases, the received signal is distorted also by a channel-induced superposition of different components of the useful transmission, or by signals from other transmission systems. Such distortions are called *interference*, and differ from additive noise in that typically some source-specific statistical characteristics of interference are known. Thus interference is not in all cases best approximated as an additive white Gaussian process. In this Thesis, relevant interference effects are limited to intersymbol and intercarrier interference in OFDM systems. More information on this topic is given in Appendix A.

In this work, digital data is primarily mapped to binary phase shift keying (BPSK), or various rectangular quadrature amplitude modulation signal sets (for quaternary phase shift keying, or QPSK, also the notation 4-QAM may be used). In all analytical calculations, the signal space is assumed to be sufficiently described by the complex envelopes of the individual signals. All QAM constellations used in simulations and analyzes are assumed to be uniform, that is, all adjacent constellation points are assumed equidistant. Furthermore, all modulation symbols are assumed equiprobable, and when considering bit error rates, it is assumed that Gray coding is applied in mapping data bits to modulation symbols, and minimum distance demodulation is performed in the receiver. For information on basic modulation methods and signal-space representations, references [2, 3] are suggested.

In the case of OFDM systems, it is assumed that all samples of an OFDM symbol in the frequency domain correspond to independently modulated subcarriers, which are represented by their complex modulation symbol values. In this work the signal-to-noise ratio (SNR) of OFDM subcarriers is referred to as the carrier-to-noise ratio, which generally varies both in time and in frequency. For each OFDM subcarrier, the CNR is equivalent to the sample SNR defined in the following.

In complex baseband signal-space representations, the effect of additive white Gaussian noise in the receiver can be described as a complex num-

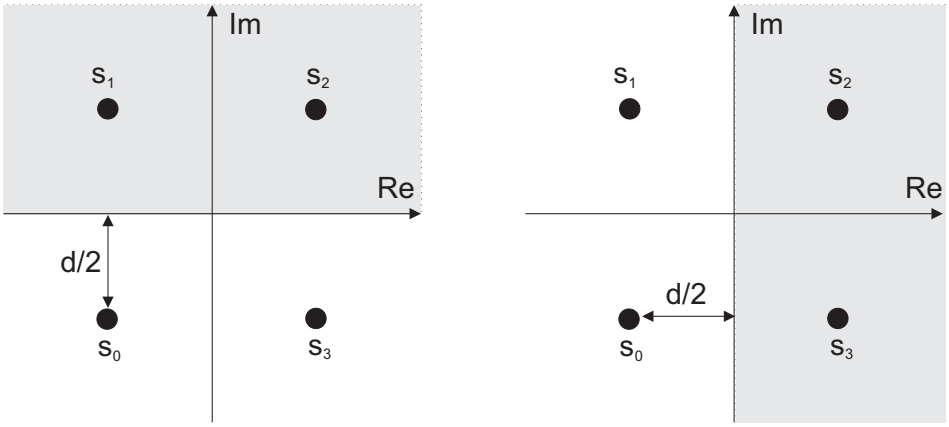

Figure 2.9: Left: imaginary component of noise is larger than $d/2$ - transmitted symbols s_0 and s_3 will be erroneously decoded either as s_1 or s_2. Right: real component of noise is larger than $d/2$ - transmitted symbols s_0 and s_1 will be erroneously decoded either as s_2 or s_3.

ber added to each transmitted modulation symbol value. The real and imaginary parts of these complex numbers are independent and identically distributed Gaussian random variables with zero mean and variance equal to $\overline{P_N}/2$, where $\overline{P_N}$ denotes the average noise power. In the following, these components are denoted by a common notation

$$X_N \sim N\left(0, \overline{P_N}/2\right).$$

If the absolute value of either the real or the imaginary noise component is larger than half of the Euclidian distance d between adjacent modulation symbols, a transmitted symbol may be erroneously decoded into any symbol within a complex half-plane, as illustrated in the QPSK example of Figure 2.9. The probability of either of the independent and identically distributed noise components having such values can be written as

$$P\left(X_N > d/2\right) = \int_{d/2}^{\infty} \frac{1}{\sqrt{\pi \overline{P_N}}} \exp\left(-\frac{x^2}{\overline{P_N}}\right) dx$$

$$= 1 - \int_{-\infty}^{\frac{d}{\sqrt{2\overline{P_N}}}} \frac{1}{\sqrt{2\pi}} \exp\left(-\frac{x^2}{2}\right) dx, \tag{2.6}$$

where the final expression is given in terms of the cumulative distribution function of a normalized Gaussian random variable.

For any of the uniform QAM constellations used as examples in this work, the distance between any pair of neighboring symbols is easily obtained as

a function of the average - over the set of modulation symbols - transmitted signal power $\overline{P_S}$ as

$$d = \begin{cases} 2\sqrt{\overline{P_S}}, \text{ (BPSK)} \\ 2\sqrt{\overline{P_S}/2}, \text{ (QPSK)} \\ 2\sqrt{\overline{P_S}/10}, \text{ (16-QAM)} \end{cases} \tag{2.7}$$

The average symbol error probability for each of the cases above is obtained by calculating averages over demodulation error probabilities for the signal sets as a function of the average signal-to-noise ratio, given by $\overline{P}_S/\overline{P}_N \hat{=} \lambda$. Using equations (2.6) and (2.7), the average symbol error probabilities are obtained as

$$p_s(\lambda) = \begin{cases} Q(\sqrt{2\lambda}), \text{ (BPSK)} \\ 2\left(Q\left(\sqrt{\lambda}\right)\right) - \left(Q\left(\sqrt{\lambda}\right)\right)^2, \text{ (QPSK)} \\ 3\left(Q\left(\sqrt{\lambda/5}\right)\right) - 9/4\left(Q\left(\sqrt{\lambda/5}\right)\right)^2, \text{ (16-QAM)} \end{cases} \tag{2.8}$$

In the above, $Q(\alpha) = 1 - \int_{-\infty}^{\alpha} \frac{1}{\sqrt{2\pi}} \exp\left(-\frac{x^2}{2}\right) dx$ as obtained in equation (2.6).

The results given above are sufficient to describe the error behavior of AWGN channels, where additive noise is the only significant distortion in the received signal, and the average noise and received signal power remain constant. In fading channels, however, the average power of the received signal should be considered a random variable as specified in the previous Sections. Thus, denoting for example the instantaneous signal-to-noise ratio for a Rayleigh channel by random variable Λ_R, the SNR can be written as

$$\Lambda_R = \frac{\overline{P_S} R^2}{\overline{P_N}},$$

where R is the Rayleigh distributed channel coefficient amplitude. The average SNR, denoted by ρ, is obtained as

$$\rho = \frac{E[R^2]\overline{P_S}}{\overline{P_N}} = \frac{2\sigma_0^2 \overline{P_S}}{\overline{P_N}},$$

where σ_0^2 is the variance of the Gaussian components used to define the Rayleigh distribution in Subsection 2.2.1. In simulations, the average power conveyed by a Rayleigh channel can thus be normalized by selecting $\sigma_0 = 1/\sqrt{2}$. The probability distribution function of Λ_R is obtained as presented in reference [21], and can be written as

$$p_\Lambda(\lambda_R) = \frac{1}{\rho} \exp\left(\frac{-\lambda_R}{\rho}\right), \ \lambda_R > 0. \tag{2.9}$$

Chapter 3

Principles of Finite-state Channel Modeling

Regardless of the model used to describe the physical transmission channel a given communication system is operated through, it is possible to increase the computational efficiency of a corresponding system simulation model by considering abstracted representations of the error behavior of the system. To be precise, in this context abstraction is defined as an act of generalization, where details of a lower abstraction level description are hidden or ignored to analyze specific properties of a process under inspection. Thus, by definition, abstracting a system model introduces a tradeoff between the level of analytical detail and compactness of representation, which is in many cases directly realizable as computational efficiency of the implementation of the considered model. In this work the focus is on efficient simulation models for communication systems, rather than on detailed analysis of system characteristics. Thus hiding, or to some extent even ignoring, analytical detail in modeling system error behavior is tolerated, given that the abstracted representation produces simulation results that agree well with those provided by a more detailed model.

In this Chapter, the use of finite-state models to approximate communication channels is considered. In relation to the above, such models can be considered direct tools for abstraction of analytical channel models. In Section 3.1, definitions and notations used throughout the rest of this work in describing finite-state models are presented. In Section 3.2, an example of a well-known finite-state model that approximates the effects of frequency-nonselective Rayleigh fading, specified in the previous Chapter, is presented. In Section 3.3, an extension to modeling frequency-selective fading is suggested. This approach is directly applicable to simulating the error behavior of OFDM systems, and to the author's knowledge has not been previously studied. Derivation of models for block error processes is considered in

Section 3.4. In Section 3.5, further abstraction of communication channels through more generic statistical models is considered.

3.1 Definitions and Notations

In the following, the notation $\{S_t\}_{t\in\mathbb{T}}$ is used for a sequence of random variables, where for each $t \in \mathbb{T}$, S_t is a random variable taking values in a finite set $\mathbb{S}$ called the state space. Unless otherwise noted, in the following it is assumed that $\mathbb{S} = \{1, 2, \ldots, K\}$. The index t is interpreted as an expression for time, thus S_t is considered to describe the state of a stochastic process at time t. Furthermore, it is assumed that the index set $\mathbb{T}$ is countable (more specifically, that $\mathbb{T} = \{0, 1, ...\}$), limiting the study to discrete-time stochastic processes.

An *m-th order Markov chain* is a discrete-time stochastic process, whose state at a given time is dependent only on the previous m states, or the context, of the process. Formally, for all $i \geq m,\ t > 0$ and state realizations u, v_i:

$$P\left(S_t = u|\{S_i = v_i\}_{i=0}^{t-1}\right) = P\left(S_t = u|\{S_i = v_i\}_{i=t-m}^{t-1}\right)$$

However, by simply redefining the state space, m can be reduced to 1 without loss of generality. [36]

The one-step state transition probabilities $P\left(S_t = j|S_{t-1} = i\right),\ n > 0$, $i, j \in \mathbb{S}$, are denoted as $a_{ij|t}$, and can be written in matrix form as

$$\mathbf{A_t} = \begin{pmatrix} a_{11|t} & \cdots & a_{1K|t} \\ \vdots & \ddots & \vdots \\ a_{K1|t} & \cdots & a_{KK|t} \end{pmatrix}.$$

If this *transition probability matrix* is stationary, i.e. independent of t, the Markov chain is called *homogenous*. [37] In such cases the time index is omitted from the expressions for state transition probabilities given above. Unless otherwise stated, time-homogenous Markov chains are assumed in the following. Furthermore, all transition probability matrices considered in this work are assumed to be right stochastic matrices, that is, square matrices where $a_{ij} \in [0, 1] \forall i, j$, and $\sum_j a_{ij} = 1 \forall i$.

Similarly to the above, n-step transition probabilities $P(S_t = j|S_{t-n} = i),\ t, m > 0,\ i, j \in \mathbb{S}$ are denoted as $a_{ij}^{(n)}$. These give the probability that a process in state i will be in state j after n state transitions. According to the Chapman-Kolmogorov equations, these probabilities can be calculated using the one-step transition probability matrix as

$$\mathbf{A}^{(n)} = \mathbf{A}^n, \tag{3.1}$$

that is, by multiplying the one-step transition probability matrix by itself n times. If $\forall i, j \in \mathbb{S}\ \exists\ n :\ a_{ij}^{(n)} > 0$, the Markov chain is said to be *irreducible*. [38]

A state $i \in \mathbb{S}$ is said to be *recurrent* if, starting in state i, the probability of the process re-entering state i is 1. If the expected time until the process returns to state i is finite, the state is said to be *positive recurrent*. In a finite-state Markov chain, all recurrent states are positive recurrent. Furthermore, a state has period d if $a_{ii}^{(n)} = 0$ when n is not divisible by d, where d is the largest integer with this property. If $d = 1$, the state is *aperiodic*. Positive recurrent, aperiodic states are called *ergodic*. For an irreducible ergodic Markov chain, $\lim_{n\to\infty} a_{ij}^{(n)} \hat{=} \pi_j$ exists and is independent of i. Now the *limiting probability* vector for the states of the considered process $\vec{\pi} = (\pi_1\ \ldots\ \pi_K)$ is obtained as the unique nonnegative solution of

$$\begin{cases} \vec{\pi}\mathbf{A} = \vec{\pi} \\ \vec{\pi}\vec{1} = 1 \end{cases} \tag{3.2}$$

where $\vec{1} = (1\ \ldots\ 1)^T$. It should be noted that the elements of $\vec{\pi}$ equal the long-run proportions of time that the process will be in each state. [38]

Let $\{Y_t\}_{t\in\mathbb{T}}$ be a discrete-time stochastic process taking values in a set $\mathbb{Y}$, called the *observation space*. Unless otherwise stated, it is assumed that $\mathbb{Y} = \{c, e\}$, where the symbols c and e correspond respectively to correct and erroneous transfer of specific information symbols. Let $y \in \mathbb{Y}$ denote the value of Y_t at a given time index. Y_t is now defined to be dependent only on S_t with conditional probability $b_t(y|s) = P(Y_t = y|S_t = s)$ for any given state s and time index t. Assuming that $\{Y_t\}_{t\in\mathbb{T}}$ are conditionally independent, that the distribution of Y_t is time-invariant and for any specific time index k, Y_k is dependent on $\{S_t\}_{t\in\mathbb{T}}$ only through S_k, the discrete-time bivariate random process $\{(S_t, Y_t)\}_{t\in\mathbb{T}}$ is called a Hidden Markov Process (HMP). Note that when a HMP is used to model for example a communication channel, the term hidden Markov model (HMM) may be equivalently applied. [39] Now the joint probability of state transition and observation y, defined as $P(S_t = j,\ Y_t = y|S_{t-1} = i)$, can be written in matrix form as

$$\mathbf{P}(y) = \mathbf{A}\mathbf{B}(y),$$

where $\mathbf{B}(y) = diag(b(y|1), \ldots b(y|K))$ [40]. Again, the time indexing is omitted from the conditional observation probabilities due to the assumption of time invariance.

If $\forall s \in \mathbb{S} :\ b(y|s) \in \{0, 1\}$, $\{(S_t, Y_t)\}_{t\in\mathbb{T}}$ is called an Aggregated Markov Process (AMP). Note that while in this case there is a deterministic mapping from each state in $\mathbb{S}$ to a corresponding observation symbol, this mapping is not bijective, i.e. the state sequence of the underlying Markov process can not be unambiguously determined from the observation sequence. Thus aggregated Markov processes are a subclass of hidden Markov processes. [39]

3.2 Finite-State Modeling of Rayleigh Fading Channels

In [41], Wang and Moayeri propose a finite-state model for a Rayleigh fading channel. The authors use the term finite-state Markov channel (FSMC), which will also be used in this work - other terms used for this model are Wang model (used for example in reference [36]), and amplitude-based finite-state Markov chain (AFSMC, [42, 43]). This model provides an illustrative example of utilizing hidden Markov models for simulating errors in a communication channel, and also serves to combine several issues presented in previous Sections.

The FSMC is based on partitioning the received signal-to-noise ratio Λ_R of a single-link wireless communication system, operating over a Rayleigh channel, into K intervals, and associating each of these intervals with a state in a homogenous first order Markov chain. It should be noted that modeling the time-variant SNR is equivalent to modeling the amplitude of the Rayleigh fading process - given constant average signal and noise powers, the instantaneous SNR can be obtained based on the fading process.

Based on the above, the state space of the FSMC is defined $\mathbb{S} = \{1, \ldots, K\}$, and the limiting state probabilities can be written, based on equation 2.9 as

$$\pi_j = \int_{\lambda_{j-1}}^{\lambda_j} \frac{1}{\rho} \exp\left(-\frac{x}{\rho}\right) dx \ \forall j \in \mathbb{S}, \tag{3.3}$$

where $0 = \lambda_0 < \ldots < \lambda_K = \infty$ are thresholds for the SNR partitions, and $\rho = E[\Lambda_R]$ is the mean signal-to-noise ratio, which defines the exponential distribution of the SNR. It should be noted that partitioning the SNR to obtain best model accuracy is a nontrivial task, as considered for example in [44]. In this work, equiprobable SNR partitions are selected, which is a relatively simple approach, but does not give the best performance in terms of matching the theoretical limiting state probabilities [44].

Furthermore, in [41] the state transition probabilities are determined based on N_k, the expected number of times per second that the received SNR passes downwards across a given threshold λ_k. This is given as

$$N_k = \sqrt{\frac{2\pi\lambda_k}{\rho}} f_D \exp\left(-\frac{\lambda_k}{\rho}\right), \tag{3.4}$$

where f_D is the maximum Doppler frequency as described in Chapter 2. Assuming that the Rayleigh fading is sufficiently slow that the SNR remains within a given state for the duration of a transmitted modulation symbol, and that state transitions are allowed only between neighboring states, the state transition probabilities are now given as

$$
\begin{aligned}
&a_{j,j+1} \approx \tfrac{N_{j+1}}{R_t \cdot \pi_j},\ j = 1, \ldots, K-1, \\
&a_{j,j-1} \approx \tfrac{N_j}{R_t \cdot \pi_j},\ j = 2, \ldots, K, \\
&a_{j,j} = 1 - a_{j,j+1} - a_{j,j+1},\ j = 2, \ldots, K-1, \\
&a_{1,1} = 1 - a_{1,2}, \text{ and } a_{K,K} = 1 - a_{K,K-1},
\end{aligned}
\tag{3.5}
$$

where R_t is the transmitted symbol rate.

Above, the Markov process $\{S_t\}$ was defined to simulate the time-variant SNR of slow Rayleigh fading. To estimate the performance of a communication system operating over this channel, the observation process $\{Y_t\}$ is defined to correspond to the error process after demodulation of a given modulation scheme at the receiver. It is thus justified to define $\mathbb{Y} = \{c, e\}$, where c and e correspond to correctly and erroneously received symbols, respectively. The conditional error probability is thus obtained as

$$
\begin{aligned}
b(e|k) = P(Y_t = e|S_t = k) &= \frac{P(S_t = k, Y_t = e)}{P(S_t = k)} \\
&= \frac{\int_{\lambda_{k-1}}^{\lambda_k} \frac{1}{\rho} \exp\left(-\frac{x}{\rho}\right) p_s(x) dx}{\pi_k},
\end{aligned}
$$

where $p_s(\lambda)$ is the symbol error probability as a function of the signal-to-noise ratio as given in equation (2.8) for BPSK, QPSK, and 16-QAM. The probability of correct reception is now $b(c|k) = 1 - b(e|k)$.

One motivation for modeling Rayleigh fading using Markov models is the intractability of multivariate Rayleigh distributions. Obtaining an accurate finite-state Markov approximation of Rayleigh fading processes would provide a tool both for efficient simulation and analysis of multivariate fading in cases where it is impractical to use multivariate statistical models. [42] For these purposes, it is important for the finite-state approximation to closely match the statistical properties of the fading to be modeled. In [47], Wang and Chang propose an information theoretic metric to show that the first-order Markov chain presented in [41] is sufficient to accurately model a slow Rayleigh fading process. The authors consider the average mutual information between the amplitude of a received symbol at a given time instant and the amplitudes of two previous symbols, and find that the contribution of channel symbols other than the immediately preceding one is negligible.

However, in [43] Tan and Beaulieu show that the measure used in [47] is insufficient to indicate the first-order Markov property. The results of [47] indicate only that a second-order Markov model for the considered slow fading is marginally better than a first-order model, but do not guarantee that a higher order Markov chain would not produce more accurate results. In [43], the authors also show that the autocorrelation of the above described first-order Markov approximation is of exponential form and does not generally

match that of the Rayleigh fading process. This means that the considered Markov model is best applicable in modeling slow fading over a limited number of samples, where the effect of the autocorrelation mismatch is negligible. This is stated also in [48], where the authors address the question of fitting the autocorrelation function of Rayleigh fading using Markov chains with order larger than one.

In [49], Bergamo et al. propose a two-dimensional Markov chain model for a Rayleigh fading process, where the state space is determined based on both the amplitude and the rate of change of the fading envelope. The authors show that improvement in simulation accuracy over a one-dimensional model is obtained, but do not give analytical expressions for determining the model parameters, which are in [49] obtained by simulation analysis. In [42], Carruthers and Beaulieu further analyze the two-dimensional model, and also provide expressions for the model parameters, which, although not possible to solve in closed form, can be estimated using numerical methods. The authors show that significant improvement in the model autocorrelation accuracy compared to a one-dimensional first-order Markov chain can be obtained, but even a two-dimensional first-order Markov chain is not sufficient to accurately match the theoretical autocorrelation function of a Rayleigh fading process.

3.3 Finite-State Modeling of Frequency-Selective Fading Channels for OFDM Systems

In the following, a set of finite-state models is used to simulate transmission of OFDM symbols over a frequency-selective Rayleigh-fading WSSUS channel. The considered model is an extension of the simple finite-state model for Rayleigh fading of [41], presented in the previous Section. Thus all the model accuracy issues such as the inaccurate autocorrelation behavior of the model with long simulation times compared to the channel coherence time are relevant also for the model considered in the following. However, it is a straightforward task to apply any of the improvements to the model of [41] presented for example in references [42–44, 49]. In the following, only the simple approach of [41] is first considered to estimate the relevance of the suggested model.

3.3.1 Preliminaries

The main initial assumption for the model to be considered is that the coherence bandwidth B_C of the channel should be larger than the OFDM subcarrier bandwidth $\frac{1}{T_s}$. The definition $B_C = \frac{\sqrt{3}}{2\pi S_D}$ for the coherence bandwidth, given in equation (2.4) is assumed in the following. As considered in

Appendix A, this is typically required for the operation of an OFDM system, and is thus not a major limitation for the simulation model. Assuming a frequency-selective channel with an exponential continuous power delay profile and Rayleigh faded scattered components with the Jakes Doppler spectrum, the channel can be constructed based only on the delay spread S_D and maximum Doppler frequency shift f_D, as described in Chapter 2. In the following, the parameters for a finite-state channel model are selected based on S_D and f_D.

In an OFDM system, the frequency spreading caused by the Doppler effect removes the perfect orthogonality of the subcarriers, thus generating inter-carrier interference. The resulting carrier-to-interference ratio (CIR) for a given subcarrier is dependent on its location within the frequency band occupied by the OFDM signal. Indexing the subcarriers according to their frequencies from the lowest to the highest, the CIR for subcarrier k - denoted by $\rho_I(k)$ - can be written as presented in [30]:

$$\rho_I(k) = \frac{1}{\frac{(T_s f_D)^2}{2} \sum_{\substack{k=1 \\ k \neq i}}^{N_{sc}} \frac{1}{(k-i)^2}}, \tag{3.6}$$

where N_{sc} is the total number of subcarriers, and f_D is the maximum Doppler frequency. It should be noted that the subcarrier-specific ICI values are generally not independent and identically distributed complex Gaussian variables. However, in the following the ICI is treated as additive complex Gaussian noise. As shown in [30], this assumption slightly raises the bit error rates with high carrier-to-noise ratios.

3.3.2 Model Description

Assuming a WSSUS channel model with each of the delay components independently Rayleigh faded and a sufficiently wide coherence bandwidth as specified above, each OFDM subcarrier can be modeled as a frequency-nonselective Rayleigh fading channel [30]. The correlation between the fading over two subcarriers is dependent on the subcarrier frequency spacing as given in equation (2.4). In the following it will be assumed that the fading is uncorrelated for subcarriers with distance in subcarrier index $N_{coh} = \lfloor B_c T_s \rfloor$, that is, the maximum integer number of subcarrier frequency separation intervals within the given coherence bandwidth (here $\lfloor . \rfloor$ signifies rounding down to the nearest integer).

Given the assumption above, it is possible to select $\lceil \frac{N_{sc}}{N_{coh}} \rceil$ (where $\lceil . \rceil$ signifies rounding up to the nearest integer, and N_{sc} is the number of subcarriers in the OFDM signal) independently faded subcarriers, equidistant at intervals of N_{coh} subcarriers within the total OFDM bandwidth. Assuming that the first selected subcarrier is the one with index number 1,

the following steps are performed to simulate transmission of N_{symb} OFDM symbols over a frequency-selective WSSUS channel with maximum Doppler frequency f_D and average carrier-to-noise ratio (excluding ICI) ρ_N:

I Generate independent state sequences $\{S_t\}_i$, where $t = 1, ..., N_{symb}$ and $i = 1, ..., \lceil \frac{N_{sc}}{N_{coh}} \rceil + 1$, using a Markov chain approximation as given in equations (3.3)-(3.5) of Section 3.2. For the average CNR of the i:th state sequence, use the value

$$\rho_{N,I} = \frac{1}{1/\rho_N + 1/\overline{\rho_{I,i}}},$$

where

$$\overline{\rho_{I,i}} = \frac{1}{N_{coh}} \sum_{k=(i-1)N_{coh}+1}^{iN_{coh}} \rho_I(k), \ i = 1, ..., \lceil \frac{N_{sc}}{N_{coh}} \rceil - 1,$$

and

$$\overline{\rho_{I,i}} = \frac{1}{N_{sc} - (i-1)N_{coh}} \sum_{k=(i-1)N_{coh}+1}^{N_{sc}} \rho_I(k), \ i = \lceil \frac{N_{sc}}{N_{coh}} \rceil.$$

$\rho_I(k)$ is given in equation (3.6). Use the above given last value of $\rho_{I,i}$ also for $S_{t,\lceil \frac{N_{sc}}{N_{coh}} \rceil + 1}$. The output at this point can be presented as a N_{symb} by $\lceil \frac{N_{sc}}{N_{coh}} \rceil + 1$ matrix of state values, where each row corresponds to one OFDM symbol, and each column corresponds to one independently faded subcarrier - the last column corresponds to the highest-frequency subcarrier, and is needed in the following. Note that the symbol duration needed to calculate R_t in equation (3.5) should be equal to $T_s(1 + l_{pr})$, where T_s is the duration of the useful OFDM symbol, and l_{pr} is the relative cyclic prefix length.

II For each value of t, interpolate $N_{coh} - 1$ state values between $\{S_t\}_i$ and $\{S_t\}_{i+1}$, $i = 1, ..., \lceil \frac{N_{sc}}{N_{coh}} \rceil - 1$. Interpolate $N_{sc} - (\lceil \frac{N_{sc}}{N_{coh}} \rceil - 1)N_{coh} - 2$ state values between $S_{t,\lceil \frac{N_{sc}}{N_{coh}} \rceil}$ and $S_{t,\lceil \frac{N_{sc}}{N_{coh}} \rceil + 1}$. The output at this point can be presented as a N_{symb} by N_{sc} matrix of state values.

III For each of the sequences generated in step 1 above, calculate the observation symbol probabilities as described in Section 3.2. For the states interpolated between $\{S_t\}_i$ and $\{S_t\}_{i+1}$, use the probabilities obtained for the nearest state sequence in step 1, in terms of subcarrier frequency separation. Generate observation symbol sequences $\{Y_t\}_j$, where $t = 1, ..., N_{symb}$ and $j = 1, ..., N_{sc}$.

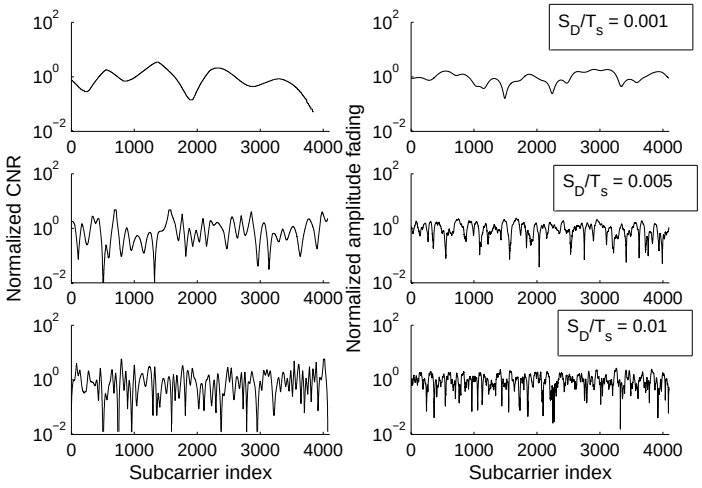

Figure 3.1: Example of frequency-selective fading generated for one OFDM symbol with 4096 subcarriers using a WSSUS channel model (right-hand plots) with a given delay spread and the corresponding finite-state model (left-hand plots) for different values of S_D/T_s.

3.3.3 Simulation Results

Simulations were performed using the above described approach with 100 CNR partitions per subcarrier (with interpolation performed using a symmetric lowpass filter), 4096 and 8192 subcarriers, BPSK and QPSK subcarrier modulations, and various values for the maximum Doppler frequency, OFDM symbol duration and average carrier-to-noise ratio. Furthermore, corresponding simulation results were also obtained by simulating an OFDM system with the given parameters over a deterministic WSSUS channel model as described in Chapter 2 with 20 discrete delay components and the channel power delay profile selected according to the WINNER C2 model [31]. Perfect channel estimation was assumed, thus no pilot symbol structure was applied, and random data was assigned to all subcarriers.

Figure 3.1 shows examples of normalized subcarrier CNR values for one OFDM symbol with 4096 subcarriers obtained using the above described finite-state model, compared to the amplitude fading produced by a frequency-selective WSSUS model. These examples serve to demonstrate the effect of reducing the coherence bandwidth of the simulated channel, and show roughly that in this aspect the proposed model behaves similarly as a corresponding WSSUS channel model.

Figure 3.2 demonstrates the bit error rate behavior of the proposed model as a function of the mean carrier-to-noise ratio and normalized maximum Doppler frequency, compared to corresponding simulations of OFDM trans-

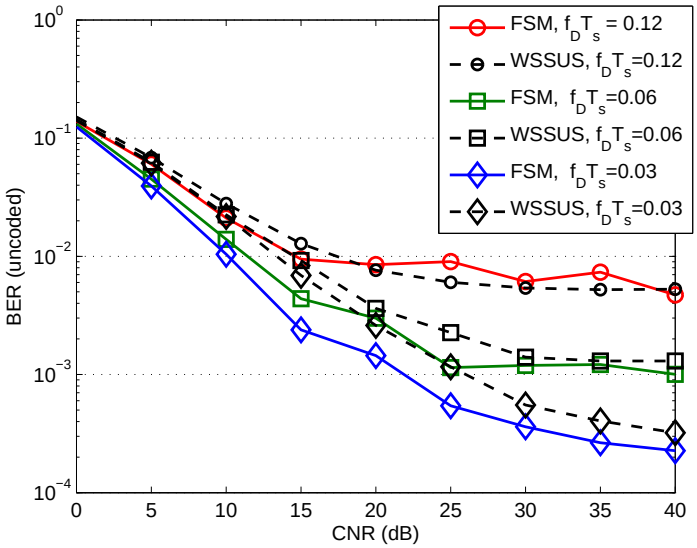

Figure 3.2: Simulated bit error rates for OFDM with 8192 subcarriers, symbol duration 91.4 μs, BPSK subcarrier modulation.

mission over a WSSUS channel. BPSK subcarrier modulation was used with 8192 subcarriers, and $S_D/T_s \approx 0.003$. (The useful OFDM symbol duration was again selected as 91.4 μs, corresponding to a mobile WiMAX system.) In these simulations, the BER produced by the proposed finite-state model corresponds well to the bit error rate obtained from the simulated OFDM system. The given simulation parameters were selected to enable comparison with the analytical results of reference [30], and it can be stated that the obtained results agree well with the reference values.

Figures 3.3 and 3.4, respectively, show sample distributions of lengths of sequences of consecutive erroneously and correctly received QPSK symbols obtained by simulating transmission of 1000 OFDM symbols, containing 4096 QPSK-modulated subcarriers each. In these examples, a small Doppler frequency ($f_D T_s = 0.001$) was assumed, with $S_D/T_s = 0.01$ and a 10 dB average CNR. It can be seen that in this scenario, the considered frequency-selective finite-state model produces results that agree very well with those obtained using the WSSUS model with a simulated OFDM system. However, as illustrated in Figure 3.5, increasing the maximum Doppler frequency by a factor of 10 ($f_D T_s = 0.01$) results in a poorer fit for the observation symbol distributions. This is most likely due to the slowly decreasing autocorrelation of the simple FSMC model applied for the individual subcarriers, which in this example can be seen in the larger probability of long error-free intervals compared to the WSSUS model.

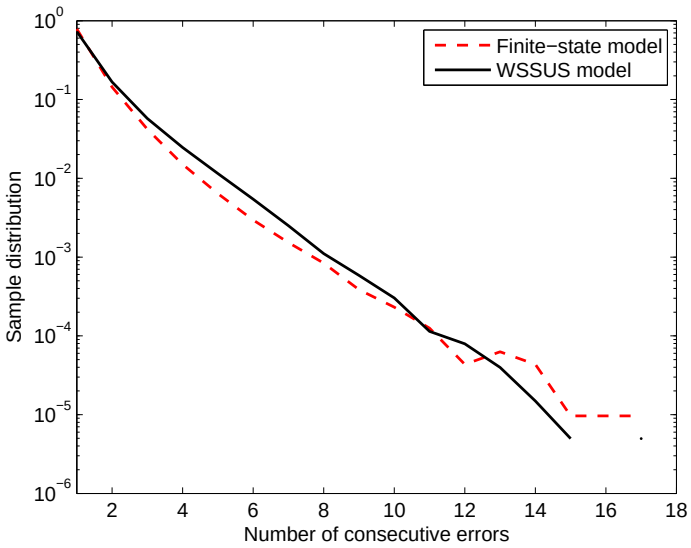

Figure 3.3: Sample distributions of simulated QPSK symbol error burst lengths, $f_D T_s = 0.001$, $S_D/T_s = 0.01$.

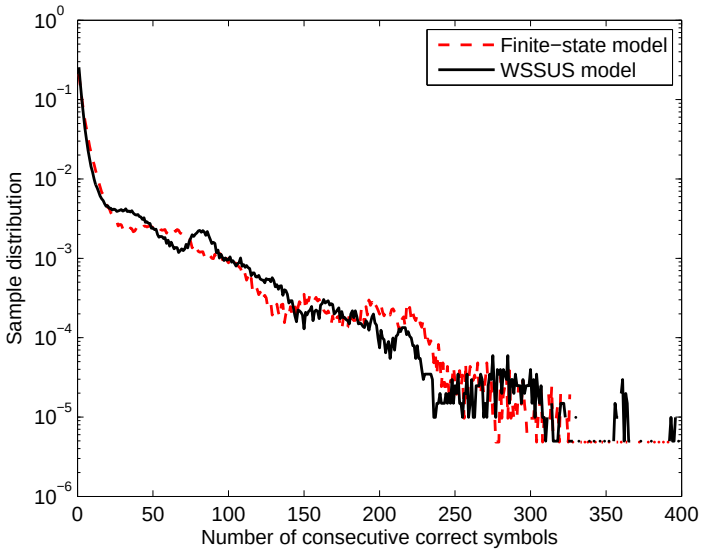

Figure 3.4: Sample distributions of simulated lengths of sequences of correctly received QPSK symbols, $f_D T_s = 0.001$, $S_D/T_s = 0.01$.

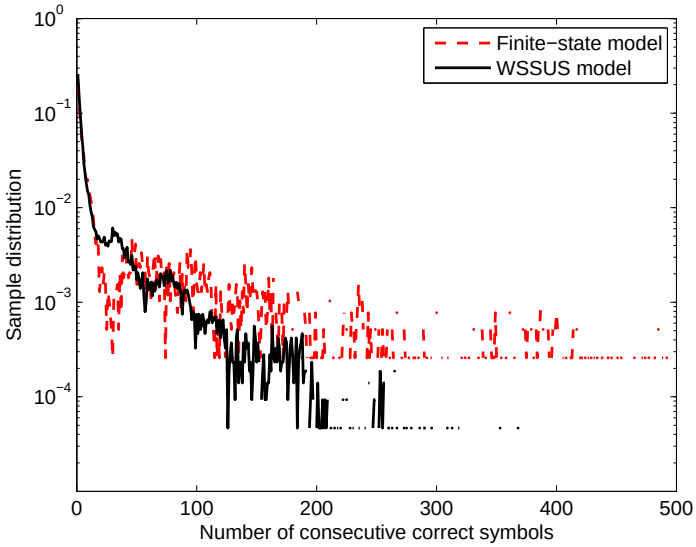

Figure 3.5: Sample distributions of simulated lengths of sequences of correctly received QPSK symbols, $f_D T_s = 0.01$, $S_D/T_s = 0.01$.

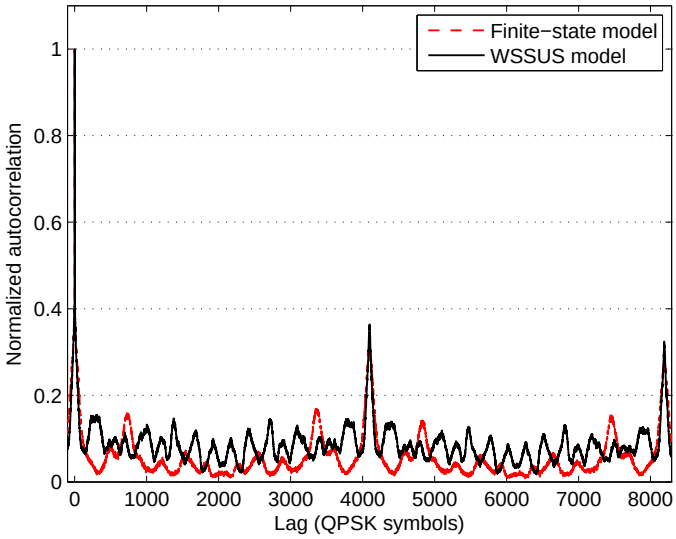

Figure 3.6: Example of autocorrelations of QPSK symbol error traces generated for a sequence of OFDM symbols with 4096 subcarriers using the considered finite-state model and a WSSUS channel model with a small Doppler frequency ($f_D T_s = 0.001$).

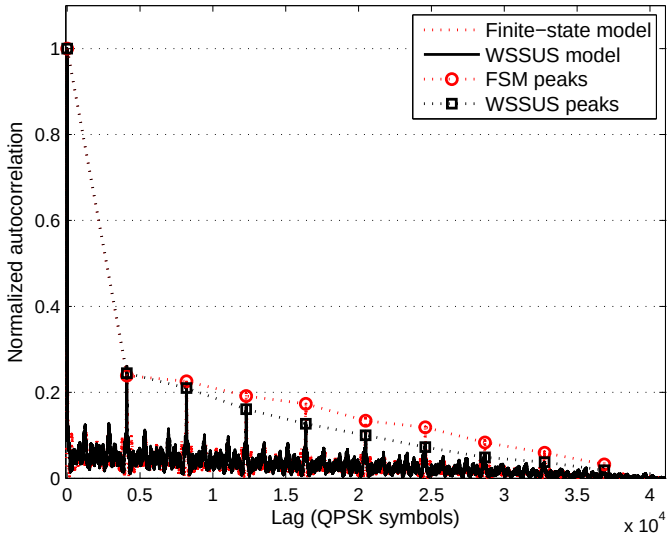

Figure 3.7: Example of autocorrelations of QPSK symbol error traces generated for a sequence of OFDM symbols with 4096 subcarriers using the considered finite-state model and a WSSUS channel model with a moderate Doppler frequency ($f_D T_s = 0.01$).

Figure 3.6 shows the autocorrelations of QPSK symbol error traces (sequences of observation symbols as defined in Section 3.1) after parallel-to-serial conversion of the OFDM subcarrier symbols. In this example, a small normalized maximum Doppler frequency ($f_D T_s = 0.001$) was used. The autocorrelation peaks at intervals of 4096 symbols, corresponding to the number of subcarriers used, indicate correlation between errors from subcarriers at the same frequencies in consecutive OFDM symbols. It can be seen that for this short-duration, low-Doppler example, the proposed finite-state model and the WSSUS simulation produce similar error sequence autocorrelations.

Figures 3.7 and 3.8 show error sequence autocorrelations for moderate and high normalized maximum Doppler frequencies, respectively. In these examples, 10 OFDM symbols are simulated, and the autocorrelation peaks corresponding to the time correlation between the symbols are marked in the Figures. It can be seen that, as expected based on the comments of Section 3.2, the autocorrelation accuracy of the proposed model decreases as the normalized Doppler frequency is increased. A straightforward improvement to the considered approach would be obtained by incorporating the improved FSMC model with more accurate autocorrelation properties described in [42]. This would also result in more complicated parameter

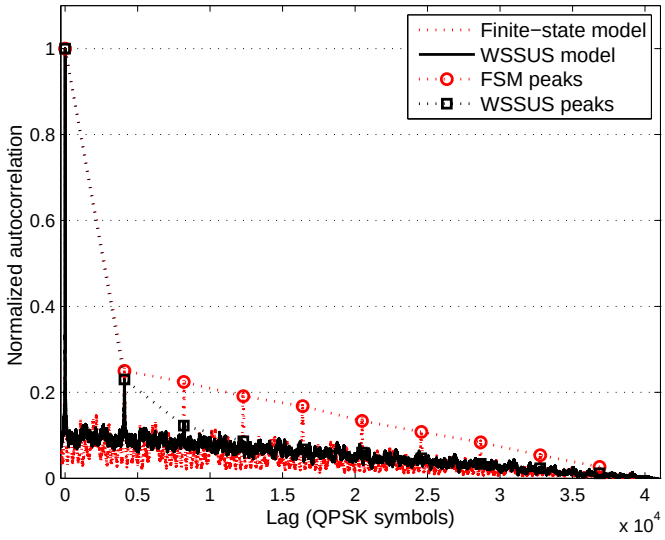

Figure 3.8: Example of autocorrelations of QPSK symbol error traces generated for a sequence of OFDM symbols with 4096 subcarriers using the considered finite-state model and a WSSUS channel model with a high Doppler frequency ($f_D T_s = 0.1$).

estimation and model structure. In the following Subsection, it is observed that in the considered application, reducing the number of states used in the model already improves its accuracy.

3.3.4 Improving the Autocorrelation Properties of the Model

To obtain the results presented in the previous Subsection, the proposed frequency-selective finite-state model was applied using sets of FSMC models as described in Section 3.2 with 100 CNR partitions for each of the independent model realizations. Using a large number of CNR partitions provides a relatively detailed approximation of the frequency-dependent carrier-to-noise ratio as illustrated in Figure 3.1. However, if - as in this work - the CNR values are not relevant as such, but only for estimating the probability of error for a given modulation method, then it is possible to considerably simplify the applied model.

From equation (3.3), it is easily found that dividing the CNR range into two equiprobable partitions results in the CNR threshold values $\lambda_0 = 0$, $\lambda_1 = \rho \ln 2$, and $\lambda_2 = \infty$, where again ρ denotes the mean CNR. For a binary state space, the state transition probability matrix can be written

generally as

$$\mathbf{A} = \begin{pmatrix} 1-a_1 & a_1 \\ a_2 & 1-a_2 \end{pmatrix}.$$

With this notation, the limiting probability vector for the state process is

$$\vec{\pi} = \left(\frac{a_2}{a_1+a_2}, \ \frac{a_1}{a_1+a_2} \right).$$

The expression above is not derived here, as it readily obtained using equation (4.2), which will be derived in Section 4.1. In the considered case, $\pi_1 = \pi_2 \Leftrightarrow a_1 = a_2 \mathrel{\hat{=}} a$. The parameter a is now determined using equations (3.4) and (3.5), which give $a = f_D T_s \sqrt{2\pi \ln 2}$. Thus the transition probability matrix can be written explicitly as

$$\mathbf{A} = \begin{pmatrix} 1-a & a \\ a & 1-a \end{pmatrix} = \begin{pmatrix} 1-f_D T_s \sqrt{2\pi \ln 2} & f_D T_s \sqrt{2\pi \ln 2} \\ f_D T_s \sqrt{2\pi \ln 2} & 1-f_D T_s \sqrt{2\pi \ln 2} \end{pmatrix}.$$

Finally, the probability of symbol error in state $i \in \{1, 2\}$ is obtained as

$$b(e|i) = 2 \int_{\lambda_{i-1}}^{\lambda_i} \frac{1}{\rho} \exp\left(-\frac{x}{\rho}\right) p_s(x) dx,$$

where $p_s(\cdot)$ is again the probability of symbol error as a function of the carrier-to-noise ratio. Expressions for this function were given in Section 3.2 for BPSK, QPSK, 16-QAM.

Based on general results given for example in reference [50], the correlation function for the state process defined above is

$$r_{XX}(m) = (1-2a)^m = \left(1 - 2 f_D T_s \sqrt{2\pi \ln 2}\right)^m,$$

where m denotes the number of transitions from the origin. For comparison, the normalized autocorrelation of a Rayleigh fading process is given by the Bessel function of the first kind and zeroth order, as described in Chapter 2. Figure 3.9 illustrates the correlation function of the state process given above, compared to the normalized autocorrelation function of Rayleigh fading evaluated at integer multiples of the symbol time T_s, or $J_0\left(2\pi f_D (m T_s)\right), \ m = 0, 1, ...$ The given example corresponds to a high normalized Doppler frequency $f_D T_s = 0.1$. Comparing the correlation functions, it is clear that with the considered finite-state model structure, only a very limited fit to the Rayleigh fading process is achievable in general.

Despite the limitations of the considered model, it should be noted that reducing the number of states in the FSMC to two as described above improves the autocorrelation accuracy of the simulated error process, compared to the results shown in the previous Subsection with 100 states in the FSMC.

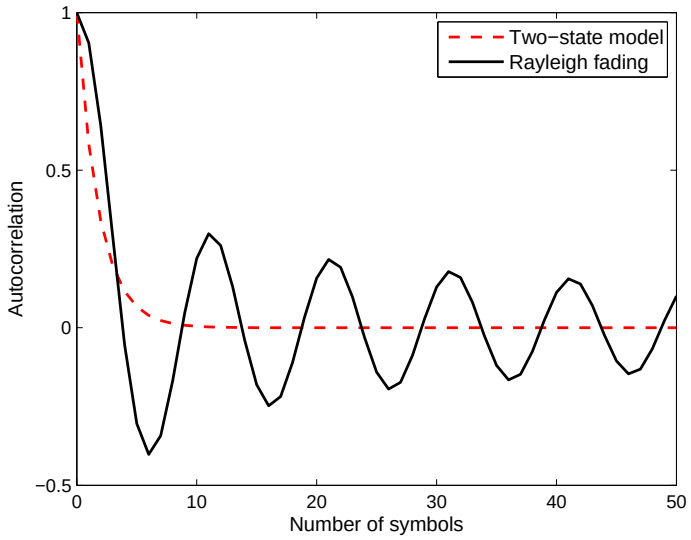

Figure 3.9: Autocorrelation functions of Rayleigh fading and a two-state FSMC for $f_D T_s = 0.1$.

Figures 3.10 and 3.11 demonstrate this improvement by plotting for 100 and two states, respectively, the autocorrelation peaks - corresponding to consecutive OFDM symbols as plotted in Figure 3.8. Furthermore, Figure 3.12 shows how reducing the number of states directly improves the fit of the sample distribution of error gap lengths produced by the finite-state model compared to the relatively poor results obtained using 100 states illustrated in Figure 3.5. Finally, to demonstrate that reducing the number of states does not decrease the accuracy of average error rates produced by the model, Figure 3.13 shows simulated symbol error rates using BPSK, QPSK, and 16-QAM for low and high normalized Doppler frequencies ($f_D T_s = 0.001$ and $f_D T_s = 0.1$, respectively).

As a side remark, it is noted that the transition probability matrix for the two-state process described above can also be defined to approximate the correlation of Rayleigh fading at a given fixed delay from the origin. For example, as considered in Section 2.4, $J_0(2\pi f_D \tau) \approx 0.5$, when $2\pi f_D \tau \approx 1.52$. Thus the minimum integer number of symbol periods T_s required for the value of the autocorrelation function to be reduced by half is obtained as

$$k = \lceil \frac{1.52}{2\pi f_D T_s} \rceil.$$

Setting for the considered two-state process the condition $r_{XX}(k) = 0.5$, the parameter required for determining the transition probability matrix $\mathbf{A}$ is

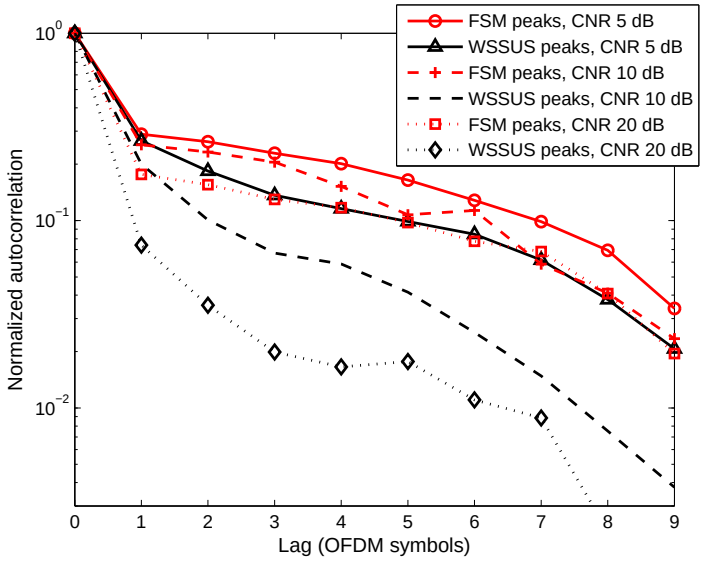

Figure 3.10: Autocorrelations of QPSK symbol error traces generated for a sequence of OFDM symbols with 4096 subcarriers, with a high relative Doppler frequency ($f_D T_s = 0.1$), using an FSMC with 100 states and a WSSUS channel model.

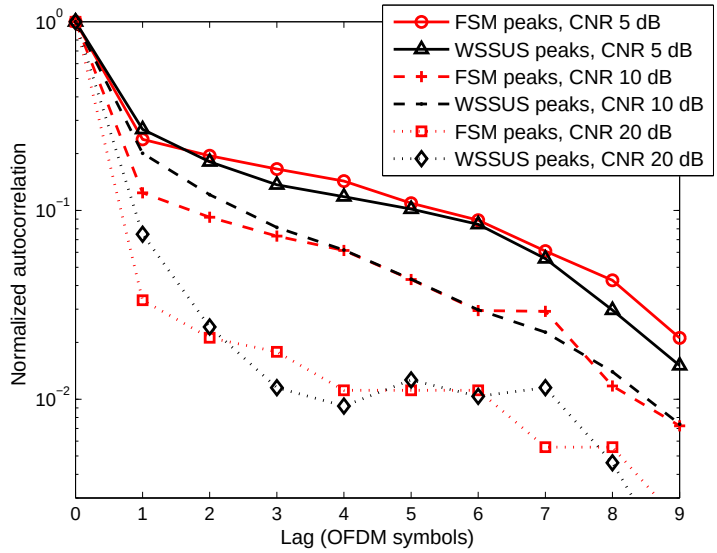

Figure 3.11: Autocorrelations of QPSK symbol error traces generated for a sequence of OFDM symbols with 4096 subcarriers, with a high relative Doppler frequency ($f_D T_s = 0.1$), using an FSMC with two states and a WSSUS channel model.

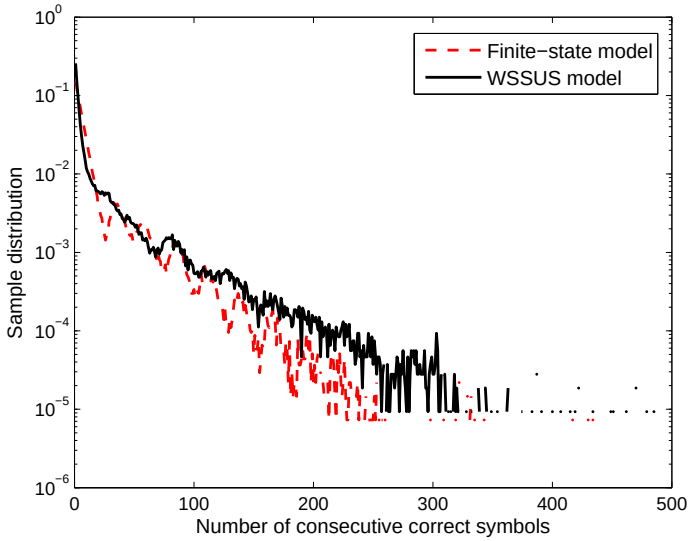

Figure 3.12: Sample distributions of simulated lengths of sequences of correctly received QPSK symbols using a two-state FSMC with $f_D T_s = 0.01$, $S_D/T_s = 0.01$.

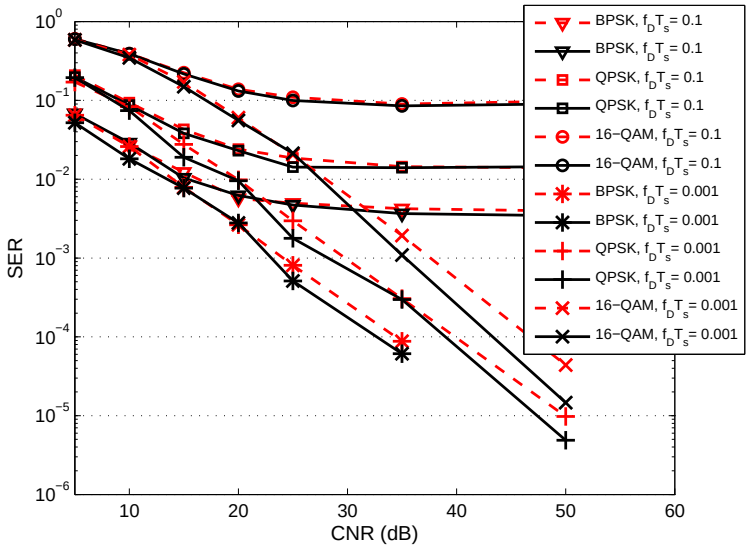

Figure 3.13: Symbol error rates using a two-state FSMC with $f_D T_s = 0.1$ and $f_D T_s = 0.001$. The solid lines correspond to simulations using a WSSUS model, and the dashed lines correspond to the frequency-selective finite-state model.

now obtained as

$$a = \frac{1 - \sqrt[k]{0.5}}{2}.$$

However, this approach was not found to produce better results than determining the parameter using equations 3.4 and 3.5 as described above.

It is relevant to consider why reducing the complexity of the FSMC model in this case improves its accuracy. An explanation for this can be found in that the model was originally defined to approximate slow fading. This was used as a justification for allowing transitions only between neighboring states. It is clear that when the maximum Doppler frequency and number of states are increased, this approximation becomes increasingly inaccurate, and the state process fails to model rapid changes of the signal-to-noise ratio. As described in the end of Section 3.2, taking into account the rate of change of the fading process is indeed the basis for the improved FSMC model considered in references [49] and [42]. Also, it is clear that with two states in the model, assuming transitions only between neighboring states is irrelevant.

From the results shown above it can be concluded that a two-state FSMC, applied as described in Subsection 3.3.2, is a promising tool for fast simulation of OFDM transmission over frequency-selective fading. Implementing the model was found to be considerably simpler than implementing a simulated OFDM system over a WSSUS channel - especially given that closed-form expressions for all the finite-state model parameters are readily obtained as described above. Furthermore, although formal complexity analysis was not performed, the simulation time required for the proposed finite-state model was found to be of order 1–10 % of the time required to simulate transmission of the same amount of data using a WSSUS model.

The model considered above will not be studied further in this Thesis. The focus in subsequent Sections will shift to simulation of errors in longer data blocks. The aim of such study is to find suitable models for arbitrary block, packet or frame error processes corresponding to given system protocol layers, ultimately to provide tools also for efficient high-level system simulations.

3.4 Threshold Models for Block Error Processes

The WSSUS channel models presented in Chapter 2 are in short an abstraction for the complicated description of wave propagation between two points in a two-dimensional environment containing a large number of scatterers. The finite-state representations of frequency-nonselective and frequency-selective Rayleigh fading presented in Sections 3.2 and 3.3 are again abstractions of the WSSUS channel models. In the following, further abstraction is

considered, starting from the representation of errors in blocks of data containing several consecutive transmitted symbols. Challenges for obtaining such representations analytically from less abstract models are also considered.

For purposes of simulating contemporary communication systems, it is in many cases not necessary to reproduce the bit or modulation symbol error behavior corresponding to a given communication channel. Such simulation cases are found most notably for system protocols where transmitted data is arranged into specific blocks, or packets, and received data blocks containing any number of errors are discarded. Thus all data blocks can be categorized either as correct or discarded. Also, for systems where blocks containing errors are not discarded, it is relevant to estimate which data blocks contain residual errors after error correction. Typical applications for block error models include analyzing automatic repeat request schemes, as for example in references [40, 51], and analyzing system performance at upper protocol layers, as for example in reference [52].

Continuing with the approach of the previous Sections, it is reasonable to consider designing efficient simulation models by directly approximating the relevant block or packet error process based on an underlying fading model. In the following, examples of block error models are presented, and the extent to which the parameters for such models may be analytically determined from underlying channel characteristics is considered. For sake of consistence, in the following expressions are derived based on a finite-state Markov channel. However, the considered modeling issues are valid also for other quantized fading processes.

Data blocks in modern communication protocols typically include error correction coding that enables recovery of a given amount of erroneous data within any received data block [2]. Considering data blocks of length l_B data symbols, including an error correction scheme able to correct n_e erroneous symbols, and assuming a constant SNR (denoted in the following as state k for an FSMC) over the duration of the data block, the block - or residual - error probability can be written as

$$P_B = \sum_{i=n_e+1}^{l_B} \left(\begin{array}{c} l_B \\ i \end{array} \right) b(e|k)^i (1 - b(e|k))^{l_B - i}, \tag{3.7}$$

where the notation $b(e|k)$ is used for the conditional symbol error probability as defined in Section 3.1.

Figures 3.14 and 3.15 show the block error probabilities as a function of $b(e|k)$ for block lengths 100 and 1000, respectively, assuming various error correction capabilities. It is evident from these examples that, especially for large block lengths, a step function can be used to approximate the block error probability as a function of the constant symbol error probability,

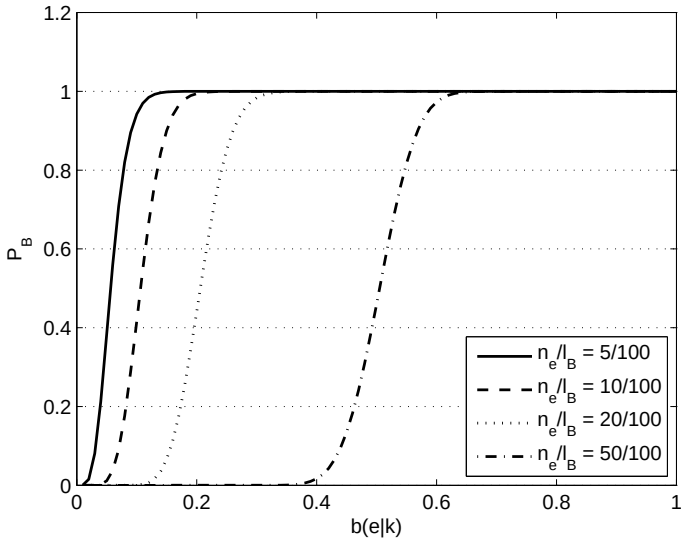

Figure 3.14: Block error probabilities as functions of the conditional error probability, $l_B = 100$.

which is directly determined by the fading state over a given data block. This behavior is the basis for threshold models for block error processes, considered for example in references [36, 49, 51, 53–56]. More specifically, a threshold model for a block error process can be obtained by finding the SNR threshold value ρ_{thr}, for which $P_B = 0.5$, assuming a given modulation scheme. Now, defining the FSMC observation process to represent block errors, the conditional observation probabilities are

$$b(e|S_t \in \mathbb{S}_<) = 1,\ b(c|S_t \in \mathbb{S}_<) = 0,\ b(e|S_t \in \mathbb{S}_>) = 0,\ b(c|S_t \in \mathbb{S}_>) = 1,$$

where $\mathbb{S}_<$ and $\mathbb{S}_>$ are subsets that partition the state space $\mathbb{S}$ into states corresponding to mean signal-to-noise ratios below and above ρ_{thr}, respectively.

The output for a threshold model for block errors, obtained from a finite-state Markov channel as described above, is a deterministic function of the underlying Markov process, or aggregated Markov process as defined in Section 3.1. This modeling approach offers a straightforward method of determining the parameters for a block error process, as the fading state transition probability matrix can be defined for a given number of discrete states using for example any of the FSMC models considered in Section 3.2.

It should be noted that if the assumption of constant fading over a data block is not valid then the expression for P_B given by equation (3.7) becomes considerably more complicated, as it is necessary to take into account all

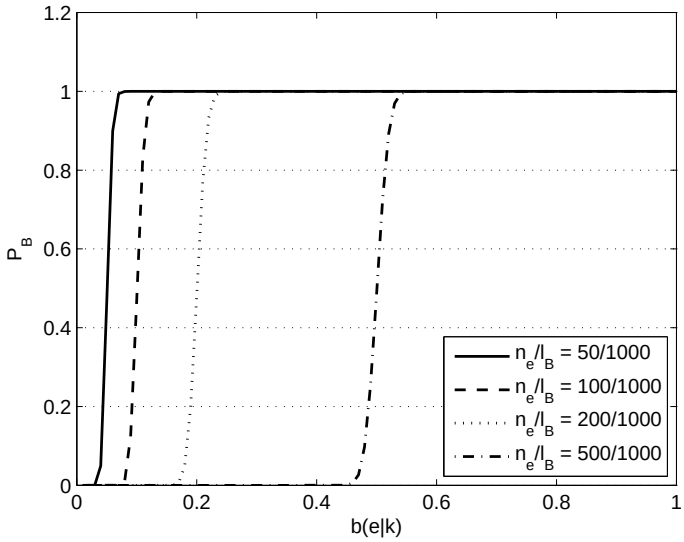

Figure 3.15: Block error probabilities as functions of the conditional error probability, $l_B = 1000$.

possible joint probabilities of the state and observation sequences over the duration of a data block. It is thus relevant to investigate the validity of this assumption. Assuming the FSMC model for Rayleigh fading, an upper limit for the probability of staying in a channel state for the duration of l_B symbols, denoted $P_{const}(l_B)$ can be obtained from the n-step transition probability matrix given in equation 3.1. Averaging these probabilities over all channel states,

$$\overline{P}_{const}(l_B) \leq \frac{tr(\mathbf{A}^{l_B})}{K}, \tag{3.8}$$

where $\mathbf{A}$ is the state transition probability matrix of the FSMC, $tr(.)$ denotes the trace (sum of main diagonal elements) of a matrix, and K is the number of states in the model. The above gives an upper limit, because the n-step transition probability includes state transition sequences where the process exits and later returns to a given state. Furthermore, as considered in the previous Sections, the autocorrelation of the fading given by the FSMC model used in the following evaluation decreases more slowly than that of a corresponding Rayleigh fading process, thus the probability of staying within a given SNR range is also higher for the FSMC, especially with large K.

Figures 3.16 and 3.17 show upper limits given by equation (3.8) for $f_D T_s = 0.001$ and $f_D T_s = 0.01$, respectively, with different numbers of states in the FSMC model. Deciding for example that a 95 % average probability of staying in any given fading state for the duration of a data

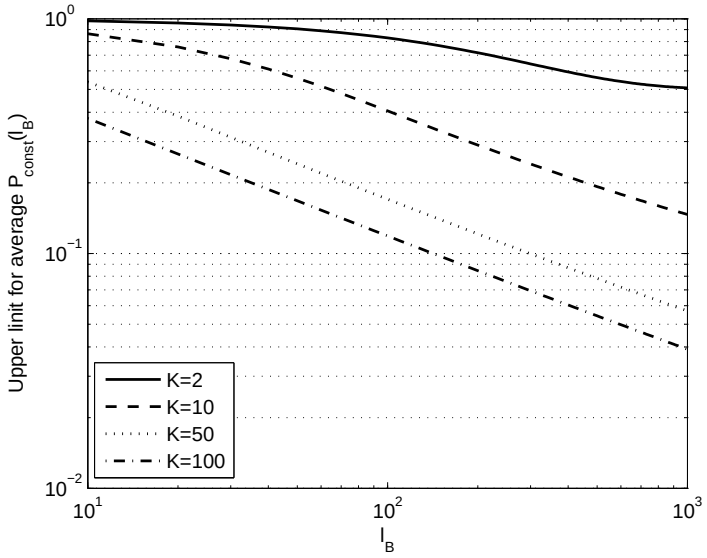

Figure 3.16: Upper limits for $\overline{P}_{const}(l_B)$ with $f_D T_s = 0.001$.

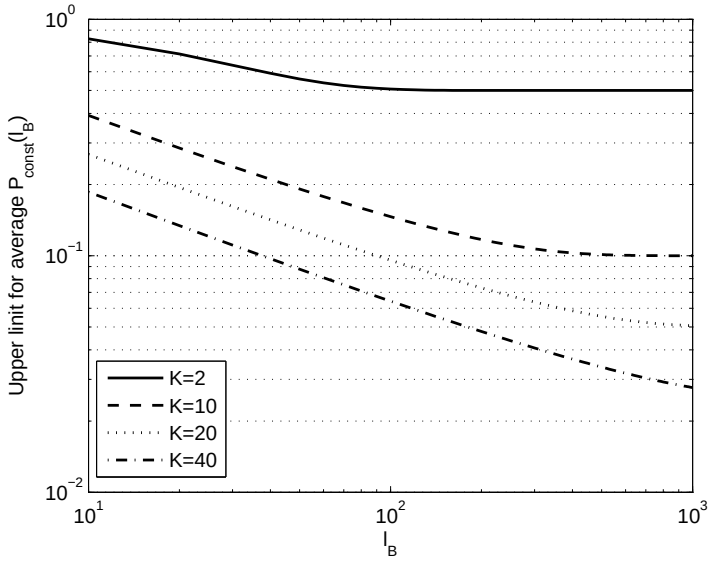

Figure 3.17: Upper limits for $\overline{P}_{const}(l_B)$ with $f_D T_s = 0.01$.

block is sufficient to allow the derivation of a block error model as specified above, then the examples given in Figures 3.16 and 3.17 clearly show that such analytical derivation is valid only for a very limited set of simulation cases, namely very low normalized Doppler frequencies, short block lengths, and small number of discrete states in the fading model.

The consideration above does not necessarily signify that it is not possible to find efficient and accurate finite-state block error models for more general fading scenarios, only that directly deriving the parameters of such models from underlying analytical channel models may not be generally tractable. Furthermore, modern communication systems typically contain interleaving between separate data blocks, along with convolutional coding, which both result in additional complexity for analytical model derivation. These considerations motivate the application of more generic finite-state structures as statistical tools for modeling error processes. More specifically, this means determining the parameters of predefined - possibly arbitrarily selected - finite-state structures to provide outputs that match a desired error process as accurately as possible according to given criteria.

3.5 Statistical Error Models

3.5.1 Statistical Inference for Hidden Markov Models

Aspects of statistical inference for hidden Markov models most relevant to communication channel modeling as considered in this Thesis can be classified under three main topics: order estimation, state inference and parameter inference. To present in detail the mathematics related to these topics is not of primary relevance for this work; for an in-depth overview, reference [57] is suggested. However, some comments on the above mentioned topics in relation to the following subsections are in order.

Widely defined, order estimation concerns the estimation of the most likely model structure to produce a given observation sequence. This is an involved and largely open area of mathematical research [57, 58]. For finite-state channel models not directly derived from underlying, possibly less abstract, analytical models as considered in Sections 3.2–3.4, analytical model order estimation is rarely considered. As will be presented in the following Subsections, determining the structure of a hidden Markov model for a given communication channel is often performed in an ad-hoc manner, with solutions justified in qualitative terms or by convenience of fitting the output of a given model structure to a desired observation sequence. This will be the case also for the packet error models proposed in Chapter 4 of this Thesis.

State inference refers to inference for the conditional probability distributions of various subsets of the hidden Markov chain $\{S_t\}_{t=0,1,\ldots}$ given a

set of observations $\{Y_t\}_{t=0,1,\ldots}$, and a known model structure and parameter values. The goal for this estimation is typically to find the most likely sequence of hidden states - using for example the Viterbi algorithm [45, 46] - or the most likely hidden state for each time index - using the forward-backward procedure [59] as described for example in references [39, 57, 58]. The former case is necessary in decoding convolutionally coded data, while the latter is relevant for example in parameter inference for hidden Markov models.

Given a model structure and observation sequence, parameter inference aims to find the most likely set of parameters for the model to produce the specific output sequence. Typically for hidden Markov models this means finding the hidden state transition probabilities, the conditional observation symbol probabilities and the initial state probability distribution. Generally, a maximum likelihood solution can be obtained using the Baum-Welch algorithm as described for example in [58], or a modification thereof [60,61]. These algorithms apply the forward-backward procedure for state inference mentioned above. Maximum likelihood parameter inference will not be considered in detail in this work; it is considered sufficient to note that for any given finite-state hidden Markov model and observation sequence, well-known solutions to this problem exist and can be found for example in the specified references.

3.5.2 Gilbert-Elliott Model

The Gilbert-Elliott model, based on the work of Gilbert [62], and a modification by Elliott [63], is a simple hidden Markov model with state space $\mathbb{S}_{GE} = \{1, 2\}$ and observation space $\mathbb{Y}_{GE} = \{c, e\}$ as defined in Section 3.1. It is probably the most widely used stochastic model for communication channels with memory; references applying the Gilbert-Elliott model are for example [64–73]. To relate the model to the considerations of previous Sections, selecting two SNR states for a finite-state Markov channel - with arbitrary selection of the SNR threshold separating the states - will produce a Gilbert-Elliott model. For wireless channels, this description corresponds directly to the typical qualitative description of the Gilbert-Elliott model as describing a communication channel that is at any given time index either in a good state corresponding to a low error probability, or in a bad state corresponding to a higher error probability. Furthermore, considering a FSMC with two states, where the SNR threshold is chosen to be ρ_{thr} as specified in Section 3.4, a threshold model for block errors can be obtained, which corresponds to a special case of the Gilbert-Elliott model, where the conditional observation symbol probabilities are quantized to 0 and 1. However, as will be considered in more detail in Chapter 4, this is generally not a very accurate model for packet error processes.

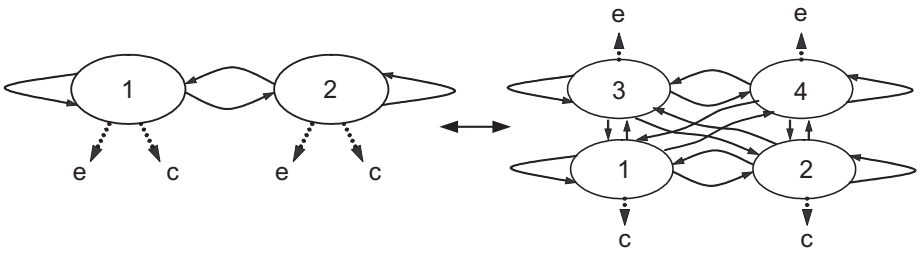

Figure 3.18: State diagram for a Gilbert-Elliott model and an equivalent AMP.

It should be noted that any finite-alphabet HMP can be described as an aggregated Markov process with an augmented state space [39]. It is thus possible to speak of equivalent models, where equivalence means that the probability of any observed output sequence, conditioned on the model structure, is the same for each model [60]. Since in the remainder of this Thesis the main focus will be on the use of specific aggregated Markov processes as communication channel models, it is relevant to determine the AMP equivalent to a given Gilbert-Elliott model.

Consider a four-state AMP with state space $\mathbb{S}_{AMP} = \{1, 2, 3, 4\}$, where the observation symbol for states 1 and 2 is c and the observation corresponding to states 3 and 4 is e. Figure 3.18 shows the state diagrams for the Gilbert-Elliott model and the considered aggregated Markov process. Now as an example of calculating the transition probabilities for the AMP based on the Gilbert-Elliott model, the probability of remaining in state 1 (denoted $a_{11,AMP}$, assuming temporarily a subscript notation to indicate the model a parameter corresponds to) can be written as

$$a_{11,AMP} = P\left(S_{t,AMP} = 1 | S_{t-1,AMP} = 1\right).$$

The equivalent probability for the Gilbert-Elliott model (defining that state 1 of the AMP corresponds to observation c in state 1 for the Gilbert-Elliott model) can be written by definition as

$$\begin{aligned} &P\left(S_{t,GE} = 1, Y_{t,GE} = c | S_{t-1,GE} = 1, Y_{t-1,GE} = c\right) \\ &= P\left(S_{t,GE} = 1, Y_{t,GE} = c | S_{t-1,GE} = 1\right) \\ &= P\left(Y_{t,GE} = c | S_{t,GE} = 1, S_{t-1,GE} = 1\right) P\left(S_{t,GE} = 1 | S_{t-1,GE} = 1\right) \\ &= P\left(Y_{t,GE} = c | S_{t,GE} = 1\right) P\left(S_{t,GE} = 1 | S_{t-1,GE} = 1\right) \\ &\hat{=} b_{GE}(c|1) a_{11,GE}. \end{aligned}$$

Above, conditional independence of the HMP observation sequence was used to proceed from the initial expression. Using similar probabilistic reasoning,

the transition probability matrix of an AMP equivalent to a given Gilbert-Elliott model can be obtained as

$$\mathbf{A} = \begin{pmatrix} b(c|1)a_{11} & b(c|2)(1-a_{11}) & b(e|1)a_{11} & b(e|2)(1-a_{11}) \\ b(c|1)(1-a_{22}) & b(c|2)a_{22} & b(e|1)(1-a_{22}) & b(e|2)a_{22} \\ b(c|1)a_{11} & b(c|2)(1-a_{11}) & b(e|1)a_{11} & b(e|2)(1-a_{11}) \\ b(c|1)(1-a_{22}) & b(c|2)a_{22} & b(e|1)(1-a_{22}) & b(e|2)a_{22} \end{pmatrix},$$

where for clarity the transition and observation probabilities inside the matrix are not explicitly notated as corresponding to the Gilbert-Elliott model, although this is of course the case.

The above considered AMP representation for the Gilbert-Elliott model is relevant also for model parameter inference. As considered by Turin and Sondhi in [61], the Baum-Welch reestimation procedure can be realized efficiently using matrix operations on the transition probability matrix of an AMP. Furthermore, in [60], Sivaprakasam and Shanmugan consider further equivalent forms for the AMP transition probability matrix, where probabilities of transition between states corresponding to the same observation symbol are set to zero. This results in a partially diagonal transition probability matrix, which allows for an even more efficient realization of the Baum-Welch algorithm.

3.5.3 Fritchman Model

The model proposed by Fritchman in [74] can be defined as an aggregated Markov process with an arbitrary number of states and a binary observation space. For this rather generic class of models, Fritchman derives the probability distributions of lengths of sequences of consecutive observation symbols, and considers the capacity of a communication channel represented by such models. The author then proceeds to explicitly determine the channel capacity for a special case with only a single error state in the model. Finally, Fritchman presents simulation results using a simplified model structure with a single error state, an arbitrary number of error-free states, and no transitions between error-free states. This approach has subsequently been called the simplified Fritchman model, or in some references simply the Fritchman model. As an example, the transition probability matrix for a simplified Fritchman model with N error-free states and one error state can be written as

$$\mathbf{A} = \begin{pmatrix} \alpha_1 & 0 & 0 & 1-\alpha_1 \\ 0 & \ddots & 0 & \vdots \\ 0 & 0 & \alpha_N & 1-\alpha_N \\ w_1 & \cdots & w_N & 1-\sum_{i=1}^{N} w_i \end{pmatrix}.$$

From this representation it is evident that the model can be completely determined by selecting the probabilities of transition to the error-free states. In Chapter 4, statistical properties for a more general class of finite-state models that includes the above as a special case are derived.

The simplified Fritchman model is useful for simulating channels where the error burst lengths can be characterized by a single exponential distribution, and the more complicated distributions of error gap (sequence of consecutive correctly received data units) lengths can be approximated using mixtures of exponential distributions. For mobile radio channels, this is in many cases a reasonable assumption - see for example Figures 3.3 and 3.4 - especially with low error rates. This, along with the relative simplicity of determining the simplified Fritchman model parameters accounts for the popularity of the model for simulating wireless mobile channels. Some example applications can be found in references [65, 67, 72, 73, 75–77].

The simplified Fritchman model is an example of a *renewal model*, where the observation symbol burst lengths are independent and identically distributed for a given observation symbol (since in this case there are two observation symbols, the term *alternating renewal process* [78] can also be used). Thus the model parameters can be obtained simply by fitting the theoretical run length distributions of the model with sample distributions obtained from measurements or simulations. The parameters (transition probabilities) for the error-free states are typically obtained from measured or simulated distributions using empirical procedures such as curve fitting [74] or gradient-based methods [65].

As noted in [1], while this model is applicable to discrete channels with simple error burst length distributions, it is not generally adequate for characterizing complex burst error patterns, which would require additional error states - examples of such situations are considered in Chapter 4. Generally in such cases it is difficult to obtain the model parameters from measured observation symbol burst length distributions alone, and typically it is considered necessary to apply more complex parameter estimation methods such as the Baum-Welch algorithm, or for example basis sequence estimation as suggested by Pimentel and Blake in reference [67], where this parameter estimation approach is implemented also for the Gilbert-Elliott model.

In Chapter 4 a finite-state structure is considered, which retains the renewal property of the simplified Fritchman model while allowing for arbitrary numbers of good and bad states in the model. This enables simple estimation of the model parameters from measured observation symbol burst length distributions, but includes the possibility to account also for scenarios with more complicated error burst distributions. Furthermore, analytical expressions for obtaining the parameters of specific models are also given in Chapter 4. Before continuing to these topics, some examples of other recent error modeling approaches are given in the following Subsection. This

treatment is not intended to be a comprehensive overview of the development of stochastic channel models, but rather to provide references to other approaches applicable for the considered task of efficient modeling of packet error processes.

3.5.4 Other Statistical Models

Several useful basic structures of generative and descriptive channel models are reviewed in [79]. These include for example the classical Gilbert-Elliott and Fritchman models considered above. Less frequently used structures described in [79] include for example the infinite-state slowly spreading chain [80], a finite-state variant of which was recently applied by Tralli and Zorzi in [52] to model the block error process in a wideband CDMA system.

Other recent generative models for packet channels are presented for example in [36], where the Babich and Lombardi extend the Markov model for Rayleigh fading of [41] to modeling block failure processes in slow Ricean fading, and in [81], where Konrad et al. present an algorithm for analyzing and reproducing statistical properties of measured packet error traces. Furthermore, in [82], Zhu and Garcia-Frias apply models based on stochastic context-free grammars in describing communication channels with bursty error behavior; this model would also seem suitable for modeling packet errors. It is notable that the latter two models require applying the given algorithms with specific empirical data for approximating statistical properties of the given measurement, while the approaches used in [36, 41, 52] are similar to the underlying principle of the models presented in the next Chapter of this Thesis, where the goal is to parameterize the described packet error models using characteristics of an underlying physical channel.

There exist numerous examples of modeling communication channels using renewal models, where typically the objective is to fit the independent run length distributions of a model to sample distributions obtained from measurements. Such examples span from the classic Gilbert [62] and simplified Fritchman models [74] to more recent studies, including the wideband code division multiple access (WCDMA) block error model of [52], the four-state run length model considered by McDougall et al. in [83], applying Weibull distributions to approximate sample run length distributions as proposed by Karner and Rupp in [84], and applying half-normal distributions as considered by the author in [12]. Notably, the Gilbert, simplified Fritchman, and WCDMA model proposed by Tralli and Zorzi [52, 62, 74] may be used for matching run length distributions for either error or error-free runs, but generally not both. The four-state run length model of [83] is structurally identical to a specific realization of the models described in Chapter 4 of this Thesis - the four-state run length model was also originally one motivation for considering the class of models specified in this work - but the

authors do not give analytical results on derivation of the model parameter values to achieve good simulation performance. The approach of [84] seems suitable for a wide range of applications due to the flexibility of the Weibull distribution. However, the authors do not consider determining the model parameters as functions of physical reception conditions.

In the following Chapter, finite-state error models are considered, which can be thought of as efficiently realizable alternating renewal processes with exponential mixture distributions. On the other hand, the models can be considered as generalizations of the simplified Fritchman model as specified in the previous Subsection. Finally, the four-state error model applied in Chapters 4 and 5 of this Thesis can also be treated as an aggregated Markov process related to the Gilbert-Elliott model, but with a state structure conditioned to enable efficient parameter estimation.

Chapter 4

Aggregated Renewal Markov Processes as Block/Packet Error Models

As presented in the previous Chapter, any discrete HMM can be modified into an equivalent AMP by increasing the number of states. Furthermore, in [60] the authors show that, assuming certain mild conditions on the transition probability matrix of an aggregated Markov process, a unique equivalent model can be obtained, where transition probabilities within a group of states corresponding to a given output symbol are represented by a diagonal matrix. In this Chapter such models are considered. According to [60] this partial diagonality of the state transition matrix is not a major limitation on the generality of a model. However, as defined in Section 4.1, rather strict conditions on the transition probabilities between state groups are also assumed, which does restrict the generality of the considered models. In Section 4.4, effects of these limitations on the performance of the defined models are evaluated.

The main contribution of this Chapter is to provide practical and efficient packet error models that allow approximating the model parameters according to time-variant reception conditions as indicated by the received signal strength and receiver velocity. To facilitate the implementation of these models, straightforward procedures are given for calculating the model parameters. The usefulness of the discussed models is considered in simulating mobile reception using digital video broadcasting for handheld devices. In this case the packet channel models describe the behavior of transport stream packets entering the DVB-H link layer. Relevant properties of the DVB-H system are described in Appendix B.

The Chapter is organized as follows. First, in Section 4.1, the considered class of finite-state models is described, and expressions for specific

properties of models in this class are derived. These properties are then used in Section 4.2 to determine the parameters for three simple models. In Section 4.3, measured DVB-H error traces are described and subsequently utilized in simulations in Section 4.4 to evaluate the accuracy of the considered models. In Section 4.5 an approach to parameterizing the models according to the average CNR and maximum Doppler frequency of the underlying physical channel is suggested.

The majority of results considered in the following Chapter were originally presented, along with intermediate results and additional motivation, in references [10–16], each having the author of this Thesis as the main contributor.

4.1 Aggregated Renewal Markov Processes

Let $\{S_t\}_{t\in\mathbb{T}}$ be a time homogenous Markov chain with a finite state space $\mathbb{S} = \{1, 2, \ldots, N+M\}$, partitioned into subsets $C: \{1, ..., N\}$ and $E: \{N+1, ..., N+M\}$. The observation process corresponding to the state sequence $\{S_t\}_{t\in\mathbb{T}}$ is again $\{Y_t\}_{t\in\mathbb{T}}$ with state space $\mathbb{Y} = \{c, e\}$. Defining the emission function $\phi : \mathbb{S} \mapsto \{c, e\}$ as $\phi(i) = c\ \forall i \in C,\ \phi(i) = e\ \forall i \in E$, $\{S_t\}$ and $\{Y_t\}$ form an aggregated Markov process as specified in the previous Chapter.

In the following it is assumed that the transition matrix $\mathbf{A} = [a_{i,j}]_{i,j\in\mathbb{S}}$ of $\{S_t\}$ is of the form

$$\mathbf{A} = \begin{pmatrix} \mathbf{A}_{CC} & \mathbf{A}_{CE} \\ \mathbf{A}_{EC} & \mathbf{A}_{EE} \end{pmatrix} \tag{4.1}$$

where

$$\begin{aligned} (i)\ \ & \mathbf{A}_{CC} = diag(\alpha_1, ..., \alpha_N), \\ (ii)\ \ & \mathbf{A}_{EE} = diag(\alpha_{N+1}, ..., \alpha_{N+M}), \\ (iii)\ \ & \mathbf{A}_{CE} = [a_{ij}]_{i\in C, j\in E} = [(1-\alpha_i)w_j]_{i\in C, j\in E}, \\ (iv)\ \ & \mathbf{A}_{EC} = [a_{ij}]_{i\in E, j\in C} = [(1-\alpha_i)w_j]_{i\in E, j\in C}, \\ & \alpha_i \in [0, 1]\ \forall i \end{aligned}$$

and

$$\sum_{i\in C} w_i = \sum_{i=1}^{N} w_i = 1,\ \sum_{i\in E} w_i = \sum_{i=N+1}^{N+M} w_i = 1. \tag{4.1a}$$

Conditions (i) and (ii) above imply that transitions between different correct states (states in subset C) are forbidden as well as transitions between error states (states in subset E). Combined with the previous, conditions (iii) and (iv) result in the property that the joint probabilities $P(S_t = i, S_{t+1} = j),\ j \in E$ are equal for all $i \in C$, assuming j is fixed. Conversely, joint probabilities $P(S_t = i, S_{t+1} = j),\ j \in C$ are equal for all

$i \in E$, assuming j is fixed. This may not be evident from the expressions above, but is readily obtained from subsequently derived results. According to reference [60], conditions (i) and (ii) are not a major limitation on the generality of the model. However, this is not true for (iii) and (iv); the effect of these restrictions will be considered in Sections 4.2 and 4.4. In the following, equation (4.1) is used to determine the limiting state probabilities for the model. Subsequently, the probability distributions of the lengths of sequences of consecutive symbols c and e are derived. Finally, to assist in determining the model parameter values in Section 4.2, the kth derivatives of the probability generating functions of these probability distributions are calculated.

Given (4.1), the limiting probabilities $\vec{\pi} = (\pi_1, ..., \pi_{N+M})$ of S_t are obtained by definition ($\vec{\pi}\mathbf{A} = \vec{\pi}$):

$$\pi_i = \begin{cases} \alpha_i\pi_i + \sum_{k=1,k\neq i}^{N} 0 \cdot \pi_k + \sum_{l=N+1}^{N+M}(1-\alpha_l)w_i\pi_l, & i \in C \\ \alpha_i\pi_i + \sum_{k=N+1,k\neq i}^{N+M} 0 \cdot \pi_k + \sum_{l=1}^{N}(1-\alpha_l)w_i\pi_l, & i \in E \end{cases}$$

$$\Leftrightarrow \pi_i = \begin{cases} \frac{w_i}{1-\alpha_i}A, & i \in C \\ \frac{w_i}{1-\alpha_i}B, & i \in E \end{cases},$$

where $A = \sum_{i\in E}(1-\alpha_i)\pi_i$, $B = \sum_{i\in C}(1-\alpha_i)\pi_i$. Multiplying the previous by $(1-\alpha_i)$ and summing over $i \in C$, equation (4.1a) gives

$$\sum_{i\in C}(1-\alpha_i)\pi_i = \sum_{i\in C} w_i A \Rightarrow B = A,$$

so that

$$\pi_i = \frac{w_i A}{1-\alpha_i} \ \forall i,$$

and since

$$\sum_i \pi_i = A\sum_i \frac{w_i}{1-\alpha_i} = 1 \Rightarrow A = \frac{1}{\sum_i \frac{w_i}{1-\alpha_i}},$$

the limiting probabilities are obtained as

$$\pi_i = \frac{w_i}{(1-\alpha_i)\left(\sum_{k=1}^{N+M}\frac{w_k}{1-\alpha_k}\right)} \forall i \in \{1, ..., N+M\} \tag{4.2}$$

Now let T_C and T_E be discrete random variables corresponding to the dwell times in state subsets C and E, respectively. The probability distributions for T_C and T_E are denoted $f_C(n)\hat{=}P(T_C = n)$ and $f_E(n)\hat{=}P(T_E = n)$, and defined as

$$f_C(n) = P(S_{k+2} \in C, ..., S_{k+n} \in C, S_{k+n+1} \notin C | S_k \in E, S_{k+1} \in C)$$

$$= \frac{P(S_k \in E, S_{k+1} \notin E, S_{k+2} \in C, ..., S_{k+n} \in C, S_{k+n+1} \notin C)}{P(S_k \in E, S_{k+1} \in C)}$$

$$= \frac{\sum_{i=N+1}^{N+M} \pi_i \sum_{j=1}^{N} p_{ij} p_{jj}^{n-1}(1 - p_{jj})}{\sum_{i=N+1}^{N+M} \pi_i (1 - p_{ii})}$$

$$= \frac{\sum_{i=N+1}^{N+M} \pi_i (1 - \alpha_i) \sum_{j=1}^{N} w_j \alpha_j^{n-1}(1 - \alpha_j)}{\sum_{i=N+1}^{N+M} \pi_i (1 - \alpha_i)}$$

$$= \sum_{j=1}^{N} w_j \alpha_j^{n-1}(1 - \alpha_j) \ \forall \ n \in \{1, 2, ...\} \tag{4.3}$$

and, exchanging E and C in the definition of $f_C(n)$,

$$f_E(n) = \sum_{j=N+1}^{N+M} w_j \alpha_j^{n-1}(1 - \alpha_j) \ \forall \ n \in \{1, 2, ...\}. \tag{4.4}$$

It can thus be seen that T_C and T_E follow geometric mixture distributions. This result was given already by Fritchman in reference [74] for generic binary aggregated Markov processes, however the derivation given above for the considered special case is somewhat more straightforward than the general approach of reference [74]. Also, in this case T_C and T_E are clearly independent of each other and of time index k, since $\{S_t\}$ was determined to be a time homogenous stochastic process. Thus the considered models can be classified as alternating renewal processes, motivating use of the term *aggregated renewal Markov process* (ARMP).

Finally, the probability generating functions of (4.3) and (4.4) are found to be of the form

$$G(z) = \sum_{k=1}^{\infty} z^k \sum_j w_j (1 - \alpha_j) \alpha_j^{k-1}$$

$$= \sum_j \frac{w_j (1 - \alpha_j)}{\alpha_j} \sum_{k=1}^{\infty} (z\alpha_j)^k$$

$$= \sum_j \frac{w_j (1 - \alpha_j) z}{1 - z\alpha_j}. \tag{4.5}$$

Depending on the range of summation in (4.5), either pgf $G_C(z)$ for $f_C(n)$ ($j \in \{1, 2, ..., N\}$), or pgf $G_E(z)$ for $f_E(n)$ ($j \in \{N + 1, ..., N + M\}$) is obtained.

$G(z)$ is of the form $\sum_j C_j \cdot f_j(z)$, where $C_j = \frac{w_j(1-\alpha_j)}{\alpha_j}$ and $f_j(z) = \frac{\alpha_j z}{1-\alpha_j z}$. Now the kth derivative of $f_j(z)$ is obtained as

$$f_j^{(k)}(z) = \frac{d^{k-1}}{dz^{k-1}}\left[f_j'(z)\right]$$

$$= \frac{d^{k-1}}{dz^{k-1}}\left[\frac{\alpha_j(1-\alpha_j z) - \alpha_j z(-\alpha_j)}{(1-\alpha_j z)^2}\right]$$

$$= \alpha_j \frac{d^{k-1}}{dz^{k-1}}\left[(1-\alpha_j z)^{-2}\right] = \alpha_j^k \cdot k!(1-\alpha_j z)^{-(k+1)}.$$

Thus

$$G^{(k)}(z) = \sum_j \frac{k!\alpha_j^{k-1} w_j(1-\alpha_j)}{(1-z\alpha_j)^{k+1}} \;\forall\; k \in \{1,2,...\}. \tag{4.6}$$

Again, different ranges of j produce either $G_C^{(k)}(z)$ or $G_E^{(k)}(z)$. In the following Section, methods of determining the transition matrix given in (4.1) from observed error processes are considered. For this, the general results obtained in this Section, namely equations (4.6) and (4.2) are used.

4.2 Realizations

The ARMP described in Section 4.1 is used to model observed error processes in given communication systems as follows: let $\{Q_n\}_{n\in\{1,...,l_Q\}}$ be the average quality of signal reception, defined by a criterion natural to the system under inspection, during l_Q measured sampling intervals. In the following it is assumed that the signal quality can be quantized so that $Q_n \in \{q_C, q_E\}\ \forall n \in \{1,...,l_Q\}$, where q_C and q_E correspond to correct and erroneous reception, respectively. Then one can try to fit the parameters of the aggregated Markov process defined in the previous Section to provide best possible consistence between modeled sequences of states $\{c, e\}$ and experimental sequences of $\{q_C, q_E\}$ according to some relevant criteria.

If the probability of error in the system under inspection is defined as

$$P(q_E) = \frac{\sum_{i=1}^{l_Q} \delta(Q_i, q_E)}{l_Q},$$

where $\delta(a,b)$ is the Kronecker symbol:

$$\delta(a,b) = \begin{cases} 1, & a = b, \\ 0, & a \neq b, \end{cases}$$

then it is reasonable to require $\{S_t\}$ to be determined so that

$$P(Y_t = e) = \sum_{i\in E} \pi_i = P(q_E). \tag{4.7}$$

Furthermore, if the length of the ith sequence of consecutive symbols q_E (referred to as error runs) in $\{Q_n\}$ is denoted as L_E^i and the length of the jth sequence of consecutive symbols q_C (correct runs) in $\{Q_n\}$ as L_C^j, then ideally L_E^i and L_C^j would be accurately approximated by T_E and T_C, defined in Section 4.1. However, as stated before, T_E and T_C are independent stationary random variables. While it can in many cases be assumed that $\{Q_n\}$ is stationary in the sense that the distributions of L_E^i and L_C^j are not time-dependent (see Section 4.3), given the rather strict conditions of (4.1) it is not generally possible to model the correlation properties of L_E^i and L_C^j. Another inherent limitation in the model is due to the probability distributions of T_E and T_C, which were shown in Section 4.1 to be geometric mixture distributions. Again, it can not be generally assumed that this applies also to L_E^i and L_C^j. However, increasing the number of states in the model, and thus the number of free parameters, potentially improves the accuracy of modeling the observed distributions.

Effects of the limitations described above are considered in more detail in Section 4.4; given these limitations, in the following functional methods of determining the model parameters from observed error processes are investigated. Initially a model with only two states ($N = 1$, $M = 1$ as defined in Section 4.1) is considered. Subsequently the advantage of increasing the number of states is studied.

4.2.1 Two States

In the simplest case, $C = \{1\},\ E = \{2\}$, which gives $w_1 = w_2 = 1$ and

$$\mathbf{A} = \begin{pmatrix} \alpha_1 & 1-\alpha_1 \\ 1-\alpha_2 & \alpha_2 \end{pmatrix}.$$

From (4.2) and (4.7) the condition

$$P(Y_t = e) = \pi_2 = \frac{1}{1 + \frac{1-\alpha_2}{1-\alpha_1}} = P(q_E)$$

is immediately obtained. From (4.6) it is seen that $\mu_C \hat{=} \sum_n n f_C(n) = G_C^{(1)}(1) = \frac{1}{1-\alpha_1}$ and $\mu_E \hat{=} \sum_n n f_E(n) = G_E^{(1)}(1) = \frac{1}{1-\alpha_2}$, so that the previous condition on the ARMP is equivalent to

$$\frac{1}{1 + \frac{\mu_C}{\mu_E}} = P(q_E). \tag{4.8}$$

Note that regardless of the actual distributions of L_E^i and L_C^j, the following holds:

$$P(q_E) = \frac{\sum_{i=1}^m L_E^i}{\sum_{i=1}^m L_E^i + \sum_{j=1}^m L_C^j},$$

assuming that $\{Q_n\}$ contains m correct and m error runs, and thus $l_Q = \sum_{i=1}^{m} L_E^i + \sum_{j=1}^{m} L_C^j$. If it is assumed that the distributions of L_E^i and L_C^j are not time-dependent, as m grows

$$P(q_E) \approx \frac{m\overline{L}_E}{m\overline{L}_E + m\overline{L}_C} = \frac{1}{1 + \frac{\overline{L}_C}{\overline{L}_E}},$$

where $\overline{L}_C$ and $\overline{L}_E$ denote the sample means of L_C and L_E. Comparing this with (4.8) it is seen that with the two-state model, reproducing a measured probability of error is accomplished by matching the mean run lengths of $\{Y_t\}$ and $\{Q_n\}$. In practice, this means using the method of moments to fit the run length distributions so that both the probability of error and mean run lengths are accurately modeled. Thus a very simple form for parameter estimation is obtained:

$$\overline{L}_C \hat{=} \mu_C = \frac{1}{1-\alpha_1} \Leftrightarrow \alpha_1 = \frac{\overline{L}_C - 1}{\overline{L}_C}, \tag{4.9}$$

$$\overline{L}_E \hat{=} \mu_E = \frac{1}{1-\alpha_2} \Leftrightarrow \alpha_2 = \frac{\overline{L}_E - 1}{\overline{L}_E}. \tag{4.10}$$

Note that this is certainly not the only way of choosing the parameters to match the observed error rate; trivially one could choose $\alpha_2 = P(q_E)$ and $\alpha_1 = 1 - \alpha_2$, which results in $\{Y_t\}$ being equivalent to the error process of a binary symmetric channel. This accurately estimates the observed probability of error, but completely disregards the effect of channel memory.

Furthermore, it can be experimentally shown that the parameter estimation given by (4.9) and (4.10) is not always a good solution in terms of simulation performance. In Section 4.4 it is shown through simulations that the following parameter estimation gives a more useful model: let $S_{L_C}^2$ and $S_{L_E}^2$ be the sample variances of the observed run lengths. The model parameters are now selected according to

$$\sigma_C^2 = G_C^{(2)}(1) + G_C^{(1)}(1) - \left[G_C^{(1)}(1)\right]^2 = \frac{\alpha_1}{(1-\alpha_1)^2} \hat{=} S_{L_C}^2,$$

$$\sigma_E^2 = G_E^{(2)}(1) + G_E^{(1)}(1) - \left[G_E^{(1)}(1)\right]^2 = \frac{\alpha_2}{(1-\alpha_2)^2} \hat{=} S_{L_E}^2,$$

which yield

$$\alpha_1 = \frac{2 + \frac{1}{S_{L_C}^2} - \frac{1}{S_{L_C}}\sqrt{4 + \frac{1}{S_{L_C}^2}}}{2}, \tag{4.11}$$

$$\alpha_2 = \frac{2 + \frac{1}{S_{L_E}^2} - \frac{1}{S_{L_E}}\sqrt{4 + \frac{1}{S_{L_E}^2}}}{2}, \tag{4.12}$$

due to the fact that $\alpha_1, \alpha_2 \in [0, 1]$.

However, with only two states in the model, fitting one parameter accurately (in this case the variance) generally results in a poor fit for other parameters (mean run lengths and error probability), due to the lack of degrees of freedom in determining the model. In the following, the number of states is increased in order to obtain more flexible models for $\{Q_n\}$.

4.2.2 Four States

To retain the accuracy of the run length variance estimation, while generally reproducing also the measured error rate and mean run lengths, additional degrees of freedom in determining the model parameters are required. Accurate modeling of run length variances will be shown to be important in terms of simulation performance, or obtaining simulation results that correspond well with measurements. Therefore a model with $C = \{1, 2\}$ and $E = \{3, 4\}$ is considered. Thus

$$\mathbf{A} = \begin{pmatrix} \alpha_1 & 0 & (1-\alpha_1)w_3 & (1-\alpha_1)w_4 \\ 0 & \alpha_2 & (1-\alpha_2)w_3 & (1-\alpha_2)w_4 \\ (1-\alpha_3)w_1 & (1-\alpha_3)w_2 & \alpha_3 & 0 \\ (1-\alpha_4)w_1 & (1-\alpha_4)w_2 & 0 & \alpha_4 \end{pmatrix}$$

and, from (4.1a), (4.2), and (4.7),

$$P(Y_t = e) = \pi_3 + \pi_4$$

$$= \frac{w_3}{(1-\alpha_3)\left(\sum_{k=1}^{4} \frac{w_k}{1-\alpha_k}\right)} + \frac{1-w_3}{(1-\alpha_4)\left(\sum_{k=1}^{4} \frac{w_k}{1-\alpha_k}\right)}.$$

Keeping for expectations and variations of T_C and T_E the same designations as in the previous subsection, equation (4.6) gives:

$$\mu_C = G_C^{(1)}(1) = \frac{w_1}{1-\alpha_1} + \frac{(1-w_1)}{1-\alpha_2},$$

$$\mu_E = G_E^{(1)}(1) = \frac{w_3}{1-\alpha_3} + \frac{(1-w_3)}{1-\alpha_4},$$

$$\sigma_C^2 = G_C^{(2)}(1) + G_C^{(1)}(1) - \left[G_C^{(1)}(1)\right]^2$$

$$= \frac{w_1\alpha_1(1-\alpha_2)^2 + w_2\alpha_2(1-\alpha_1)^2 + w_1w_2(\alpha_2-\alpha_1)^2}{(1-\alpha_1)^2(1-\alpha_2)^2},$$

and

$$\sigma_E^2 = G_E^{(2)}(1) + G_E^{(1)}(1) - \left[G_E^{(1)}(1)\right]^2$$

$$= \frac{w_3\alpha_3(1-\alpha_4)^2 + w_4\alpha_4(1-\alpha_3)^2 + w_3w_4(\alpha_4-\alpha_3)^2}{(1-\alpha_3)^2(1-\alpha_4)^2}.$$

Using the previous, the model parameters can now be selected by solving $\{\alpha_1, \alpha_2, \alpha_3, \alpha_4, w_1, w_3\}$ in the following group of equations:

$$\begin{cases} P(Z=e) = P(q_E) \\ \mu_C = \overline{L}_C \\ \mu_E = \overline{L}_E \\ \sigma_C^2 = S_{L_C}^2 \\ \sigma_E^2 = S_{L_E}^2 \end{cases} \tag{4.13}$$

Although (4.13) is an underdetermined (there are less linearly independent equations than the number of unknown variables to be solved) system of nonlinear equations with no explicit solution, working solutions may be obtained using numerical methods such as the Levenberg-Marquardt algorithm [85, 86], an implementation of which is available in standard mathematical software packages.

Equation (4.13) above was derived by the author in reference [16] for solving the parameters of the four-state error model. It should be noted that while the solution presented above produces correct results, it can be further simplified, which has been found to significantly improve both the accuracy and the speed of numerically determining the model parameters. As shown in Subsection 4.2.1, the measured probability of error can be reproduced by matching the theoretical mean run lengths of the error model with sample mean run lengths of the measured error trace. Thus the first equation in (4.13) is redundant, and can be removed. Now, solving the model parameters reduces to independently solving the following two pairs of equations:

$$\begin{cases} \frac{w_1}{1-\alpha_1} + \frac{(1-w_1)}{1-\alpha_2} = \overline{L}_C \\ \frac{w_1\alpha_1(1-\alpha_2)^2 + (1-w_1)\alpha_2(1-\alpha_1)^2 + w_1(1-w_1)(\alpha_2-\alpha_1)^2}{(1-\alpha_1)^2(1-\alpha_2)^2} = S_{L_C}^2 \end{cases} \tag{4.14}$$

$$\begin{cases} \frac{w_3}{1-\alpha_3} + \frac{(1-w_3)}{1-\alpha_4} = \overline{L}_E \\ \frac{w_3\alpha_3(1-\alpha_4)^2 + (1-w_3)\alpha_4(1-\alpha_3)^2 + w_3(1-w_3)(\alpha_4-\alpha_3)^2}{(1-\alpha_3)^2(1-\alpha_4)^2} = S_{L_E}^2 \end{cases} \tag{4.15}$$

Compared to (4.13), solutions for (4.14) and (4.15) can be found more efficiently using the same numerical algorithm.

4.2.3 Other Numbers of States

It should be noted that if equations (4.9) and (4.11) both result in approximately the same value for α_1, or correspondingly equations (4.10) and (4.12) both give approximately the same value for α_2, then in the first case only one

state with output c and in the second case only one state with output e is needed in the model, assuming the parameter estimation described above. In these cases, the obtained model corresponds to the typical simplified Fritchman model with either a single error-free state or a single error state. Still, the model parameter estimation approach presented in this Section can be applied with suitable modifications.

While the moment-based evaluation of the model parameters is efficient and feasible with a four-state implementation of the hidden Markov model structure considered, it is clear that further increasing the number of states complicates the parameter evaluation. Therefore it is relevant to determine whether there is any advantage gained from such increase in complexity. In Section 4.4 it is shown through simulations that with the digital video broadcasting system considered in this work, a four-state model produces simulation results that would not be significantly improved by increasing the number of states, given the restrictions of equation (4.1). This follows from the renewal property of the model, which means that increasing the number of states only potentially improves the fit of the model output run length distributions to the measured. Simulations imply that the differences between results obtained using a renewal model that closely approximates the measured sample run length distributions, and those obtained using the four-state model are negligible when considering simulation performance. It should be noted that this is a significant difference between the aggregated renewal processes considered in this work and general aggregated Markov processes, where increasing the number of states in the model potentially improves the maximum likelihood estimation of the model transition probabilities from the given measurement. In the context of this Thesis, models with more than four states will not be considered.

4.3 Characterization of the Observed Error Process

To evaluate the performance of the error models described in Sections 4.1 and 4.2, it is necessary to consider realizations of the error process $\{Q_n\}$. In this Thesis, $\{Q_n\}$ is defined as a sequence of packet error indicators for transport stream (TS) packets at the link layer of a DVB system for handheld terminals (DVB-H). In the following the measurement setups used to obtain the TS packet error traces required in simulating the DVB-H link layer performance are briefly described, and the required laboratory measurement lengths to obtain sufficient information on the statistics of the channel are determined. A description of DVB-H, and related link layer forward error correction for multiprotocol encapsulated data is presented in Appendix B.

4.3.1 Obtaining Packet Error Traces

DVB-T/H transport stream error traces were obtained in a laboratory setting by inputting MPEG-2 [87] source data into a DVB-T/H modulator operating with various combinations of system parameters. In all considered cases, 8K OFDM mode and 1/4 cyclic prefix length are used. The modulated signal was passed through a hardware channel simulator that used the COST 207 typical urban six-tap (TU6) WSSUS channel model [34,88]. Noise was then added to the signal to obtain various average carrier-to-noise ratio values. The noisy signal was input into a DVB-T/H receiver and subsequent logic analyzer to produce TS packet error traces. These traces correspond to $\{Q_n\}$ as defined in Section 4.2 with the observation period corresponding to one TS packet and the quantization of the signal quality performed according to the number of byte errors before physical layer outer decoding in each received TS packet. That is, $Q_n = q_E$ if the nth TS packet contains more than eight byte errors, which is the correction capability of the physical layer outer decoder in DVB-H as presented in Appendix B. Otherwise the TS packet will be decoded correctly, and by definition $Q_n = q_C$.

4.3.2 Required Measurement Lengths

In estimating the error model parameters in Section 4.2, it was assumed that the run length distributions L_C and L_E are stationary. In the laboratory measurements, the error traces were obtained using a wide-sense stationary channel model with a fixed carrier-to-noise ratio and Doppler frequency per measurement. Thus it is reasonable to assume that in this case the run length distributions are stationary and, given a sufficiently large observation window, or length l_Q of the sequence $\{Q_n\}$, the measured sample run length distributions are consistent estimators of these stationary distributions. Still, it is not evident how long the measured error traces should be to provide a reliable estimate of the statistics of the channel. In other words, the observation length necessary to obtain consistent estimates of the error statistics used to solve the model parameters should be considered.

To determine the minimum measurement length required, the variance of sample mean run lengths of DVB-H TS packet error traces was evaluated by the author in reference [16] using the *runs test*, following the example of reference [81]. As defined in Section 4.2, the term "run" refers to a series of consecutive error-free or erroneous packets. The principle of the runs test is to divide the measured error trace into segments of equal lengths, compute the lengths of runs in each segment, count the number of runs of length above and below the median value for run lengths in the trace, and finally compute a histogram for the number of runs counted. Now it was defined that a trace has sufficiently constant mean run lengths with the

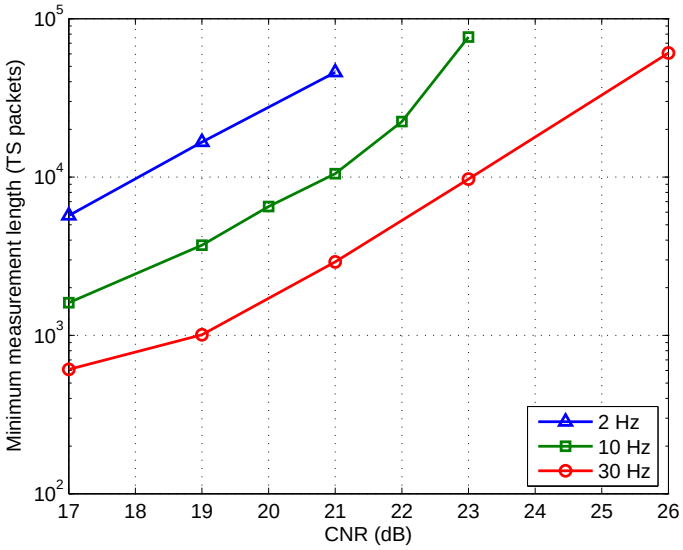

Figure 4.1: Estimations of the required measurement lengths to obtain small variance in sample mean error run length.

given segment length, when the number of runs between the 0.05 and 0.95 cutoffs is close to 90 %.

To approximate the minimum error trace lengths required to obtain sufficiently constant estimates for the relevant error statistics, long measurements (length of order $> 10^6$ TS packets) were analyzed by applying the runs test with increasingly long segment lengths, until the number of runs between the specified cutoffs was 90 %. Figure 4.1 shows results of this approximation obtained in [16] for several values of CNR and Doppler frequency (16-QAM modulation, convolutional code rate 2/3). It is physically obvious and supported by Figure 4.1 that the required minimum trace length grows with increasing CNR and decreasing Doppler frequency.

It is relevant to investigate in more detail what the approximations given above for minimum measurement length signify in terms of the consistency of the sample statistics necessary to construct the error models considered in this Chapter. Figure 4.2 shows the standard deviation of the relevant statistics as a packet error measurement (maximum Doppler frequency 10 Hz, CNR 17 dB, corresponding to Figure 4.1) is partitioned into segments, and the set of statistics is separately calculated for each segment. This is repeated for a range of segment, or observation window, lengths. The standard deviation values are given relative to the average of each considered statistic over the entire measurement. Since the relative standard deviation curves converge quite rapidly as the window size increases, it seems justified

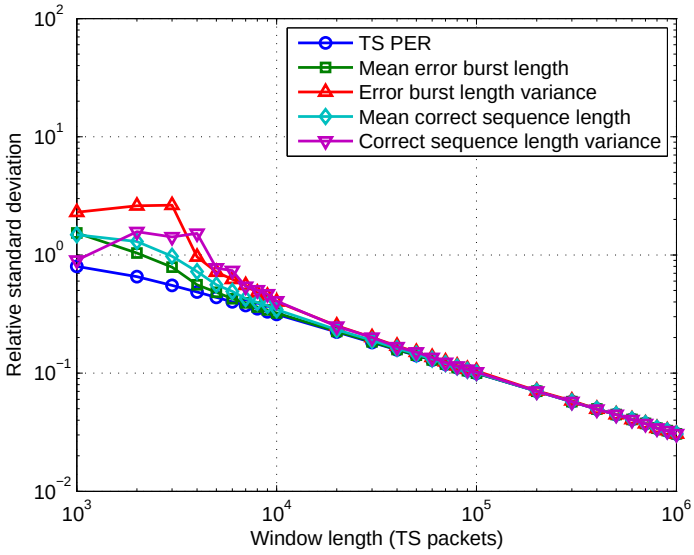

Figure 4.2: Decrease of the standard deviation of relevant statistics as a DVB-H TS packet error measurement (16-QAM, convolutional cr 2/3, maximum Doppler frequency 10 Hz, CNR 17 dB) is partitioned into segments, or observation windows, of increasing length. The given standard deviation values are relative to the average of each considered statistic over the entire measurement.

to use the standard deviation of the TS packet error rate to represent the entire set of necessary statistics, as done in the following.

Figure 4.3 shows the decrease in relative standard deviation of the TS PER as the window length increases, for the same transmission parameter configuration as considered above. Comparing the obtained results with Figure 4.1, it is clear that the criteria for determining minimum required measurement lengths using the runs test as described above are relatively loose. Selecting measurement lengths strictly according to Figure 4.1 results in measurement sets for which the standard deviation of the average TS PER is approximately of the same magnitude as the assumed correct, or asymptotic, value. It is also demonstrated in Figure 4.3 that allowing for a 10 % relative standard deviation of the TS PER results in a more strict minimum measurement length of approximately 10^5 TS packets for all of the considered cases.

Figures 4.4 and 4.5 show results obtained by repeating the above analysis for DVB-H measurements with 16-QAM, convolutional code rate 1/2. This transmission parameter configuration is of primary relevance for this Thesis, as it will be assumed in parameterizing the considered error models later in

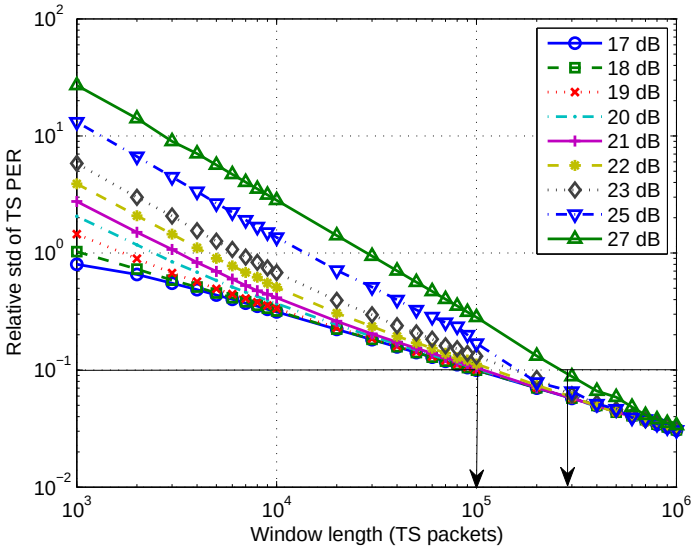

Figure 4.3: Relative standard deviations of TS packet error rates as functions of the observation window length for 16-QAM, convolutional cr 2/3, maximum Doppler frequency 10 Hz.

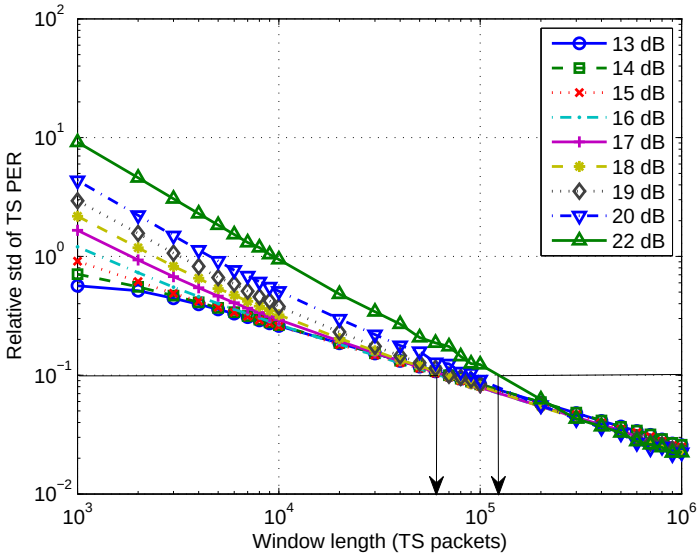

Figure 4.4: Relative standard deviations of TS packet error rates as functions of the observation window length for 16-QAM, convolutional cr 1/2, maximum Doppler frequency 10 Hz.

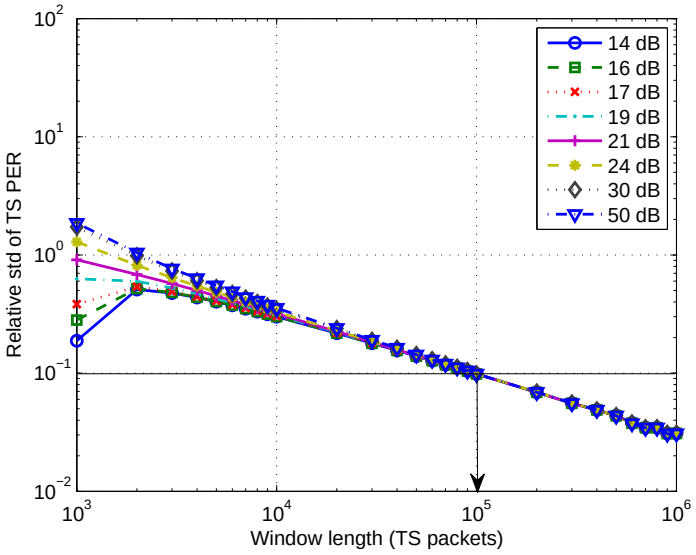

Figure 4.5: Relative standard deviations of TS packet error rates as functions of the observation window length for 16-QAM, convolutional cr 1/2, maximum Doppler frequency 80 Hz.

this Chapter, and in the system simulation case study of Chapter 5. The results shown in Figures 4.4 and 4.5 for maximum Doppler frequencies 10 and 80 Hz, respectively, indicate that assuming a 10 % relative standard deviation criterion for the TS PER again results in a minimum measurement length of approximately 10^5 TS packets for all of the considered cases. The order of magnitude for lengths of all laboratory measurements utilized in the subsequent work is 10^6 TS packets, which should be sufficient for all considered cases based on the results presented above.

4.4 Evaluation of the Model Performance

4.4.1 Transport Stream Packet Error Simulations

In the following the effects of the inherent limitations of the error model as described in Section 4.2 on the accuracy of the model in DVB-H link layer simulations are considered. In this case accuracy is measured as the difference in error rates obtained in simulations using measured error traces compared to simulations using error traces generated with stochastic models. More specifically, the deterioration of model accuracy due to the use of geometric mixture distributions to approximate measured run lengths is considered.

To evaluate the effect of assuming certain distributions for the run lengths in modeling measured error traces, ideally the model in question would be compared to a model where the generated run lengths are drawn from the underlying run length distributions of the measurements. Of course it is impossible to sample directly these underlying distributions, but approximations can be found using the sample distributions of L_C and L_E defined in Section 4.2. It should be stressed that the objective here is to evaluate the best performance within the class of renewal models, where the run length distributions are independent and time-homogenous. For this, a modification of the discrete time analog of the inverse transformation technique [89] is used, and samples are obtained according to a given sample run length distribution for random variable L as follows: denote $P(L = l_j) \hat{=} P_j$, and let U be uniformly distributed over (0,1). Assuming k different lengths of runs are present in the observation, set

$$L = \begin{cases} l_1, & \text{if } U < P_1 \\ l_2, & \text{if } P_1 < U < P_1 + P_2 \\ \vdots & \\ l_k, & \text{if } \sum_{j=1}^{k-1} P_i < U < 1 \end{cases} \tag{4.16}$$

Note that P_j, where $j \in \{1, ..., k\}$, are easily calculated from measurements as the sample frequencies of lengths of runs. By applying the previous for L_C and L_E until a sufficiently long approximation of $\{Q_n\}$ is obtained, error traces with independent time-homogenous run length distributions that closely match the given sample distributions are produced. This can also be seen in Figure 4.9, where the sample distribution of error burst lengths of a measurement is compared to that of an error trace generated as described above. The measured error traces used in the following were obtained as laboratory measurements with a 16-QAM modulation mode, 1/4 OFDM guard interval length, 8K FFT length, 1/2 , 2/3 and 3/4 physical layer convolutional code rates, and 10 and 80 Hz Doppler frequencies for the TU6 channel model applied in the physical layer. The DVB-H multiprotocol encapsulation-forward error correction (MPE-FEC) code rate used in the simulations was 3/4. It should be noted that, as described in [90], a typical error criterion used for sufficient reception of DVB-H is the MPE-FEC frame error rate 5%, around which the given simulation results are focused.

Figures 4.6, 4.7, and 4.8 show the simulated TS packet error rates, MPE-FEC frame error rates, and IP packet error rates for physical layer code rate 1/2 and 10 Hz Doppler, obtained with finite-state models as described in Section 4.2 and the discrete inverse transformation method described above. Since all of the considered models accurately reproduce the TS packet error rates of the measurements as seen from Figure 4.6, Figures 4.7 and 4.8 demonstrate the effect of taking into account the various run length statis-

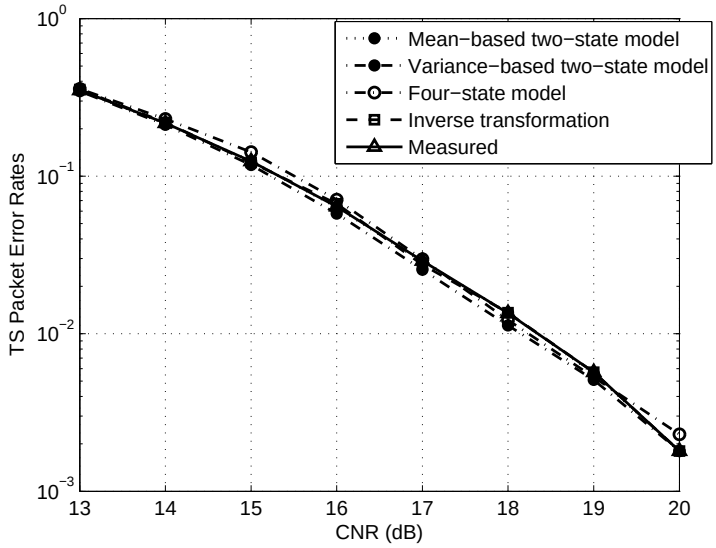

Figure 4.6: Simulated DVB-H TS packet error rates with 16-QAM modulation, physical layer code rate 1/2 and 10 Hz Doppler.

tics on the higher protocol layer error performance. Furthermore, for these examples comparison of simulation results with the inverse transformation model indicates that with the four-state ARMP, the adverse effect of the assumed run length distribution on the simulation accuracy of the model is negligible. Naturally the difference between the two-state models and the inverse transformation is much larger; still it can be seen that using the variance-based parameter estimation suggested in Section 4.2 produces more accurate results than conventional mean-based estimation.

Comparing simulation results with those obtained using the inverse transformation, it was found that in the considered DVB-H cases, little advantage remains to be gained by increasing the number of states in an aggregated renewal Markov process beyond four, or even by applying renewal models with other run length distributions. This is further illustrated in Figure 4.9, where it is shown that the four-state ARMP produces a good fit to the measured error burst length distribution. However, from Figure 4.7 it is not immediately obvious whether the simulation performance of the four-state model is sufficiently better than that of the two-state model to justify the corresponding increase in complexity of calculating the model parameter values. Figure 4.10 shows a comparison of simulated MPE-FEC frame error rates with physical layer code rates 2/3 and 3/4, and Doppler frequencies 10 and 80 Hz. It can be seen from the Figure that in the considered cases, the four-state model consistently produces more accurate simulation results

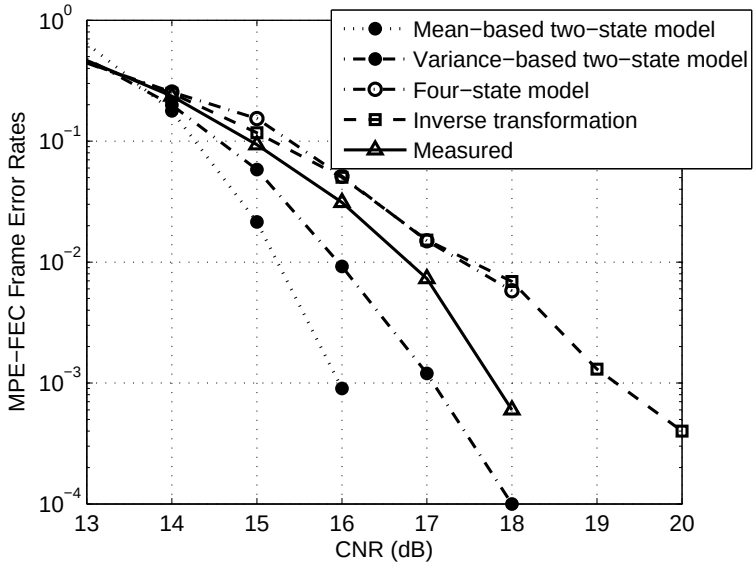

Figure 4.7: Simulated DVB-H MPE-FEC frame error rates with 16-QAM modulation, physical layer code rate 1/2 and 10 Hz Doppler, MPE-FEC code rate 3/4.

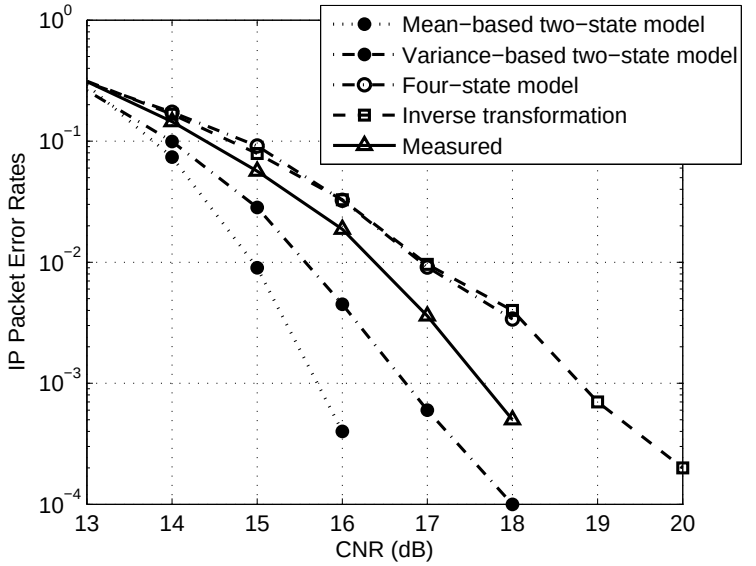

Figure 4.8: Simulated DVB-H IP packet error rates with 16-QAM modulation, physical layer code rate 1/2 and 10 Hz Doppler, MPE-FEC code rate 3/4.

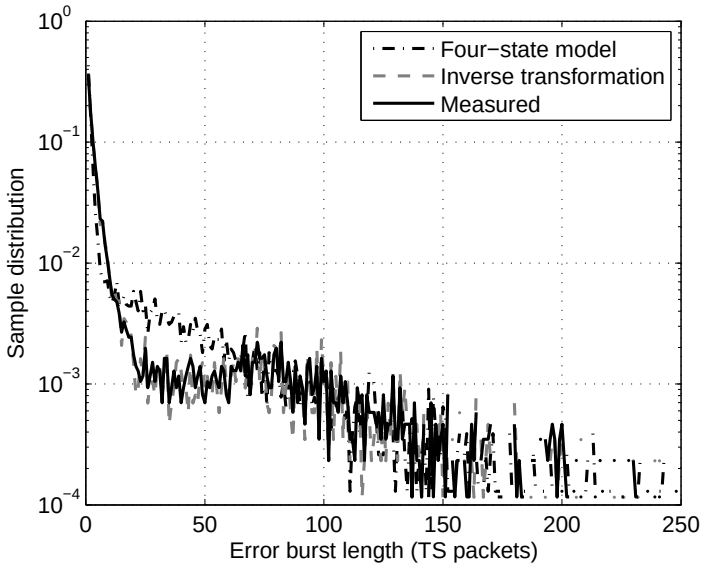

Figure 4.9: Comparison of sample distributions of TS packet error burst lengths for 16-QAM, code rate 1/2, 10 Hz Doppler at CNR 17 dB.

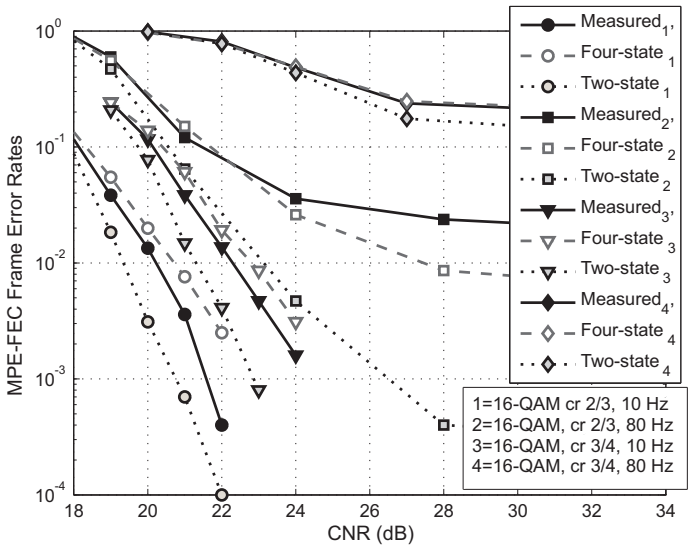

Figure 4.10: Comparison of simulated DVB-H MPE-FEC frame error rates with an MPE-FEC code rate 3/4 using the four-state model and the variance-based two-state model.

than the two-state model. This improvement in accuracy is most evident in the high Doppler frequency simulations. Since the increase in complexity of determining the parameters of the four-state model is manageable using suitable numerical methods, and implementation of the model itself is not significantly more complex than the two-state model, it can be stated that especially for the difficult mobile reception scenarios considered in this work the four-state aggregated Markov process is preferable over the variance-based two-state process.

It is noted that there is margin for improvement in simulation performance of the considered models, especially with very low error rates as can be seen in Figures 4.7 and 4.10, but such improvement is achieved at the cost of increased model evaluation complexity by using maximum likelihood evaluation of more general (non-renewal) hidden Markov models. In Section 4.5, parameterization of the models presented in this Chapter is considered, and in Chapter 5 it is shown in more detail that useful results can be obtained regardless of the inherent limitations of the models.

4.4.2 IP-Level Simulations

The hidden Markov models considered above can also be applied in internet protocol (IP)-level simulations of video streaming using DVB-H for data transmission. In [91], Känkänen compares the models specified above with the Markov-based trace analysis (MTA) model presented in reference [81], and the block error model suggested in reference [52] for WCDMA simulations (in the following, the latter is referred to as the S-state model). Note that in this comparison, the models are used to reproduce directly the characteristics of measured IP packet error traces, and not DVB-H TS packet error traces as in the previous Subsection.

The considered models are evaluated by applying them in video streaming simulations, where it is assumed that the bit rate of the video stream is 350 kbps, and the video is transmitted in individual frames, updated 25 times per second. An individual image is considered faulty, if more than two IP packets out of four contain errors. Furthermore, the reception quality is observed in intervals of one second, and a second is labeled erroneous if at least one of the 25 received images is faulty. The term erroneous seconds ratio (ESR) is used for the fraction of erroneous seconds in the simulated transmission time. This simplified approach for analyzing video quality was also used in reference [17].

Figure 4.11 shows the ESR simulated using measured IP packet error traces, the mean-based two-state HMM (denoted 2-SMM (mean) in the Figure), the variance-based two-state HMM (2-SMM (var)), the four-state HMM (4-SMM), the MTA model, and the S-state model (S-SMM). The total simulated video duration is 10 minutes. The results indicate that the

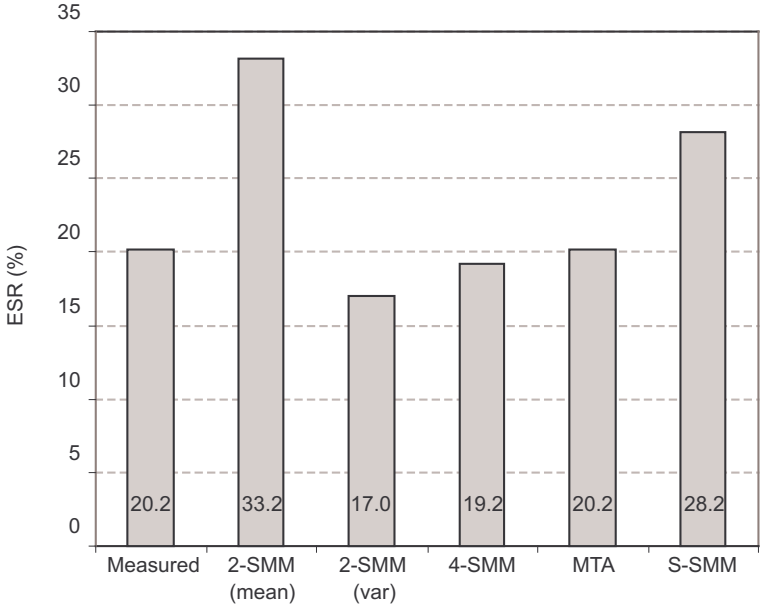

Figure 4.11: Simulated erroneous seconds ratio in a 10 minute video stream as given in [91].

four-state ARMP produces accurate results in this application. Although the MTA model produces the best results compared to the measurement, it should be noted that compared to the four-state ARMP, determining the MTA model parameters requires considerably more complicated analysis of the error traces to be modeled. Furthermore, the MTA model yields poorly to model parameterization as suggested in the following.

4.5 Model Parameterization and Modeling Realistic Field Conditions

The model parameter estimation described in Section 4.2 was based on the assumption that the observed run length distributions L_C and L_E are stationary. In Section 4.3, measurement lengths necessary for proceeding from this assumption were evaluated in the case of laboratory measurements with a set carrier-to-noise ratio and Doppler frequency per measurement. However, there is generally no basis for such an assumption of stationarity in the case of field measurements, since naturally the CNR and Doppler frequency are dependent on the potentially arbitrary movement of the receiver. Therefore the direct parameter estimation suggested in Section 4.2 is not generally justified. However, by considering the field measurement conditions to be piecewise stationary when divided into short time intervals, useful results

can be obtained. In the following, a parameterized error model is applied, where the finite-state model parameters are determined as functions of the CNR and Doppler frequency by utilizing an approximation of relevant packet error statistics.

4.5.1 Approximating Relevant Statistics

In Section 4.2, the HMM parameters were determined using sample statistics of the observed error process $\{Q_n\}$. For simulation purposes, it would be more useful to construct models using underlying physical channel variables such as the average CNR and maximum Doppler frequency. Since in this case the error model is implemented at a relatively high protocol layer, analytical estimation of the effects of the aforementioned variables on the statistics of $\{Q_n\}$ is a nontrivial matter as considered in Chapter 3. In the following, function approximation is used to find simple relationships between the physical channel variables and the statistics of the error process. It should be noted that this parameterization is dependent on the transmission parameters of the broadcast network to be simulated, and should be repeated for different combinations of transmission parameters. This is not a major hindrance to the application of the model, since although the number of possible transmission parameter combinations for DVB-H is quite large, the set of typically used parameter combinations is much smaller. Also, for a given network the transmission parameters may be considered fixed. It is then a relatively easy task to perform the following parameterization for the given transmission setup.

Let $M = \{\overline{L}_C, \overline{L}_E, S^2_{L_C}, S^2_{L_E}\}$ be the set of sample statistics used in evaluating the HMM parameters as described in Section 4.2. It was found that good results are obtained by approximating these statistics in the following manner: laboratory measurements for a suitable range of carrier-to-noise ratios and Doppler frequencies are obtained, and the natural logarithm of each of the parameters m_{ρ,f_D} in M_{ρ,f_D} are calculated - here subscripts ρ and f_D are used to denote the dependence of the statistics on the CNR and Doppler frequency, respectively. Least squared error (LSE) planar fitting is then applied to find the coefficient vector $\overline{C}^*_m = (c_{1_m}, c_{2_m}, c_{3_m})^T$ to minimize $E\left[|\left(c_{1_m}\rho + c_{2_m}f_D + c_{3_m}\right) - \ln(m_{\rho,f_D})|^2\right]$.

For convenience, a solution is summarized: let $\overline{\rho} = (\rho_1, ..., \rho_n)^T$, $\overline{f_D} = (f_{D1}, ..., f_{Dn})^T$, and $\overline{m}_l = (\ln m_1, ..., \ln m_n)^T$, respectively, be vectors composed of the carrier-to-noise ratios, Doppler frequencies and natural logarithms of error statistics of n different laboratory measurements. Now the objective is to find $\overline{C}^*_m$ from the condition

$$|| \left(\overline{1} \mid \overline{f_D} \mid \overline{\rho}\right) \overline{C}_m - \overline{m}_l||^2 = \min_{\overline{C}_m},$$

Table 4.1: LSE coefficients for 16-QAM, convolutional code rate 1/2.

	$\overline{L}_E$	$\overline{L}_C$	$S^2_{L_E}$	$S^2_{L_C}$
c_{1_m}	−0.3273	0.6047	−1.205	1.115
c_{2_m}	0.3788E-3	−29.40E-3	0.9797E-3	−94.99E-3
c_{3_m}	7.653	−2.646	24.08	−1.502

where $\overline{1} = (1 \ ... \ 1)^T$ is an n by 1 vector of ones. Let

$$A \hat{=} \left(\overline{1} \mid \overline{f_D} \mid \overline{\rho}\right).$$

The LSE coefficients are obtained as

$$\overline{C}^*_m = \left(A^T A\right)^{-1} A^T \overline{m}_l.$$

This yields an approximation of the statistics as follows: let

$$\tilde{M} = \{\tilde{\overline{L}_C}, \tilde{\overline{L}_E}, \tilde{S}^2_{L_C}, \tilde{S}^2_{L_E}\}$$

be the set of approximations given ρ and f_D; $\tilde{m} \in \tilde{M}$ is now obtained from

$$\tilde{m} = \exp(c_{1_m}\rho + c_{2_m} f_D + c_{3_m}). \tag{4.17}$$

Table 4.1 contains the LSE approximation coefficients for the statistics of the TS packet error process for DVB-H with 16-QAM modulation mode and physical layer convolutional code rate 1/2. Figure 4.12 shows an example of this approximation for $P(q_E)$ as a function of ρ and f_D. The given parameters can be thought to represent a difficult, or even worst-case, reception scenario, since the receiver used to obtain the given parameters is an early prototype. It is notable that once this parameterization is performed for a given channel and transmission scenario, no additional packet error measurements are required in applying the model as described in the following.

4.5.2 Error Trace Generation

Let N_S be the total number of samples obtained of the RSSI and vehicle speed, and N_{TS} the data-rate dependent number of received TS packets per sampling interval. Error traces are generated using a selected model structure by repeating the following steps for each of the N_S sampling intervals:

I Calculate the values of ρ and f_D corresponding to the measured RSSI and vehicle speed as described above.

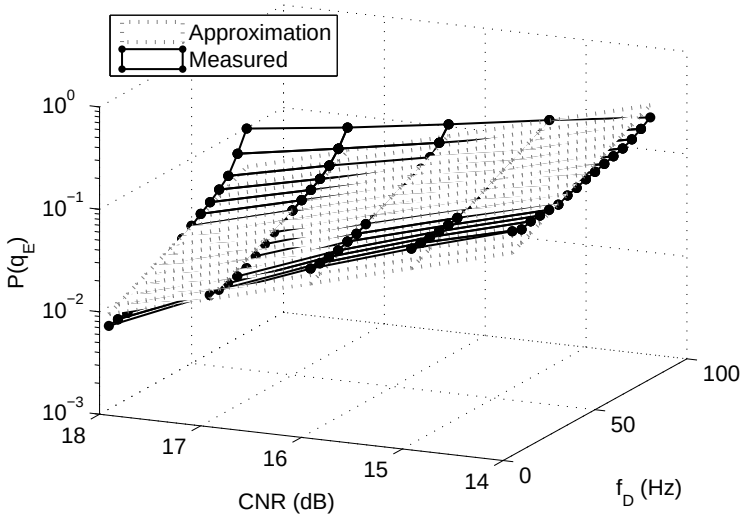

Figure 4.12: LSE approximation of $P(q_E)$ as a function of the CNR and Doppler frequency.

II Using (4.17), determine the values of the packet error statistics needed to solve the finite-state model parameters.

III Calculate the model parameters, for example for a four-state model using $\{\tilde{\overline{L}}_C, \tilde{\overline{L}}_E, \tilde{S}^2_{L_C}, \tilde{S}^2_{L_E}\}$ and equations (4.14) and (4.15). Use the probabilities given in (4.2) as the initial state probabilities and generate N_{TS} output symbols. Concatenate thus obtained subtrace with previously generated subtraces.

4.6 Possible Applications

The class of models described in Section 4.1 can be considered an extension of the simplified Fritchman model, and is readily applicable in the numerous scenarios, outlined in Chapter 3, where the Fritchman model has been used. Additionally, the considered models facilitate approximating both correct and error run length distributions more accurately than a simplified Fritchman model. Therefore they are suitable also for modeling scenarios with large dynamic variation in the received signal quality, characterized by long time intervals both with very high and very low error probabilities. One relevant application is thus simulating mobile wireless systems, where the signal quality can be expected to vary considerably more than for example in traditional wireless broadcast systems with fixed receiver antennas.

The parameterization specified in Section 4.5 enables extending the considered models beyond replicating only the statistical properties of specific measurements. This offers a compact method of describing the performance of given system/channel scenarios, as the error behavior over a range of CNR and Doppler frequency values can be simulated based on a small set of LSE coefficients as given for example in Table 4.1. To some extent, this approach can also be used to interpolate and extrapolate error traces corresponding to reception conditions not covered by a given set of measurements.

In some scenarios - such as mobile broadcasting - it is useful to be able to simulate system performance for very large groups of users moving simultaneously within a large transmission area. Using low-level simulation models such as those presented in Chapters 2 and 3 this is typically not feasible, since for practical purposes the simulations for each independent receiver should be realizable considerably faster than real-time transmission. In the next Chapter, a system simulation structure for DVB-H that enables efficient simulation of large numbers of mobile users within a broadcast network is considered as a case study. The simulator is implemented using the above described parameterized four-state model for approximating the performance of the DVB-H physical layer. Simulation results are then compared with a set of field measurements obtained in currently operating DVB-H test networks.

Chapter 5

Case Study: Dynamic Simulation of Mobile Broadcast Networks

Traditional network planning for broadcast networks is based on a static approach that targets to guarantee a certain area coverage level, or percentage of covered service area locations with a given maximum probability of error at any time. However, mobile broadcasting networks, such as a DVB-H network, require dynamic analysis over time, since the level of quality of service (QoS) perceived by the users cannot be studied from average performance measures within the service area. An example of a performance measure typically applied for DVB-H is the frame error rate commonly used in DVB-H network planning [92]. Such measures may not be generally sufficient for analyzing QoS, as it depends on the time-variant behavior of transmission errors, which are determined by the mobility characteristics of specific users.

In this Chapter the need for dynamic system-level simulations for DVB-H is considered, specifically to evaluate the overall system performance perceived by mobile users dynamically over time. Such simulations can be used as a complement of traditional radio coverage planning tools for analyzing quality of service and radio resource management aspects of a DVB-H network. A general simulation structure is described along with the main models required, and, using vehicular urban field measurements, a specific implementation that enables these analyzes is evaluated. The work presented in this Chapter was originally published in references [18, 19], both with the author of this thesis as the main author. Furthermore, reference [20] provides an example of the type of studies where the proposed simulator can be utilized.

5.1 Measurement-Based Evaluation of Service Quality for DVB-H Systems

In DVB-H systems, multimedia content can be delivered either as a streaming service or as a file delivery service to the end user [93]. For streaming services, a continuous data flow of audio, video and subtitling is transmitted and directly consumed by the users. The most representative example of such services is mobile television. As presented in Appendix B, DVB-H terminals play the information received in the last data burst until the next burst is received, in such a way that users do not notice the discontinuous transmission. If one burst is lost, the media stream is interrupted until the next burst is received. For file delivery services, a finite amount of data is delivered and stored into the terminals as a file. Some typical examples of such content are video clips, digital newspapers, and software downloads. In this case, DVB-H terminals store correctly received information in each burst associated to the file until the complete file is available at the receiver, and accessible by applications.

For streaming services occasional errors in the received data may be tolerated if the quality of the audio and video is sufficient for providing a satisfactory user experience. Typically, a 5% frame error rate is considered as the degradation point for streaming services when using MPE-FEC [90]. This criterion is also known as MFER 5% (MPE-FEC frame error rate). Another performance indicator that describes the service quality is the erroneous seconds ratio (ESR [90]), which is defined as the percentage of erroneous seconds during the streaming service reproduction time. Compared to the frame error rate, the ESR takes into account that it is possible to receive data frames partially, however both MFER and ESR only account for the overall transmission errors experienced by the users. One indicator that takes into account the time distribution of the errors is the ESR5(20) ratio, which represents the percentage of time intervals of 20 seconds with at most 1 erroneous second, that is, 5 % erroneous seconds [90].

File delivery services typically require completely error-free reception of the source data, as even a single bit error can corrupt an entire file, making it in practice useless for the receiver. The main QoS indicator is thus whether the user receives a given file correctly or not. In order to increase the robustness of the DVB-H file delivery, an additional forward error correction mechanism at the application layer (AL-FEC) using Raptor coding [94] has been adopted [93].

Field measurements are obviously the most realistic way of measuring the actual performance of any wireless communication system. For DVB-H, by recording TS packet error traces, it is possible to approximate the quality of service experienced by receivers across the measurement trajectories for

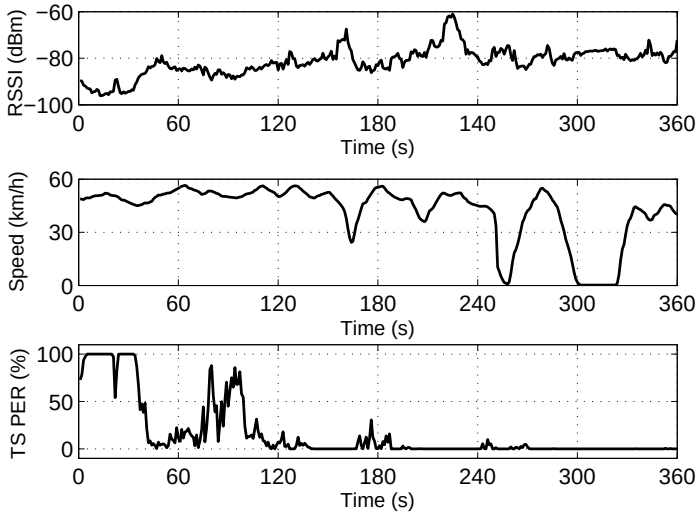

Figure 5.1: Example data of vehicular urban DVB-H field measurement.

various services (streaming or file delivery) by emulating the upper layers. Moreover, it is possible to investigate the effect of different DVB-H transmission configurations at the link and application layers, such as the burst size and the MPE-FEC and AL-FEC configuration parameters. Note that the measured error traces depend on the physical layer transmission mode employed, and thus the physical layer parameters are fixed for such QoS estimation. Figure 5.1 shows an example of data recorded during a DVB-H field measurement campaign performed in the DVB-T/H test-bed of the University of Turku, Finland, using a 16-QAM modulation mode, 1/4 OFDM guard interval length, 8K FFT length, and 1/2 physical layer convolutional code rate. The shown data consists of received signal strength indicator (RSSI), receiver speed, and time-variant TS packet error rate information.

Figure 5.2 shows the cumulative number of erroneous seconds, corresponding to the measurement illustrated in Figure 5.1, as a function of the service time for a six-minute streaming service at 256 kb/s for different MPE-FEC coding rates. To obtain the results, the conventional MPE-FEC erasure decoding mode and 512 rows per MPE-FEC frame have been considered. A constant IP packet size equal to 512 bytes was assumed, and also that the media content in each IP packet can be retrieved independently of previous or subsequent IP packets. In the Figure, the time evolution of errors experienced by the users, as well as the actual improvement perceived by the user when varying the MPE-FEC coding rate can be seen.

The main problem with field measurement campaigns is that their re-

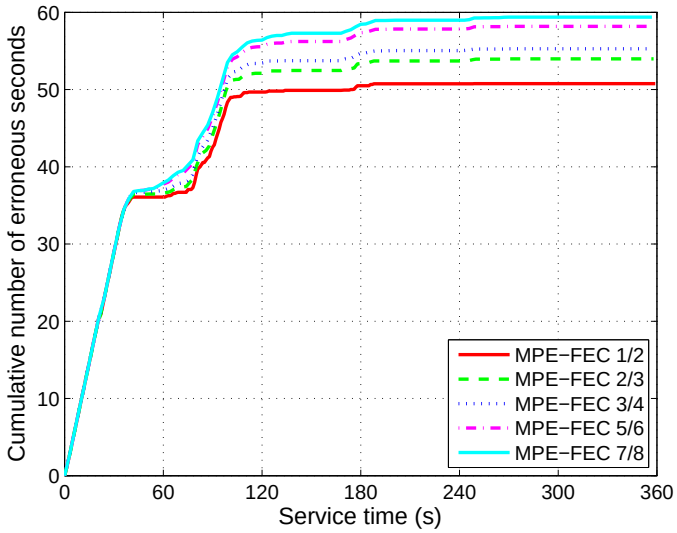

Figure 5.2: Time evolution of the errors for a 256 kb/s streaming service across the measured trajectory shown in Figure 5.1.

source expenditure is often cost prohibitive. Moreover, results obtained apply only for specific measured receiver trajectories. To extract conclusions about overall system performance experienced by users in a service area, a large number of measurements is needed. If, for example, the objective is to consider the percentage of satisfied users, assuming a given QoS criteria, thousands of independent receiver trajectories would generally be needed to obtain statistically consistent average results. If it is taken into account that measurements are only useful for the specific DVB-H physical layer transmission mode and network configuration setting employed, the need of performing dynamic system level simulations becomes apparent.

In the particular case of DVB-H, with a dynamic system-level simulator it would be possible to evaluate the overall QoS perceived by users of a given service as a function of the DVB-H transmission configuration. For example, simulations could be performed to estimate the time evolution of errors perceived by mobile users of a streaming service, or to determine the users that successfully receive a file, and the amount of repair information needed by each user not able to decode the file. This can be achieved by accurately modeling the time-variant error behavior of the receiver physical layer, and emulating the upper protocol layers based on this error information as in the example of the previous subsection. Not only should the simulation provide accurate results, but the results should also be obtained in a computationally efficient manner to enable simulation of large groups of users.

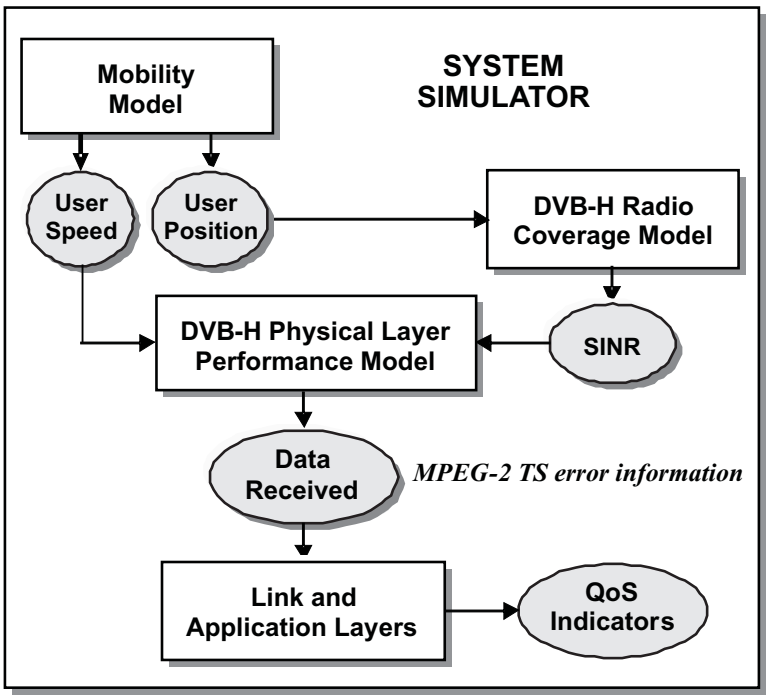

Figure 5.3: DVB-H system level simulator architecture.

5.2 Overview of a Dynamic DVB-H System Level Simulator

Four major blocks (modules) can be identified as necessary in a dynamic DVB-H system level simulator: a mobility module, a DVB-H radio coverage module, a DVB-H physical layer performance model, and a module to emulate the link and application layers (see Figure 5.3). The mobility model approximates the mobility patterns of users across the service area, and computes the speed of the users when receiving a burst. The DVB-H radio coverage module computes the average signal-to-interference plus noise ratio (SINR) during the reception of a burst for each user. For this purpose, a DVB-H coverage map of the service area can be pre-computed in order to speed up the simulation process. The DVB-H physical layer performance model computes which MPEG-2 TS packets are correctly received per burst for each user, based on the information of the time-variant reception conditions obtained from the mobility and radio coverage models. Finally, the packet error information is used in the link and application layers to compute the QoS indicators for the service under study.

The considered approach can be described as a discrete-event simulator, where the only events are the reception of data bursts by the users. For

each data burst, the receiver position and speed is updated in the mobility model, the signal strength corresponding to the updated location is estimated in the radio coverage model, and error content in the data burst is subsequently simulated using the physical layer performance model. The average received signal strength and receiver speed are assumed to be constant for the duration of each received burst.

5.2.1 Mobility Model

Mobility models are key elements in dynamic simulators, since the simulation results may vary significantly for different mobility patterns (receiver trajectories and velocities). For this reason it is important that the mobility model is based on realistic traffic patterns for the scenario under study. Note that different models may be needed to account for different usage scenarios, for example for pedestrian (indoor and outdoor) and vehicular (urban and motorway) cases. For an example of a mobility model for vehicular users extracted from realistic urban traffic conditions, see reference [95].

The model described in [95] provides different distribution functions with limited numbers of parameters to be derived for a particular city. The relative direction changes at crossroads are expressed by a mixture of four normal distributions with means selected 90° apart, and weights selected according to the probability of turning left or right, turning around, or continuing straight. Each component distribution is assigned the same standard deviation, whose value is dependent on the considered road network characteristics. The distance between crossing streets is assumed to be a Rayleigh distributed random variable. A given user's speed is modeled according to a Rayleigh or Rice distribution to distinguish between urban streets and major roads, respectively. The speed parameters are the mean speeds of city and major roads, speed deviation, and the percentage of cars on major roads. Typically users are distributed uniformly within a given area, unless specific information about population density is available.

5.2.2 DVB-H Radio Coverage Model

The DVB-H radio coverage model is also a critical element in the simulator to determine the received signal strength corresponding to user locations given by the mobility model. It should be pointed out that typically coverage estimation only provides the average received signal strength with a given spatial resolution. As the actual field strength can be considered a random variable, typically characterized by a lognormal distribution, it is necessary to account for the variation of the medium-scale fading, considered in more detail in Chapter 2, within each grid element of a coverage map by adding an instantaneous component to the predicted mean values. For relatively

low-resolution grids (rectangular element dimension 500 x 500 m), a typical value for the standard deviation of this lognormal component with DVB-T/H in the UHF band is 5.5 dB, however for higher resolutions a lower value may be more realistic [90]. Furthermore, the correlation properties of the instantaneous received signal strength component must be determined according to the modeled environment.

When considering a real, site-specific scenario, the accuracy of the radio propagation models, which give a prediction of the mean received power at each location in the service area from each transmission site in the network, depends on the available cartography and its resolution. As considered in Chapter 2, relevant geographical data can be classified in terrain height (topography), terrain morphology (land usage or clutter class), and building heights and shapes. In order to further increase the accuracy of the results, radio propagation models can be calibrated based on field measurement campaigns. The calibration process aims to provide a zero mean and a minimum standard deviation of the error between the prediction and the measurements.

5.2.3 DVB-H Physical Layer Performance Model

The DVB-H physical layer performance model must predict which MPEG-2 TS packets or MPE sections are correctly received for each DVB-H transmission burst. In the considered simulation structure, the main input parameters for the physical layer performance model are:

- Physical layer transmission mode: FFT size, OFDM prefix length, modulation mode and convolutional code rate
- Channel model
- Average Carrier-to-Noise Ratio
- Terminal speed

Of these, the transmission mode and the channel model can be considered fixed for any given simulation scenario. The transmission mode is mainly determined by the desired system capacity, although other parameters such as transmission robustness, maximum supported terminal velocity, and maximum distance between transmitters may also be taken into account in the system design process. Regarding DVB-H channel models, the COST 207 typical urban 6-tap model has been found to be representative for mobile reception for Doppler frequencies above 10 Hz [90], and it is used to construct the packet error model applied in the following as described in Chapter 4. It is relevant to note that the considered simulation structure also enables assigning different communication channel models for different

geographical segments of the network area to be simulated - this could be relevant for example in taking into account the variation of building density and different line-of-sight conditions within the reception area.

In the following, the parameterized four-state TS packet error model described in Chapter 4 is utilized as a physical layer performance model within the DVB-H system simulator. It should be noted that to compare the accuracy of the model with field measurements, measured signal strength values must be converted to corresponding values of ρ in the TU6 model used in the laboratory measurements as described in Chapter 4. In the following implementation this is done by matching the average TS packet error rates as functions of the received signal strength and ρ for a set of field and laboratory measurements, respectively. This conversion can be done also without explicit information of measured TS packet error rates. Using noise figures given by the receiver manufacturer and an approximation for the background noise in the measurement environment produced a conversion factor between the received signal strength and ρ that differed from the above mentioned matching by approximately 1.5 dB.

Furthermore, the values for f_D required in determining the error model parameters are obtained as the maximum Doppler frequency given the measured vehicle speed and carrier frequency of the DVB-H broadcast. Since the TU6 channel model used for the parameterization is a non line-of-sight model as defined in Chapter 2, it is not necessary to consider the direction of the receiver velocity for determining the model parameters.

5.3 Validation Results

In this Section, the suitability of the considered physical layer performance model is evaluated using vehicular urban DVB-H field measurements. This is done by replacing the mobility and radio coverage models of the system simulator with measured vehicle speed and RSSI information, and comparing the simulation results thus obtained with field measurements. Furthermore, field measurement results are compared with system simulations performed using a precalculated DVB-H coverage map as the radio coverage model. This validation approach differs from the complete system simulator described in the previous Section only in that instead of the mobility model, measured GPS data are used in the simulations.

5.3.1 Methodology

The majority of field measurements considered in the following were performed in the DVB-H SFN test-bed of the University of Turku (Finland). The network has two transmitters operating at 610 MHz (channel 38). Field measurements were performed at various locations and transitions around

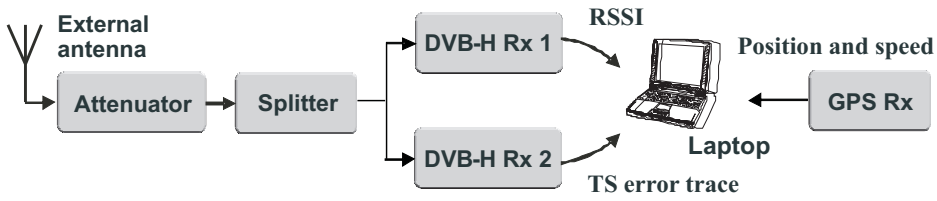

Figure 5.4: DVB-H field measurement system.

the city of Turku. The total measurement time was 2 hours (corresponding to approximately $49 \cdot 10^6$ MPEG-2 TS packets), divided into 20 individual measurements of length 6 minutes each. The measurement setup is illustrated in the block diagram of Fig. 5.4. DVB-H transmissions were received using an external antenna placed inside a vehicle with speed ranging approximately from 0 to 60 km/h. The signal was then transferred through an attenuator and a splitter into two DVB-H receivers. Received signal strength indicator data (with 1 dB resolution) was obtained from one receiver, and a TS packet error indicator trace from the other receiver. The RSSI and error information were then synchronized, combined with GPS data (position and speed), and stored on a laptop computer. An example of the obtained vehicular urban measurement data was presented in Figure 5.1.

In the following Subsection, the validity of the proposed physical layer model is verified by replacing the mobility and radio coverage models with measured vehicle speed and RSSI values, respectively, and comparing the simulated TS error traces to those obtained from the measurements. It should be pointed out that for small-size networks like the one considered in this work, self-interferences are negligible, and thus the CNR can be directly approximated from the received signal strength.

5.3.2 Simulations Using RSSI and Speed Measurements

Figure 5.5 shows an initial example of TS packet error rates as functions of time (averaged over 1 s intervals), obtained from a field measurement performed in the DVB-H network in the Hague, Netherlands (operating with a 16-QAM modulation mode, 1/4 OFDM guard interval length, 8K FFT length, and 1/2 physical layer convolutional code rate), and from an error trace generated using the parameterized four-state hidden Markov model based on measured RSSI and vehicle speed data. It can be seen that the generated error trace follows the fluctuations in instantaneous packet error rate of the measurement very well. The total average TS packet error rate in the measurement was 23.4%, and 23.7% in the generated error trace. Furthermore, the simulated average IP packet error rates obtained with the field measurement and with the parameterized four-state model were 21.0% and 20.5%, respectively, and the corresponding simulated average MPE-FEC

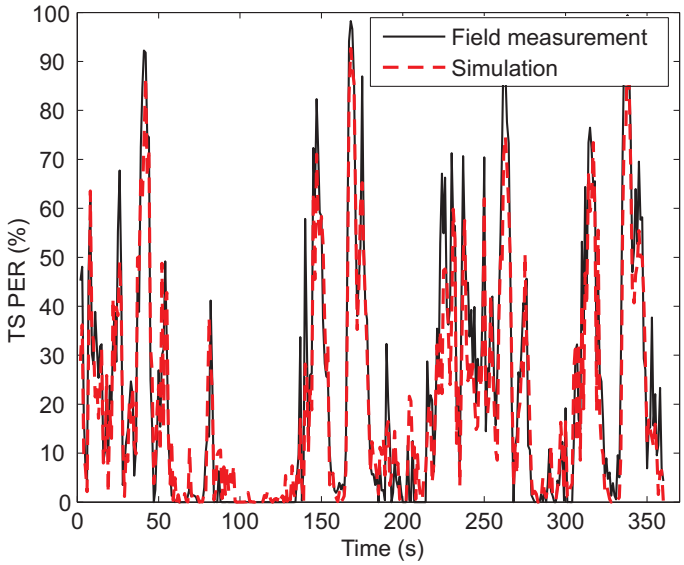

Figure 5.5: Comparison of measured and modeled DVB-H TS packet error rates averaged over 1 s intervals. Simulation performed using time-dependent RSSI and vehicle speed values measured in the Hague, Netherlands.

frame error rates were 28.1% and 29.6%.

To verify that the model parameterization and simulation performance results are not valid only for this specific network and set of measurements, similar field measurements were performed in the DVB-H test network in Turku, Finland, as described in the previous Subsection. Figure 5.6 shows an example of measured and simulated TS packet error rates (PER) over time corresponding to the measured trace shown in Figure 5.1 (error rates are averaged over 1 s intervals). It can be seen that again the time-variant packet error rate of the simulated error trace very closely follows the measurement. This is also true for the average packet error rate for each of the individual six-minute measurements, as can be seen in Figure 5.9.

The leftmost columns in Table 5.1 show the total average error statistics for the 2 hours of measurements in terms of TS PER, MPE-FEC section error rate (MPE SER), and IP PER (constant IP packet size 512 bytes), MFER, ESR, and ESR5(20) for a 256 kb/s streaming service (number of rows per frame 512 and MPE-FEC code rate 1/2), and the corresponding simulation results obtained as described above. From these validation results it can be concluded that the overall accuracy of the considered DVB-H physical layer performance model is relatively good with measured mobility and coverage information. Possibilities for improving the simulation results can be identified for example in modifying the parameterization of the physi-

Table 5.1: Average error rates (in %, over complete set of measurements)

Error criterion	Measured	Simulated with measured RSSI	Simulated with predicted RSSI
TS PER	3.9	3.7	3.9
MPE SER	4.2	3.8	4.0
MFER	4.9	4.6	4.5
IP PER	3.7	3.3	3.7
ESR	5.1	4.5	4.5
ESR5(20)	11.9	11.5	9.0

cal layer performance model. In these simulations, the parameterization was based on the TU6 channel model, which is by definition not the most suitable solution for example in line-of-sight conditions.

In the following Subsection, the accuracy of the proposed system simulator is evaluated by using a precalculated coverage map as the radio propagation model, and by again replacing the mobility model with measured GPS information. Simulation results are again compared to the above described set of field measurements.

5.3.3 RSSI Estimation from Coverage Prediction

To consider a specific use case with coverage prediction, the coverage map shown in Figure 5.7 is applied for determining the predicted signal strength as a function of receiver trajectories measured using recorded GPS data. An example of receiver location information corresponding to a set of field measurements performed in the test network, plotted over the applied coverage map, is also shown in Figure 5.7. The coverage estimation was computed by the Finnish broadcasting service provider Digita, as described within the European Celtic Wing TV project [96], using the CRC (Canadian Research Corporation) propagation model with terrain height, building and clutter information (pixel size 110 m). For the simulations considered in this Thesis, the coverage map was calibrated using measurements to correspond to the received signal strength for in-vehicle reception. Figure 5.8 shows the measured and predicted signal strength values as functions of time for the route shown in Figure 5.7. The mean error for the obtained coverage prediction is -0.5 dB, and the standard deviation is 7.8 dB. It should be noted that for these simulations, only the average RSSI provided by the coverage

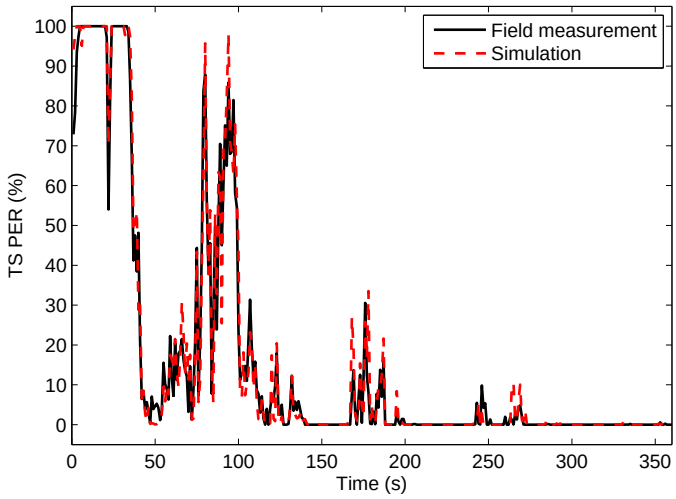

Figure 5.6: Comparison of measured and modeled DVB-H TS packet error rates averaged over 1 s intervals. Simulation performed using time-dependent RSSI and vehicle speed values measured in Turku, Finland.

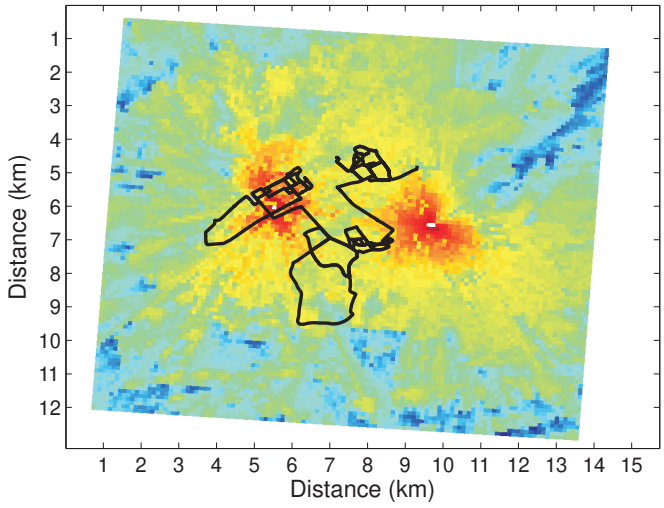

Figure 5.7: Measured GPS data over coverage prediction map of the DVB-H test network in Turku, Finland.

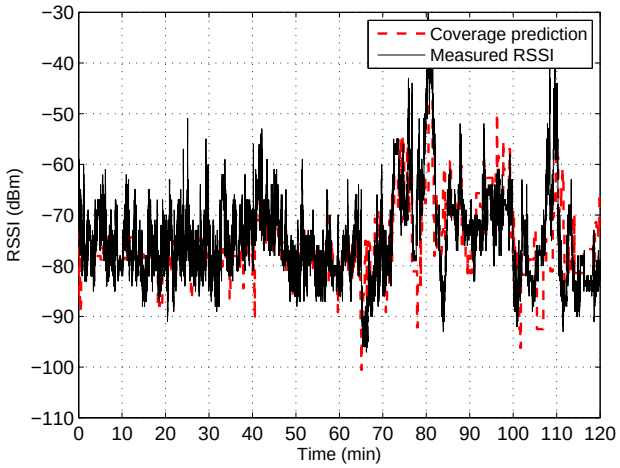

Figure 5.8: Measured RSSI data compared to coverage prediction.

map is used. Introducing an instantaneous RSSI component as discussed in subsection 5.2.2 is left for future consideration.

Simulated error rates obtained using measured and predicted RSSI values are compared in Table 5.1 to field measurement results. It can be seen that in modeling this set of measurements, also the coverage prediction-based simulations produce accurate average results. In this case study, error in the coverage prediction contributes positively to the accuracy of the average simulation results. Results for simulating short or localized receiver routes may be more inaccurate, however. This is illustrated in Figure 5.9, where simulated and measured TS packet error rates for each of the 20 six-minute measurements are shown. Still, the accurate average error rates obtained in the case study above are a very positive result, and as such confirm the usefulness of the considered simulation models. It is also relevant to note that of the simulated error rates given in Table 5.1, the ESR5(20) best represents the true order of the considered models in terms of simulation accuracy.

5.3.4 System Simulation Example

Finally, to verify that the proposed system simulator is applicable for the specified purpose of simulating large groups of users, the full simulation structure was implemented by incorporating the mobility model outlined in Subsection 5.2.1. Vehicular (portable in-car) reception was considered, using the DVB-H coverage map of the SFN test-bed of the University of Turku shown in Figure 5.7. Figure 5.10 shows the vehicle speed probability distribution specified for the mobility model. 10 000 users were randomly placed

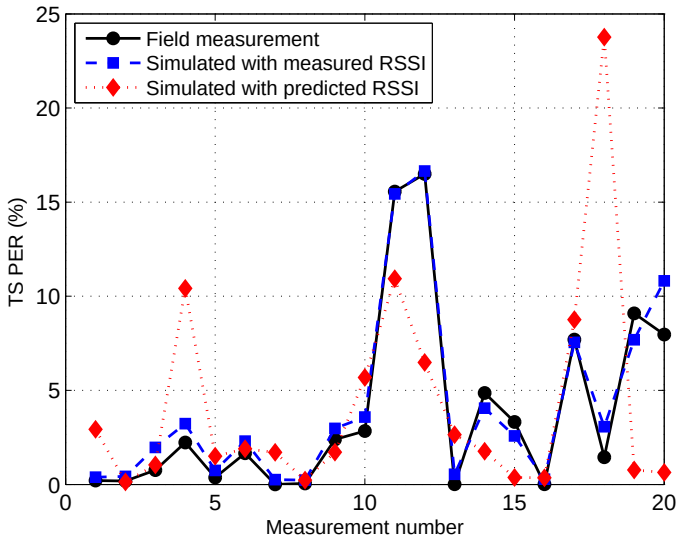

Figure 5.9: Simulated average TS packet error rates compared to measured values for a sequence of six-minute measurements.

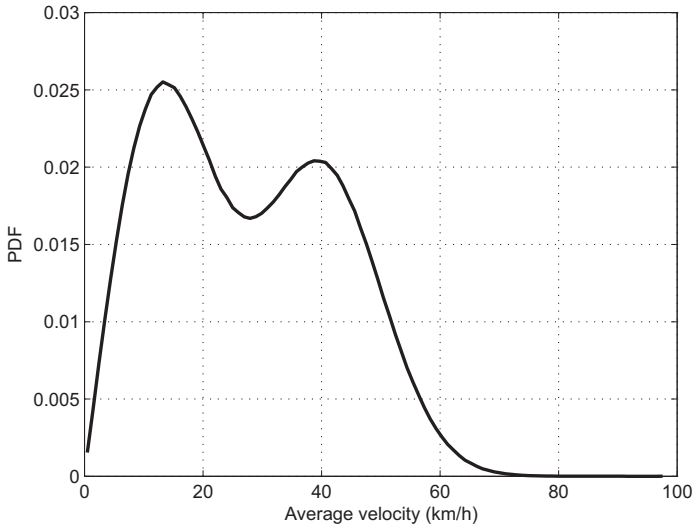

Figure 5.10: Probability density function for the vehicle speed used in the mobility model.

within the coverage area, and a 10 minute streaming service was simulated at a data rate of 256 kb/s. The generated TS packet error information of each of the 10 000 users were then used to analyze various global properties of the broadcast network.

Figures 5.11 and 5.12 show simple examples of the information available from the simulations. Figure 5.11 demonstrates the cumulative distribution function (CDF) of the erroneous seconds ratios experienced by the 10 000 users for various MPE-FEC code rates. From this example it can be seen that the MPE-FEC code rate is not significant in terms of the distribution of the ESR. However, the distribution of the average number of correctly received MPE sections in MPE-FEC frames containing uncorrectable errors is affected by the MPE-FEC code rate, as shown in Figure 5.12. It should be kept in mind that the number of data sections in each frame is dependent on the MPR-FEC code rate, as specified in Appendix B. Still, the given example serves to demonstrate that the link layer code rate affects the potential gain of utilizing also content of erroneous MPE-FEC frames at upper protocol layers.

The total runtime required to produce the 10 000 error traces used in the examples described above was $3.9 \cdot 10^4$ seconds (or approximately 11 hours) using a 2.4 GHz tabletop PC with 2 GB of RAM. The time it would require to record the same amount of error information in field measurements using a single receiver is $6.0 \cdot 10^6$ seconds (approximately 1 667 hours), meaning that the time expenditure required for obtaining the simulated data is only 0.65 % of the corresponding field measurement time, which of course excludes all peripheral efforts such as setting up the measurement equipment and transportation between measurement locations.

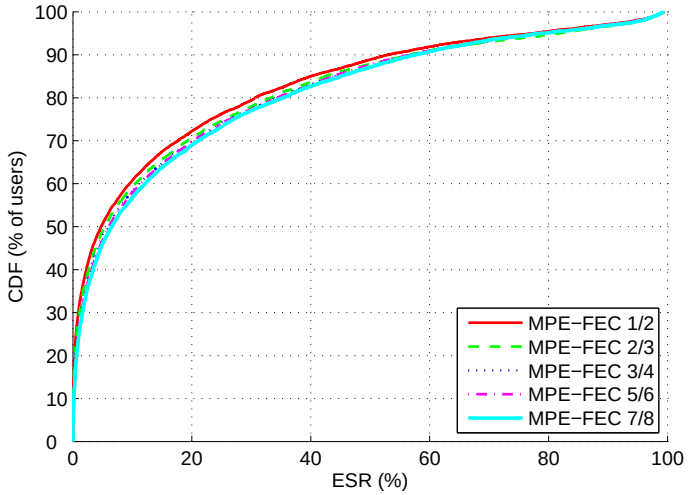

Figure 5.11: CDF of the erroneous seconds ratio for a 10 min streaming service at 256 kb/s. MPE-FEC frame size 512 rows.

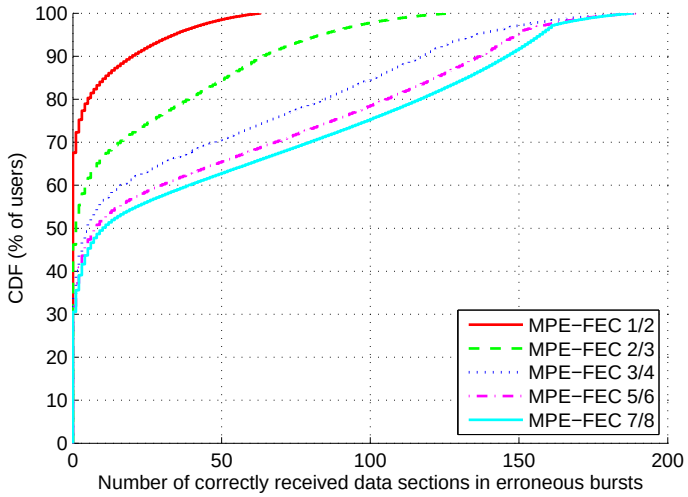

Figure 5.12: CDF of average number of correctly received data sections in erroneous MPE-FEC frames. Frame size 512 rows.

Chapter 6

Conclusions

In this Thesis, it was studied how and to which extent it is feasible to derive, based on physical channel models, finite-state models for simulating mobile wireless communication systems, and how to model specific wireless communication systems at various protocol levels, or levels of abstraction, in a computationally efficient manner. Table 6.1 summarizes in order of presentation the simulation models most relevant for the development of this study. From the given input and output data types of the different models, it is evident how the considered models extend from the physical, relatively system-independent Rayleigh and WSSUS channels presented in Chapter 2, to the modulation-specific finite-state Markov channel and frequency-selective finite-state model considered in Chapter 3, and finally to the packet error models studied in Chapters 4 and 5. These packet error models were applied to model specific error processes of a DVB-H system, and while the models as such are not designed for any specific communication system, their application requires the derivation of numerical model parameters that correspond to a specific system and transmission scenario.

Figure 6.1 further illustrates the conceptual structure of the Thesis, with dependencies between considered subjects outlined. By deriving the frequency-selective finite-state model in Chapter 3 based on properties of physical WSSUS channel models and the FSMC model for Rayleigh fading, it was found that it is feasible to derive an accurate and efficient finite-state simulation model for a mobile wireless OFDM system directly from relevant system and channel parameters. This derivation, which is an original contribution of this work, was partly facilitated by the study performed in Chapter 2, which indicated that in the considered OFDM simulations, the delay spread S_D and maximum Doppler frequency f_D are practically sufficient to determine the effect of the channel. That is, the exact discrete power delay profile of a WSSUS channel model was found to have a relatively minor effect on the average error rate of the considered system, given

Table 6.1: Main simulation models considered in the Thesis with the corresponding primary user input data, and output data types.

Simulation model	Input data	Output data
Rayleigh	f_D	Fading coefficient
WSSUS	S_D, f_D	Impulse response
FSMC	SNR, f_D	Symbol error trace
Freq. sel. FSM	CNR, S_D/T_s, $f_D T_s$	Symbol error trace
ARMP	Run length statistics	Packet error trace
Parameterized ARMP	RSSI, Speed	Packet error trace

fixed values for S_D, f_D, and the number of discrete delay components in the channel model. To the author's knowledge, this study is also a novel, though relatively minor, contribution of this Thesis.

Further abstraction was studied initially by considering the principle and limitations of threshold models for block error processes in Chapter 3. Several previously applied generic statistical models applicable in simulating block or packet error processes were outlined in the end of Chapter 3. Aggregated renewal Markov processes, which can be considered as an extension of the widely used simplified Fritchman models, were defined in Chapter 4, and subsequently applied for simulating link and IP-level packet error processes of a DVB-H system. The model parameters were determined based on measured data from a DVB-H system operating through a hardware WSSUS channel simulator. It was found that while using a simple aggregated Markov process with only two states does not generally produce accurate results, selection of the statistical characteristic to be matched using such models has a significant effect on the accuracy of the model. Furthermore, it was found that with the considered application and performance metrics, four-state aggregated Markov processes produced results that can not be significantly improved upon using models classifiable as renewal processes. The consideration of aggregated renewal Markov processes is a major original contribution of this work, which directly builds upon a pre-existing area of research on finite-state error models.

Derivation of model parameters from physical reception conditions was considered using function approximation for relevant error statistics as functions of the carrier-to-noise ratio and maximum Doppler frequency of the received signal. This model parameterization was used in the case study of Chapter 5 to construct a dynamic system simulator corresponding to a specific DVB-H network. Simulation results were found to be accurate

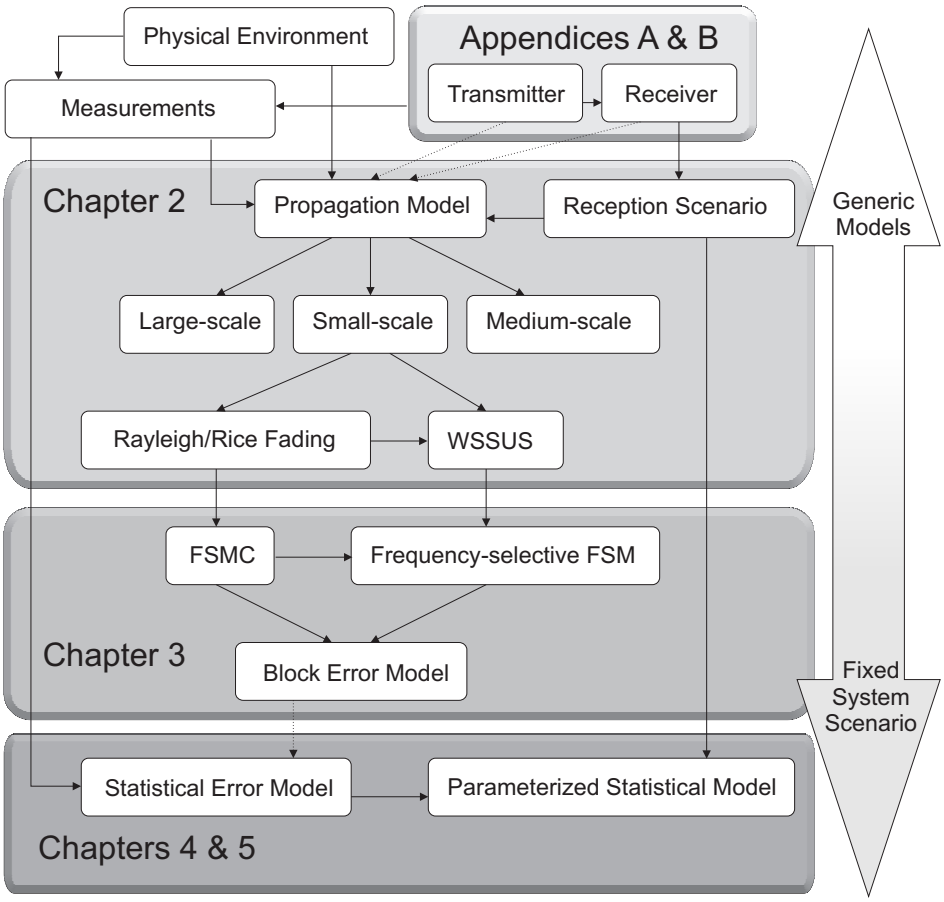

Figure 6.1: Conceptual structure of the Thesis.

compared to corresponding field measurements. Finally, an application example of the dynamic system simulator was given, where 10 000 mobile receivers were simulated within the considered DVB-H network. The study of large-scale dynamic simulation of mobile broadcast networks is also a novel contribution of this work, which builds upon the efficient simulation models considered earlier in the Thesis.

To summarize: in this Thesis, finite-state models were considered for physical and modulation symbol level error processes, and for packet error processes at transport stream and internet packet protocol layers of a specific communication system. All models were derived based on underlying physical channel and system characteristics using direct theoretical analysis, and approximations based on both simulations and measurements. It was found that significant performance gains were achievable with tolerable decrease in accuracy of the results compared to more detailed models. A clear tradeoff was identified in that highly abstracted models lose the possibility of modifying specific system and channel characteristics, which is an important property of simulation models. However, in many cases the possibility for efficient implementation and application of simplified models outweighs the disadvantages.

Topics for future work can be identified within this Thesis. Related to the frequency-selective finite-state models for OFDM systems considered in Chapter 3, a direct subject for further research is to consider incorporating the recently proposed improvements [42, 49] to the FSMC model, which exhibit more accurate autocorrelation properties. The dynamic system simulator considered in the case study of Chapter 5 can be developed further for example by incorporating additional system scenarios and by applying different physical channel characteristics to different regions of the coverage area - a straightforward example would be to determine model parameter sets according to line-of-sight and non-line-of-sight conditions. Furthermore, the considered simulation structure may be useful as a tool for developing and testing subjective quality measures for analysis of mobile multimedia services.

Bibliography

[1] M. C. Jeruchim, P. Balaban, K. S. Shanmugan, *Simulation of Communication Systems, 2nd edition*, Kluwer Academic, New York, 2000.

[2] J. G. Proakis, *Digital Communications, 3rd edition*, McGraw-Hill, 1995.

[3] R. E. Ziemer, R. W. Peterson, *Introduction to Digital Communication*, Prentice Hall, 2001.

[4] S. Haykin, *Communication Systems*, John Wiley & Sons, Ltd., 2001.

[5] T. K. Moon, *Error Correction Coding - Mathematical Methods and Algorithms*, John Wiley & Sons, Ltd., 2005.

[6] Y. Q. Shi, X. M. Zhang, Z.-C. Ni, N. Ansari, "Interleaving for combating bursts of errors," *IEEE Circuits and Systems Magazine*, vol. 4, First Quarter 2004, 29-42.

[7] C. Oestges, B. Clerckx, *MIMO Wireless Communications: From Real-World Propagation to Space-Time Code Design*, Elsevier, 2007.

[8] E. Lutz, D. Cygan, M. Dippold, F. Dolainsky, W. Papke, "The Land Mobile Satellite Communication Channel – Recording, Statistics and Channel Model," *IEEE Trans. Veh. Technol.*, vol. 40, May 1991, 375-386.

[9] J. Poikonen, "Finite-state Models for Simulating the Performance of DVB-H," *Master's thesis*, University of Turku, May 2005.

[10] J. Poikonen, J. Paavola, "Comparison of Finite-State Models for Simulating the DVB-H Link Layer Performance," *Proc. ISWCS '05*, Siena, Italy, 2005.

[11] J. Poikonen, J. Paavola, "Error Models for the Transport Stream Packet Channel in the DVB-H Link Layer," *Proc. ICC 2006*, Istanbul, Turkey, 2006.

[12] J. Poikonen, "Half-normal Run Length Packet Channel Models Applied in DVB-H Simulations," *Proc. ISWCS '06*, Valencia, Spain, 2006.

[13] J. Poikonen, "Geometric Run Length Packet Channel Models Applied in DVB-H Simulations," *Proc. PIMRC 06*, Helsinki, Finland, 2006.

[14] J. Poikonen, "Parameterization of Aggregated Renewal Markov Processes for DVB-H Simulations," *Proc. PIMRC '07*, Athens, Greece, 2007.

[15] J. Poikonen, J. Paavola, V. Ipatov, "Finite-State Models for Simulating the Packet Error Behavior of a Mobile Broadcasting System Operating in a Multi-Path Channel Environment," *Handbook of Mobile Broadcasting*, CRC Press, 2008.

[16] J. Poikonen, J. Paavola, V. Ipatov, "Aggregated Renewal Markov Processes with Applications in Simulating Mobile Broadcast Systems," to appear in *IEEE Trans. Veh. Technol.*, January 2009.

[17] J. Paavola, H. Himmanen, T. Jokela, J. Poikonen, V. Ipatov, "The Performance Analysis of MPE-FEC Decoding Methods at the DVB-H Link Layer for Efficient IP Packet Retrieval," *IEEE Transactions on Broadcasting - Special Issue on Mobile Multimedia Broadcasting*, 2007.

[18] J. Poikonen, "Applications of Parameterized Packet Error Models for Simulating Mobile DVB-H Reception in an Urban Environment," *Proc. ISWCS '07*, Trondheim, Norway, 2007.

[19] J. Poikonen, D. Gómez-Barquero, "Validation of a DVB-H Dynamic System Simulator using Field Measurements," *Proc. IEEE International Symposium on Broadband Multimedia Systems and Broadcasting*, Las Vegas, Nevada, 2008.

[20] D. Gómez-Barquero, J. Poikonen, "Filecasting for Streaming Content Delivery in IP Datacast over DVB-H Systems," *Proc. IEEE International Symposium on Broadband Multimedia Systems and Broadcasting*, Las Vegas, Nevada, 2008.

[21] S. R. Saunders, A. Aragón-Zavala, *Antennas and Propagation for Wireless Communication Systems, 2nd edition,* John Wiley & Sons, Ltd., Chichester, 2007.

[22] N. Blaunstein, J. B. Andersen, *Multipath Phenomena in Cellular Networks,* Artech House, Boston, 2002.

[23] B. Sklar, "Rayleigh Fading Channels in Mobile Digital Communication Systems Part I: Characterization," *IEEE Communications Magazine*, September 1997, 136-146.

[24] Y. Okumura, E. Ohmori, K. Fukuda, "Field Strength and its Variability in VHF and UHF Land Mobile Radio Service," *Rev. Elec. Commun. Lab.*, vol. 16, 1968, 825-873.

[25] M. Hata, "Empirical Formulae for Propagation Loss in Land Mobile Radio Services," *IEEE Trans. Veh. Technol.*, vol. VT-29, 1980, 317-325.

[26] COST 231, "Urban Transmission Loss Models for Mobile Radio in the 900 MHz and 1800 MHz Bands (rev. 2)," COST 231 TD(90), 119 Rev. 2, Den Haag, 1991.

[27] R. B. Ash, C. A. Doléans-Dade, *Probability & Measure Theory, Second Edition*, Academic Press, San Diego, 2000.

[28] M. Pätzold, *Mobile Fading Channels*, John Wiley & Sons, Ltd., Chichester, 2002.

[29] M. R. Spiegel, *Mathematical handbook of formulas and tables*, McGraw-Hill, Inc., New York, 1994.

[30] T. J. Wang, J. G. Proakis, E. Masry, J. R. Zeidler, "Performance Degradation of OFDM Systems Due to Doppler Spreading," *IEEE Trans. Wireless Comm.*, vol 5, June 2006, 1422-1432.

[31] IST-2003-507581 WINNER, D5.4 v 1.4, "Final Report on Link Level and System Level Channel Model".

[32] IEEE, "Air Interface for Fixed and Mobile Broadband Wireless Access Systems, IEEE Standard, P802.16e/D12, February, 2005.

[33] Rec. ITU-R M. 1225, "Guideline for evaluation of radio transmission technologies for IMT-2000," 1997.

[34] COST 207, "Digital land mobile radio communications," Office Official Publ. Eur. Communities, Final Rep., Luxemburg, 1989.

[35] N. Czink, E. Bonek, L. Hentil, J.-P. Nuutinen, J. Ylitalo, "Cluster-based MIMO channel model parameters extracted from indoor time-variant measurements," *Proc. IEEE GlobeCom 2006*, San Francisco, November 2006.

[36] F. Babich, G. Lombardi, "A Markov Model for the Mobile Propagation Channel," *IEEE Trans. Veh. Technol.*, vol. 49, January 2000, 63-73.

[37] T. Koski, *Hidden Markov Models for Bioinformatics*, Kluwer Academic Publishers, Dordrecht, 2001.

[38] S. M. Ross, *Introduction to Probability Models, 8th edition*, Academic Press, San Diego, 2003.

[39] Y. Ephraim, N. Merhav, "Hidden Markov Processes", *IEEE trans. Inform. Theory*, vol. 48, June 2002, 1518-1569.

[40] W. Turin, "Throughput Analysis of the Go-Back-N Protocol in Fading Radio Channels", *IEEE Journal on Sel. Areas in Comm.*, vol. 17, May 1999, 881-887.

[41] H. S. Wang, N. Moayeri, "Finite-State Markov Channel – A Useful Model for Radio Communication Channels," *IEEE Trans. Veh. Technol.*, vol. 44, February 1995, 163-171.

[42] R. Carruthers, N. C. Beaulieu, "On an Improved Markov Chain Model of the Rayleigh Fading Channel," *Proc. IEEE Globecom 2007*, 2007, 1529-1534.

[43] C. C. Tan, N. C. Beaulieu, "On First-Order Markov Modeling for the Rayleigh Fading Channel," *IEEE Trans. Comm.*, vol. 48, December 2000, 2032-2040.

[44] J. Aráuz, P. Krishnamurthy, M. Labrador, "Discrete Rayleigh fading channel modeling," *Wirel. Commun. Mob. Comput.*, vol. 4, 2004, 413-425.

[45] A. J. Viterbi, "Error bounds for convolutional codes and an asymptotically optimal decoding algorithm," *IEEE Trans. Inform. Theory*, vol. IT-13, April 1967, 260-269.

[46] G. D. Forney, "The Viterbi algorithm," *Proc. IEEE*, vol. 61, March 1973, 268-278.

[47] H. S. Wang, "On Verifying the First-order Markovian Assumption for a Rayleigh Fading Channel Model," *IEEE Trans. Veh. Technol.*, vol. 45, May 1996, 353-357.

[48] W. Turin, R. van Nobelen, "Hidden Markov Modeling of Flat Fading Channels," *IEEE Journal on Sel. Areas in Comm.*, vol. 16, December 1998, 1809-1817.

[49] P. Bergamo, D. Maniezzo, A. Giovanardi, G. Mazzini, M. Zorzi, "An Improved Markov Chain Description for Fading Processes," *Electron. Lett.*, vol. 38, May 2002, 477-478.

[50] L. R. Wilhelmsson, "Evaluating the Performance of Raptor Codes for DVB-H by using the Gilbert-Elliott Channel," *Proc. IEEE VTC Fall*, 2007, 1932-1936.

[51] M. Zorzi, R. R. Rao, L. B. Milstein, "ARQ Error Control on Fading Mobile Radio Channels," *IEEE Trans. Veh. Technol.*, vol. 46, May 1997, 445-455.

[52] V. Tralli, M. Zorzi, "Markov Models for the Physical Layer Block Error Process in a WCDMA Cellular System," *IEEE Trans. Veh. Technol.*, vol. 54, November 2005, 2102-2113.

[53] L. F. Chang, "Throughput estimation of ARQ protocols for a Rayleigh fading channel using fade- and interfade-duration statistics," *IEEE Trans. Veh. Technol.*, vol. 40, February 1991, 223-229.

[54] M. Zorzi, R. R. Rao, L. B. Milstein, "Error Statistics in Data Transmission over Fading Channels," *IEEE Trans. Comm.*, vol. 46, November 1998, 1468-1477.

[55] M. R. Hueda, "On the Equivalence of Channel-State and Block-Error Markov Models for the Analysis of Transmission over Slow Fading Channels," *Proc. IEEE VTC Fall*, vol. 2, 2001, 1043-1047.

[56] M. R. Hueda, C. E. Rodríguez, "A New Information Theoretic Test of the Markov Property of Block Errors in Fading Channels," *IEEE Trans. Veh. Technol.*, vol. 54, March 2005, 425-434.

[57] O. Cappé, E. Moulines, T. Rydén, *Inference in Hidden Markov Models*, Springer Science+Business Media, New York, 2005.

[58] L. R. Rabiner, "A Tutorial on Hidden Markov Models and Selected Applications in Speech Recognition," *Proc. IEEE*, vol. 77, February 1989, 257-285.

[59] R. W. Chang, J. C. Hancock, "On receiver structures for channels having memory," *IEEE Trans. Inform. Theory*, vol. IT-12, October 1966, 463-468.

[60] S. Sivaprakasam, K. S. Shanmugan, "An Equivalent Markov Model for Burst Errors in Digital Channels," *IEEE Trans. Comm.*, vol. 43, Feb./Mar./Apr. 1995, 1347-1355.

[61] W. Turin, M. M. Sondhi, "Modeling Error Sources in Digital Channels," *IEEE Journal on Sel. Areas in Comm.*, vol. 11, April 1993, 340-347.

[62] E. N. Gilbert, "Capacity of a Burst-noise Channel," *Bell Systems Tech. Journal*, vol. 39, September 1960, 1253-1266.

[63] E. O. Elliott, "Estimates of Error Rates for Codes on Burst-error Channels," *Bell Systems Tech. Journal*, vol. 42, September 1963, 1977-1997.

[64] M. Mushkin, I. Bar-David, "Capacity and Coding for the Gilbert-Elliott Channels," *IEEE Trans. Inform. Theory*, vol. 35, November 1981, 1277-1290.

[65] J.-Y. Chouinard, M. Lecours, G. Y. Delisle, "Estimation of Gilbert's and Fritchman's Models Parameters Using the Gradient Method for Digital Mobile Radio Channels," *IEEE Trans. Veh. Technol.*, vol. 37, August 1988, 158-166.

[66] G. Sharma, A. A. Hassan, "Performance Evaluation of Burst-Error-Correcting Codes on a Gilbert-Elliott Channel," *IEEE Trans. Comm.*, vol. 46, July 1998, 846-849.

[67] C. Pimentel, I. F. Blake, "Modeling Burst Channels Using Partitioned Fritchman's Markov Models," *IEEE Trans. Veh. Technol.*, vol. 47, August 1998, 885-899.

[68] L. Wilhelmsson, L. B. Milstein, "On the Effect of Imperfect Interleaving for the Gilbert-Elliott Channel," *IEEE Trans. Comm.*, vol. 47, May 1999, 681-688.

[69] K. Sakakibara, "Performance Analysis of the Error-Forecasting Decoding for Interleaved Block Codes on Gilbert-Elliott Channels," *IEEE Trans. Comm.*, vol. 48, March 2000, 386-395.

[70] J. Garcia-Frias, J. D. Villasenor, "Turbo Decoding of Gilbert-Elliot Channels," *IEEE Trans. Comm.*, vol. 50, March 2002, 357-363.

[71] A. W. Eckford, F. R. Kschischang, S. Pasupathy, "Analysis of Low-Density Parity-Check Codes for the Gilbert-Elliott Channel," *IEEE Trans. Inform. Theory*, vol. 51, November 2005, 3872-3889.

[72] Y. Zhang, B.-H. Soong, "Performance of Mobile Networks with Wireless Channel Unreliability and Resource Insufficiency," *IEEE Trans. Wireless Comm.*, vol. 5, May 2006, 990-995.

[73] L. Zhong, F. Alajaji, G. Takahara, "A Binary Communication Channel With Memory Based on a Finite Queue," *IEEE Trans. Inform. Theory*, vol. 53, August 2007, 2815-2840.

[74] B. D. Fritchman, "A binary channel characterization using partitioned Markov chains," *IEEE trans. Inform. Theory*, vol. IT-13, April 1967, 221-227.

[75] F. Swarts, H. C. Ferreira, D. R. Oosthuizen, "Renewal Channel Models for PSK on Slowly Fading Rayleigh Channel," *IEEE Electronics Letters*, vol. 25, October 1989, 1514-1515.

[76] A. Semmar, M. Lecours, J.-Y. Chouinard, J. Ahern, "Characterization of Error Sequences in UHF Digital Mobile Radio Channels," *IEEE Trans. Veh. Technol.*, vol 40, November 1991, 769-776.

[77] W. Chang, T. Tan, D. Wang, "Robust Vector Quantization for Wireless Channels," *IEEE Journal on Sel. Areas in Comm.*, vol. 19, July 2001, 1365-1373.

[78] F. Downton, "Bruce's Spider and Renewal Theory," Operations Research, vol. 16, July-August 1968, 875-879.

[79] L. N. Kanal, A. R. K. Sastry, "Models for Channels with Memory and Their Applications to Error Control," *Proc. IEEE*, vol. 66, July 1978, 724-744.

[80] J. G. Kemeny, "Slowly Spreading Chains of the First Kind," *J. Math Analysis and Applications*, vol. 15, August 1966, 295-310.

[81] A. Konrad, B. Y. Zhao, A. D. Joseph, R. Ludwig, "A Markov-based channel model algorithm for wireless networks," *Wireless Networks 9(3)*, Kluwer Academic, New York, 2003, 189-199.

[82] W. Zhu, J. Garcia-Frias, "Stochastic Context-Free Grammars and Hidden Markov Models for Modeling of Bursty Channels," *IEEE Trans. Veh. Technol.*, vol. 53, May 2004, 666-676.

[83] J. McDougall, J. Joseph, Y. Yi, S. Miller, "An Improved Channel Model for Mobile and Ad Hoc Network Simulations," *Proc. CIIT '04*, St. Thomas, US Virgin Islands, 2004.

[84] W. Karner, M. Rupp, "Measurement based Analysis and Modelling of UMTS DCH Error Characteristics for Static Scenarios," *Proc. DSPCS2005*, Sunshine Coast, Australia, 2005.

[85] K. Levenberg, "A Method for the Solution of Certain Problems in Least-Squares," *Quarterly Applied Mathematics 2*, 164-168, 1944.

[86] D. Marquardt, "An Algorithm for Least-squares Estimation of Nonlinear Parameters," *SIAM Journal Applied Mathematics*, Vol. 11, 431-441, 1963.

[87] ISO/IEC 13818-1, "Information Technology - Generic Coding of Moving Pictures and Associated Audio Information. Part 1: Systems," Second Edition, 2000-12-01.

[88] 3GPP Technical Specification, "Digital cellular telecommunications system (Phase 2+); Radio transmission and reception," TS 05.05 v.8.20.0, November 2005.

[89] S. Ghahramani, *Fundamentals of Probability, with Stochastic Processes, 3rd edition*, Prentice Hall, New Jersey, 2004.

[90] G. Faria, J. A. Henriksson, E. Stare, P. Talmola, "DVB-H: Digital Broadcast Services to Handheld Devices," *Proc. IEEE*, vol. 94, January 2006, 194-209.

[91] T. Känkänen, "IP Packet Channel Modeling Applied in DVB-H Datacast System," *Master's thesis*, University of Turku, January 2007.

[92] ETSI, "Digital Video Broadcasting (DVB); DVB-H Implementation Guidelines," TR 102 377 v1.3.1, May 2007.

[93] ETSI, TS 102 472 v1.2.1, "IP Datacast over DVB-H: Content Delivery Protocols," Dec. 2006.

[94] M. Luby, *et al.*, "Raptor Codes for Reliable Download Delivery in Wireless Broadcast Systems," *Proc. IEEE CCNC*, Las Vegas, USA, 2006.

[95] P. I. Bratanov and E. Bonek, "Mobility Model of Vehicle-Borne Terminals in Urban Cellular Systems," *IEEE Trans. Veh. Technol.*, vol. 52, no 4, pp. 947-952, July 2003.

[96] D. Milanesio *et al.*, "Wing TV Network Issues," Celtic Wing TV project report, May 2006. Available online: http://projects.celtic-initiative.org/WING-TV/

[97] L. Litwin, M. Pugel, "The principles of OFDM," *RF Design*, No. 1, January 2001, 30-48.

[98] R. van Nee, R. Prasad, *OFDM for Wireless Multimedia Communications*, Artech House Publishers, Boston/London, 2000.

[99] L. Hanzo, M. Münster, B. J. Choi, T. Keller, *OFDM and MC-CDMA for Broadband Multi-User Communications, WLANs and Broadcasting*, John Wiley and Sons, Ltd., West Sussex, 2003.

[100] M. J. F.-G. Garcia, S. Zazo, J. M. Paez-Borrallo, "Pilot Patterns for Channel Estimation in OFDM," *IEEE Electronics Letters*, vol. 36, June 2000, 1049-1050.

[101] Y. Li, "Pilot-Symbol-Aided Channel Estimation for OFDM in Wireless Systems," *IEEE Trans. Veh. Technol.*, vol. 49, July 2000, 1207-1215.

[102] M. Speth, S. A. Fechtel, G. Fock, H. Meyr, "Optimum Receiver Design for Wireless Broad-Band Systems Using OFDM-part I," *IEEE Trans. Comm.*, vol. 47, November 1999.

[103] ETSI, "Digital Video Broadcasting (DVB); Transmission System for Handheld Terminals (DVB-H)," European Telecommunication Standard, EN 302 304 (v. 1.1.1), November 2004.

[104] ETSI, "Digital Video Broadcasting (DVB); DVB Specification for Data Broadcasting," European Telecommunication Standard, EN 301 192 (v. 1.4.1), November 2004.

[105] ETSI, "IP Datacast over DVB-H: Program Specific Information (PSI)/Service Information (SI)," Technical Specification, TS 102 470 (V1.1.1), April 2006.

[106] ETSI, "Digital Video Broadcasting (DVB); Framing Structure, channel coding, and modulation for digital terrestrial television," European Telecommunication Standard, EN 300-744, January 2004.

Appendix A

Orthogonal Frequency Division Multiplexing

A.1 Basic Principle of OFDM

Orthogonal frequency division multiplexing is a data transmission method, where N_{sc} data symbols are transmitted simultaneously using a set of orthogonal signals modulated by N_{sc} equidistant carrier frequencies. These orthogonal signals are typically called subcarriers. In OFDM systems, orthogonal subcarriers are mainly realized using rectangular time-domain pulses. The frequency spectrum of a rectangular signal pulse with duration T_s is described by a cardinal sine (or *sinc*) function, that is:

$$\Pi\left(\frac{t}{T_s}\right) \overset{F}{\leftrightarrow} T_s \frac{\sin(\pi f T_s)}{\pi f T_s},$$

where $\Pi(t/T_s)$ is a rectangular pulse with time duration T_s, and $\overset{F}{\leftrightarrow}$ denotes a Fourier transform relationship.

The zero-points of a sinc-function are found at frequencies $f = f_i \pm k/T_s$ Hz, $(k = 1, 2, ...)$, where f_i is the center (carrier) frequency of the i:th subcarrier. To achieve orthogonality between subcarriers, their carrier frequencies should be selected so that the center points of the individual subcarrier spectra match the zero-points of all other subbands. This leads to theoretically perfect orthogonality of the subcarriers in these points of the spectrum. That is, if the signal spectrum is sampled at these frequency points, every sample is completely determined by the peak value of the corresponding subcarrier. This principle is illustrated in Figure A.1.

In OFDM, the aforementioned is typically utilized by mapping the symbols to be transmitted into frequency-domain samples using a suitable complex signal constellation. Then an inverse fast Fourier transform (IFFT) is performed on the samples, producing a time-domain representation of the

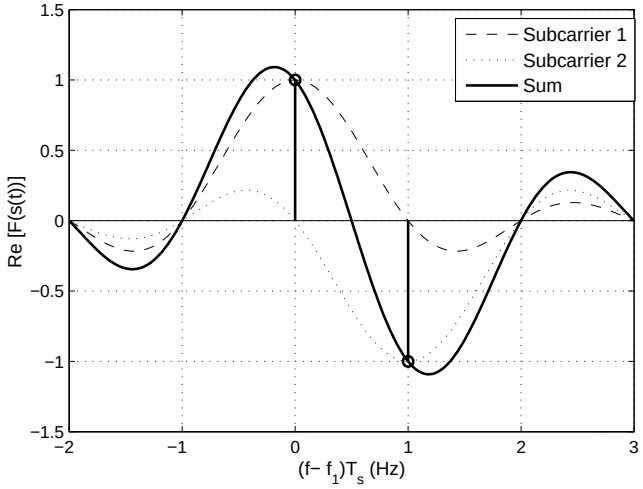

Figure A.1: A simple OFDM symbol in the frequency domain with two subcarriers modulated using binary phase shift keying with a symbol set $\{1, -1\}$. Shown are the individual subcarrier signals, and the OFDM signal corresponding to the sum of the subcarrier signals; the correct sampling of the OFDM signal is also demonstrated.

discrete signal. When this data is passed trough a digital-to-analog converter assuming an appropriate sampling frequency, a signal containing the orthogonal subcarriers previously defined is obtained for transmission. For a more in-depth overview of OFDM, references [97–99] are suggested. In the following, properties of OFDM systems most relevant to this Thesis are considered.

A.2 OFDM Symbols in the Time Domain

In the time domain the sum of the rectangular pulses with different carrier frequencies is called an OFDM symbol. The length T_s of the OFDM symbol determines the bandwidth of all the subcarriers in the signal spectrum. It is notable that since the (zero-to-zero) bandwidth $2/T_s$ of an individual subcarrier is typically only a fraction of the total bandwidth used by an OFDM symbol, the time duration of the symbol is correspondingly longer than the duration of a single-carrier signal pulse with the same total bandwidth. One effect of this is that OFDM has better tolerance of impulse noise than corresponding single-carrier modulation.

To reduce the effect of intersymbol interference (ISI) on an OFDM symbol, a *guard interval* can be inserted between successive symbols in the time domain. If the length of this guard interval is selected to be sufficiently

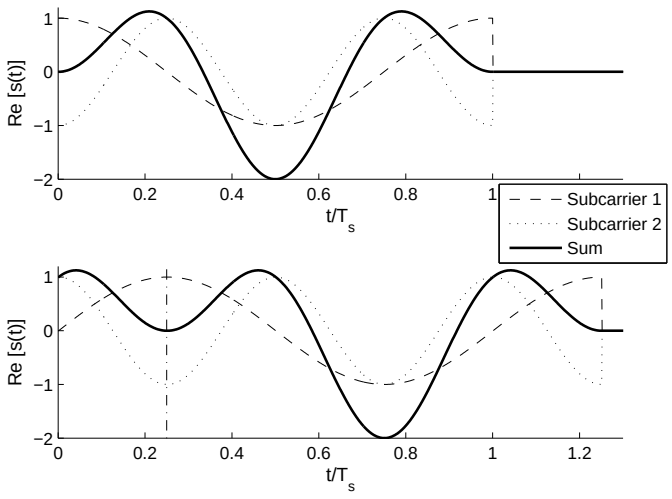

Figure A.2: A Simple OFDM symbol in the time domain with two subcarriers modulated using binary phase shift keying with a symbol set $\{1, -1\}$. Shown are the individual subcarrier signals, and the OFDM signal corresponding to the sum of the subcarrier signals. The upper subplot shows only the useful OFDM symbol with duration T_s, while in the lower subplot a cyclic prefix of length $l_{cp} = 1/4$ is also included.

larger than the delay spread of the channel, the effect of intersymbol interference will be mitigated by removing the guard interval at the receiver. A simple zero padded guard interval removes ISI, but leaves the signal vulnerable to frequency-selective fading caused by the communication channel. This problem, also called intrasymbol interference, is in practice solved by using a *cyclic prefix* instead of zero padding between successive symbols. Figure A.2 illustrates an OFDM symbol in the time domain without and with a cyclic prefix.

The cyclic prefix is obtained by copying a number of samples from the end of the OFDM symbol and concatenating these samples as a prefix before the useful signal. Thus the total length of the OFDM symbol becomes $(1+l_{cp})T_s$, where l_{cp} is the length of the prefix, relative to the useful symbol duration T_s. As stated before, the length of the prefix should be greater than the delay spread of the channel in use. If this condition is fulfilled, the signal will appear periodic in regard to convolution with the channel impulse response. As explained in reference [2], if at least one signal in a discrete convolution is periodic over the range of the convolution, the convolution in time is equivalent to multiplication in the frequency domain. This property makes equalization of OFDM symbols in the receiver significantly more efficient than traditional convolutional equalization.

A.3 Reception of an OFDM Signal

In reception, operations inverse to transmission are applied. The received signal is sampled with optimally the same sampling frequency and timing as in transmission. After sampling, a discrete Fourier transform is performed on the signal and the data symbols mapped onto the subcarriers can be estimated.

The effect of a frequency-selective transfer channel on the individual OFDM subcarriers is that they are multiplied by complex factors corresponding to the frequency response of the channel at the coincident frequency. Here the multiplicative property of the OFDM symbol gained by the use of a cyclic prefix can be utilized. If each sampled subcarrier is multiplied by the complex inverse of the channel frequency response at the frequency under inspection, the result will be the transmitted complex value of the subcarrier plus additive noise, which is also affected by the equalization. Thus if the channel frequency response at a given frequency is very close to zero, the subcarrier value obtained by such equalization is rather unreliable due to magnification of additive noise at that frequency.

To enable the equalization presented above, some method of estimating the channel frequency response is required. This is commonly achieved by mapping known values, or *pilot symbols*, into selected subcarriers. Compar-

ing the received values of these pilots to the known transmitted ones the receiver gains samples of the transfer channel at the pilot positions. Choosing the number of pilots used and the positions that they are inserted into is not a trivial task, however. On one hand, using more pilots gives more information about the channel. On the other hand, the pilots reserve subcarriers that could be used to carry information, thus reducing the effective data rate.

More detailed information on pilot symbol placement and subsequent channel estimation is found in literature for example in references [98–100]. The basic principle is that the pilot placement or channel sampling interval should fulfill the Nyquist sampling theorem [2] in order to enable accurate estimation of the channel frequency response. Note that in time-varying channels the Nyquist sampling theorem should be met both in the time domain and in the frequency domain. In practice this means roughly that the channel sampling interval in the time domain - corresponding to the time between subsequent OFDM symbols containing pilots - should be smaller than the coherence time T_C. Also, the sampling interval in the frequency domain - corresponding to the pilot carrier spacing within an OFDM symbol - should be shorter than the coherence bandwidth B_C (T_C and B_C are defined in Chapter 2).

The channel estimation principle outlined above, which uses scattered pilots in the time and frequency domain, is suitable for rapidly varying channels such as those utilized in DVB-H and Digital Audio Broadcasting (DAB). In many packet transmission systems such as wireless local area networks (WLAN), the channel impulse response can be considered constant within several OFDM symbol periods. In such cases a more suitable method of including whole symbols dedicated to estimating the channel parameters can be utilized. More information on this channel estimation method is given in reference [101]. It is notable that one of the main advantages of OFDM is that it allows transmission over highly frequency-selective channels at a low receiver implementation cost. In particular, costly equalizers needed in single-carrier systems are dramatically simplified [102]. This, along with the relatively long time duration of OFDM symbols, which enables operation over channels with large delay spreads, makes OFDM a suitable transmission method for *single-frequency networks* (SFN). An SFN differs from a cellular network in that all transmitters operate at the same carrier frequency. At the network level this requires careful synchronization of the transmitters. However, regardless of the synchronization accuracy, increased delay spreads are a typical characteristic for single-frequency networks, which must be taken into account when selecting the cyclic prefix length and pilot symbol configuration for an OFDM system.

Finally, it should be noted that when the maximum Doppler frequency of the communication channel is significant compared to the bandwidth of

Table A.1: Effects of wireless channel characteristics on OFDM signals, and counteractions available by adjusting the basic OFDM system parameters. **To mitigate the effects of intercarrier interference and impulse noise, additional noise canceling algorithms and forward error correction/interleaving schemes may be used.*

Channel property	Effect on OFDM signal	Counteraction
$S_D/T_s > 0$	(i) Intersymbol interference	(i) Guard interval
	(ii) Frequency-selective fading	(ii) Prefix & pilots
		(i),(ii) Incr. T_s, l_{cp}
$f_D T_s > 0$	Intercarrier interference	Decrease T_s *
Impulse noise	Low SNR	Increase T_s *

the OFDM subcarriers - described by the *normalized Doppler bandwidth* $f_D T_s$, which will in this case be larger than zero - the received signal will be distorted by intercarrier interference (ICI). As described in reference [30], the ICI is effectively additive noise that can no longer be corrected using equalization as described in the previous Section, and requires the use of specific ICI cancelation algorithms. Since OFDM symbols are by nature often lengthy in the time domain, corresponding to relatively small subcarrier bandwidths, intercarrier interference is a considerable limitation on the use of OFDM. In fact, the poor performance of OFDM in rapidly time-varying channels is one of the main arguments against applying OFDM [99]. Table A.1 summarizes the most crucial properties of mobile wireless channels related to the performance of OFDM systems, and possible methods to reduce the distortion caused by the communication channel by adjusting the basic OFDM system parameters.

Appendix B

DVB-H

Digital video broadcasting for handheld terminals (DVB-H), as specified in references [90, 92, 103], is an expansion of the terrestrial digital video broadcasting standard (DVB-T) [92]. In the following, a brief summary of the DVB-H system and its features is given, along with brief descriptions of the intended benefits of the modifications to the DVB-T standard, which is designed primarily for static rooftop reception.

B.1 System Features

DVB-H is built on the terrestrial broadcasting standard DVB-T. This offers the possibility of implementing DVB-H in existing DVB-T networks with some modifications. According to the DVB-H implementation guidelines [92], it should be possible to transmit a DVB-H stream simultaneously with a DVB-T stream in a network without significant disturbance or requirement for modification in existing DVB-T receivers. Moreover, traditional DVB-T integrated receiver-decoder chip designs can be modified to enable reception of the DVB-H stream by relatively simple changes to the hardware and system software.

A DVB-H transmitter consists of an IP (internet protocol) encapsulator, a multiplexer that constructs transport stream (TS) packets from DVB-H IP streams and possible DVB-T MPEG2 streams [87], and a modified DVB-T modulator. The modifications and additions to the existing DVB-T standard are due to specific requirements set by handheld terminals (light-weight, battery-powered apparatus) on the transmission system. These requirements, as described in [92], include reducing the average power consumption in the receiver by *time slicing*, seamless handovers between transmission cells, and low-noise signal reception in a wide range of reception scenarios, noise environments and transmission networks.

Mandatory additional features in the DVB-H system as compared to

DVB-T are link layer time-slicing of the transmitted IP-stream, and physical layer DVB-H parameter signaling in previously unused DVB-T transmission parameter signaling (TPS) bits. Optional features include forward error correction for multiprotocol encapsulated data (MPE-FEC), an additional 4K OFDM modulation mode (shorthand notation for the total number of subcarriers used in the system which for 4K is $2^{12} = 4096$), and in-depth symbol interleaving for the 2K and 4K modulation modes. It should also be noted that the payload of DVB-H is IP-datagrams or other network layer datagrams encapsulated into MPE-sections, as opposed to the MPEG-2 stream transmitted by a DVB-T system.

Time-slicing means sending data in short bursts using a significantly higher instantaneous bit rate compared to the average bit rate of the transmitted service. The main advantages of time-slicing are reduced power consumption and the possibility to accomplish seamless handovers between transmission cells. The reduction in power consumption is due to the relatively small duty cycles used in time-slicing; for example, a 10 % data transmission duty cycle implies a 90 % reduction in the power consumption of the receiver radio hardware. Also, time-slicing enables the receiver to monitor neighboring cells during reception off-times. If a handover is accomplished during an off period, the reception of a service is seemingly uninterrupted, provided that the service content is synchronized between neighboring cells.

Link layer forward error correction is an optional feature intended to improve carrier-to-noise ratio performance and Doppler performance in mobile channels. Forward error correction should also improve tolerance to impulse interference. As defined in [104], MPE-FEC coding utilizes a combination of Reed-Solomon and 32-byte cyclic redundancy check codes. For a detailed description and analysis of the MPE-FEC coding in DVB-H, see reference [17].

Program specific information/service information (PSI/SI [105]) are essential data for service discovery in DVB-H systems. The PSI enables a decoder to demultiplex DVB-H services. The SI contains data on DVB-H services carried by different multiplexes. It should be noted that MPE-FEC coding is not applied for PSI/SI, which are transmitted with only cyclic redundancy check information to verify their correctness.

An optional addition to the DVB-T modulator is the 4K OFDM mode. The DVB-T standard [106] originally defines two modes of operation: 2K and 8K. The operation mode determines the number of subcarriers used in OFDM, thus affecting the optimal network configuration for the system. Because the bandwidth occupied by the system is fixed for a given network, changing the number of subcarriers directly affects the OFDM symbol duration. Increasing the number of subcarriers increases the symbol duration, which means that the system has better tolerance for large delay spreads.

This is beneficial in large single-frequency networks, but also leads to worse performance in high-speed reception. The objective of the added 4K OFDM mode is to improve the network planning flexibility by allowing a tradeoff between mobility and single frequency network size.

In-depth symbol interleaving is another optional modification to the DVB-T modulator. In-depth interleaving is specified in [106] for the 2K and 4K modulation modes. It is designed to improve reception in fading channels, and to provide an extra level of protection against short noise impulses by increasing the symbol interleaver depth. This is achieved by utilizing the memory capacity of the 8K symbol interleaver in interleaving 2K and 4K symbols; this effectively quadruples (for 2K) or doubles (for 4K) the symbol interleaver depth.

B.2 Data Flow in DVB-H Transmission

The DVB-H IP-encapsulator arranges incoming IP datagrams into MPE sections, optionally performing FEC coding and time slicing. If time-slicing is used, additional delay information (or delta-t information) is added to the MPE and MPE-FEC section headers. This information is used to signal the time from the start of the MPE (or MPE-FEC) section currently being received to the start of the next time-sliced data burst. MPE (or MPE-FEC) sections are encapsulated into TS packets and then multiplexed along with other possible data streams into a DVB-T/H modulator. In DVB-H, PSI/SI information is carried in MPEG-2 private table structures, which are segmented into sections, inserted into transport stream packets, and multiplexed into the modulator [105].

Figure B.1 shows the link layer IP encapsulation in DVB-H. Network layer IP datagrams are first written column-wise into the application data table part of an MPE-FEC frame, which consists of a total of 191 columns. The application data table is encoded row-wise using a systematic Reed-Solomon code; the resulting 64 correction bytes per row are then added to the RS data table part of the MPE-FEC frame. The row-wise encoding of the application data arranged into columns results in a virtual interleaving effect that is useful in difficult fading scenarios, as only weak time interleaving is available in DVB-H, and only with in-depth interleaving.

The MPE-FEC code rate can be adjusted by zero-padding either the application data table, or the RS data table. The added zeros are not transmitted; the MPE and MPE-FEC section headers shown in Figure B.1 contain information for reconstructing the MPE-FEC frame in the receiver. If forward error correction is not used, the whole MPE-FEC frame is filled with IP data. This also removes the virtual interleaving mentioned above.

After the MPE-FEC frame is constructed, the application data table IP

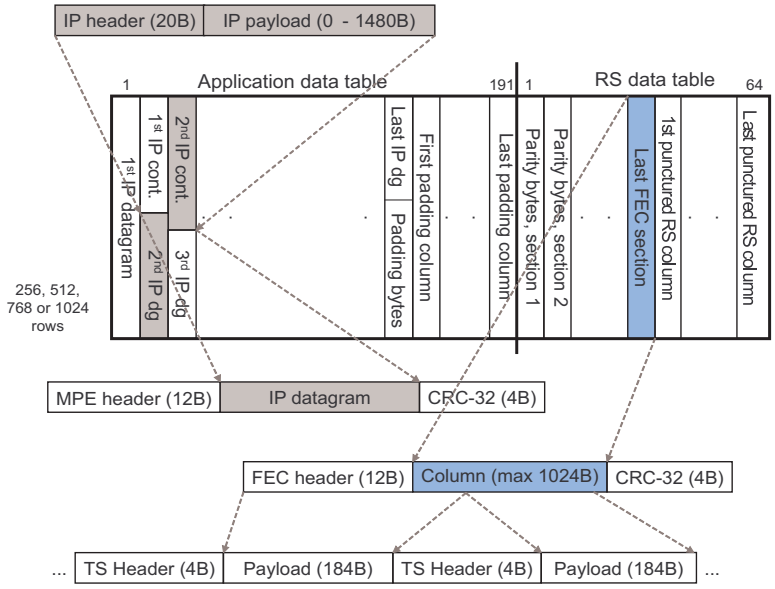

Figure B.1: DVB-H link layer operations [17].

datagrams are encapsulated into MPE sections, which include 12-byte MPE headers and four CRC-32 error detection bytes. In a similar fashion, the RS data table columns are encapsulated into MPE-FEC sections; the only difference between MPE and MPE-FEC sections is that the section header fields differ. The encapsulated MPE and MPE-FEC sections are partitioned into TS packets and transmitted through the modified DVB-T modulator in the physical layer.

A functional block diagram of a DVB-T/H modulator is shown in Figure B.2. Input to the DVB-H modulator is arranged into fixed-length transport stream packets; total length of one transport multiplex (MUX) packet is 188 bytes, following the MPEG-2 transport multiplex defined in reference [87]. Note that the block diagram of Figure B.2 contains two parallel processing paths up to the inner interleaver block. This is required when hierarchical modulation is used, that is, two data streams of different priorities are transmitted simultaneously. The "HP" and "LP" abbreviations in Figure B.2 refer to High Priority and Low Priority, respectively.

The first byte of each TS packet is always a synchronization byte, set in the MUX adaptation step. The other 187 bytes of a TS packet are randomized using a pseudo random binary sequence (PRBS) generator to ensure adequate binary transitions; this procedure is also referred to as energy dispersal.

After energy dispersal the TS packet is coded using a Reed-Solomon code, which enables correcting 8 erroneous bytes in each TS packet. The

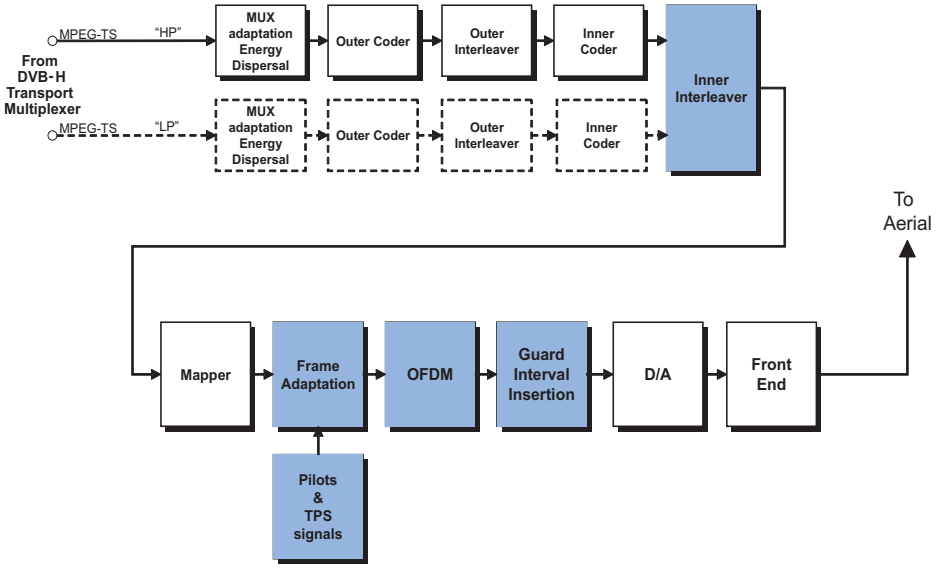

Figure B.2: Functional block diagram of a DVB-T/H modulator [106]. Blocks with DVB-H-specific modifications are shaded.

resulting error protected packets of length 204 bytes are then byte-wise interleaved in the outer interleaver. The interleaved bit stream is convolutionally coded in the inner coder, which uses a mother code of rate 1/2, and allows punctured rates of 2/3, 3/4, 5/6 and 7/8. Note that information on the code rate used is transmitted in the transmission parameter signalling bits that are added to the transmitted OFDM symbol before modulation.

The convolutionally coded data is passed to an inner interleaver and mapper, which assign input bits onto output modulation symbols according to the signal constellation used. In the inner interleaver the input bit stream - or two streams in the hierarchical case - is demultiplexed into a total of v substreams, where $v = 2$ for QPSK, $v = 4$ for 16-QAM, and $v = 6$ for 64-QAM. After demultiplexing, or serial-to-parallel conversion, bit interleaving is performed using a block size of 126 bits per interleaver. That is, corresponding bits in 126 input vectors are shuffled using a different permutation function for each bit interleaver. This block interleaving process is repeated exactly twelve times per OFDM symbol of useful data in the 2K mode, twenty-four times in the 4K mode and forty-eight times per symbol in the 8K mode. Also, when in-depth interleaving is applied in the 2K or 4K modes, the block interleaving process must be repeated forty-eight times in order to supply the symbol interleaver with enough data to produce either four consecutive 2K OFDM symbols or two consecutive 4K OFDM symbols [106]. From the inner interleaver up to the transmitter front end the

system operates with modulation symbols, whose bit-length is determined by the signal constellation used.

The outputs of the v bit interleavers form the final bit vectors, or data symbols, to be mapped onto the OFDM subcarriers. The purpose of an additional symbol interleaver is to offer frequency diversity and to map the v-bit modulation symbols onto the 1512 (2K mode), 3024 (4K mode) or 6048 (8K mode) active carriers per ODFM symbol. The block size of the symbol interleaver in the native interleaving mode is thus same as the number of data carriers required per OFDM symbol. When the in-depth interleaver is selected, the symbol interleaver acts on blocks of 6048 data symbols in all modulation modes. The main idea of in-depth symbol interleaving is to utilize the full memory capacity present in both the transmitter and the receiver.

After the symbol interleaver, Gray coding is applied to map the groups of input bits to modulation symbols. The DVB-T-system allows different levels of QAM modulation, namely QPSK, 16-QAM and 64-QAM, to be used to trade bit rate versus ruggedness. The system also allows two-level hierarchical channel coding and modulation. In hierarchical modulation several bit streams of different priorities are mapped to the same signal constellation. In this case the most significant bits of each QAM symbol contain a high-priority bit stream that is decoded as if the constellation were QPSK. To decode the low-priority bits the full constellation is examined.

OFDM subcarriers not used for data or TPS signaling are modulated with reference information whose transmitted value is known to the receiver. This enables channel estimation and frequency-domain equalization in the receiver as described in Appendix A. The OFDM symbols in DVB-H contain both scattered and continual pilot cells, whose values are determined by a pseudo-random binary sequence. The continual pilots occupy the same carriers in all OFDM symbols, while the scattered cells are shifted cyclically between OFDM symbols. Reference pilot cells are BPSK modulated, and transmitted with a power level 4/3 times the average power of the data subcarriers. After the addition of TPS and pilot cells, the total number of carriers in an OFDM symbol is 1705 (in 2K mode), 3409 (4K mode) or 6817 (8K mode). Of the added reference pilot cells, 45 (2K), 89 (4K) or 177 (8K) are continual pilots [106]. After the data symbols and pilot cells are mapped to the carriers, a time-domain OFDM symbol is constructed and a cyclic prefix is added to the useful part of the OFDM symbol. One of four cyclic prefix lengths may be used: 1/4, 1/8, 1/16 or 1/32 of the duration of the useful part.